

Investigation of Capillary Suspension Drying Behavior with Simultaneous Stress and Weight Measurements

Zur Erlangung des akademischen Grades eines

DOKTORS DER INGENIEURWISSENSCHAFTEN (Dr.-Ing.)

von der KIT-Fakultät für Chemieingenieurwesen und Verfahrenstechnik
des Karlsruher Instituts für Technologie (KIT)

genehmigte

DISSERTATION

von

Dipl.-Ing. Steffen Benno Fischer
aus Böhmenkirch

Hauptreferent:

Prof. Dr. Erin Koos

Korreferent:

Prof. Dr.-Ing. Wilhelm Schabel

Tag der mündlichen Prüfung:

29. Juni 2021

Preface

The presented research in this dissertation is based on four peer-reviewed scientific journal articles of which three are published and one has been accepted. They contain the major results of my experimental work from October 2014 until July 2019 performed at the Institute of Mechanical Process Engineering and Mechanics in the Applied Mechanics group at the Karlsruhe Institute of Technology ([KIT](#)) in Germany, as well as research carried out in the Soft Matter, Rheology and Technology ([SMaRT](#)) group at the KU Leuven ([KUL](#)) in Belgium.

This manuscript comprises a brief introduction into the mechanism causing stress formation in coatings during drying, capillary suspensions, and how their rheological behavior can aid in crack prevention. This is followed by a description of my novel design for a film stress measurement apparatus as well as results obtained by employing it. Moreover, I present a new way and background of capillary suspension formulation and its implications on drying. The thesis consists of the following articles:

1. Apparatus for simultaneous stress and weight measurement [chapter 2](#),
2. Using an added liquid to suppress drying defects [chapter 3](#),
3. Influence of drying conditions on the stress and weight development of capillary suspensions [chapter 4](#), and
4. Capillary bridge formation at room temperature in binary liquids with small miscibility [chapter 5](#).

The dissertation concludes with a summary and outlook. The list of publications include my own journal articles and conference contributions, followed by the bibliography, which contains all references used in this dissertation. As a consequence, the reference numbers in the chapters are adapted from the original publication.

Acknowledgements

Finally, after several years of hard work, my dissertation is concluded and it is time to express my gratitude and extend a big thank you to everyone who contributed to this accomplishment in various ways.

First, I would like to thank my supervisor Prof. Dr. Erin Koos for offering me the possibility to pursue a PhD in your group. Thank you for your constant support, encouragement, and the scientific advice throughout the years. I highly appreciate your speed and willingness to look through manuscripts and presentations on weekends or late nights. I am very grateful for the opportunity to spend a three months research stay in Seoul, South Korea. Thank you for nudging me to embrace yet another adventure abroad. For your help and flexibility with the move to Leuven as well as your efforts to fulfill our wishes that arose and get the best out of the time in Belgium.

Prof. Dr.-Ing. Wilhelm Schabel, I very much appreciate you serving as the second reviewer; for giving me the opportunity to perform the shrinkage measurements in your lab; and for enlightening discussions at conferences and various points during the project.

I thank Prof. Dr. Norbert Willenbacher for the opportunity that you gave me to work in your group, especially for the support in supervising students, and the fruitful discussions in the group as well as introducing me to new research areas.

I would also like to thank Prof. Kyung H. Ahn from Seoul National University in South Korea, for the possibility to spend time in your lab. Dr. Sunhyung Kim is thanked for initiating my research stay in Korea as well as for discussions and the introduction to stress measurements. I am indebted to the entire microrheology group, especially Sanghyuk, Howon, Jieun, Jin Hwan, and Do Hoon, for making me feel extremely welcome; all the amazing food I had the pleasure to experience with you; the little trips around the city you had organized for me; and in general for helping me out whenever necessary. Thank you all for this unforgettable experience.

Thanks to my students: Janine Wittemann, Karoline Kozubski, Caroline Papenhagen and Grégoire Castel for your contribution and the cognition resulting from your work; the

design project groups I supervised for discussions and solutions for real industrial problems that were a welcome distraction from research drawbacks.

Many thanks to Karsten Sasso, Olaf Jörg and his team from the mechanical workshop at the Karlsruhe Institute of Technology ([KIT](#)) for your precise work and making things possible that were deemed extremely difficult to realize. Moreover, Herman Tollet from the CIT departmental workshop at KU Leuven, Belgium is thanked for his passion when further adjustments were necessary. Thank you Nico for helping to get my apparatus implemented in the lab infrastructure and your introduction to the equipment. To Anja, our lab mom, for always caring and making sure experiments go smoothly and keeping everything in order.

Thanks to my colleagues in Karlsruhe, and everyone at [SMaRT](#) in Leuven, for your warm welcome, discussions, help and social activities. Irene, Moritz and Frank for the mutual encouragement during the research and especially during the course of the move to Leuven. Thank you Sebastian for your delicious Lasagne and your help whenever needed during and after my time in Leuven. Irene, thank you for continuously checking in and your encouraging words as well as the tasty dinners. Thanks to the entire Leuven crew, from Professors to colleagues; gratitude to my dear office mates BramBerta for keeping in touch well beyond my time in Leuven. Thanks Roberta for keeping the office alive and happy. Bram for our legendary squash battle until failure and your continuous help and humor :). Your substitute Jens, the new youngster in the house. Thank you for helping me out with various things from confocal microscopy measurements to providing information after I had already left. Venkat, Yannick, Iurii, Kenneth and Lucas for making our office a truly international experience. Jasper, thank you for organizing all the social events that made me feel comfortable and welcome very quickly! Jan, for the scientific discussions, but even more the occasional wine and beer during late nights, movie sessions, BBQ and bar tours that kept me sane during all the work. Greet, thank you for always joining me for one more glass of water. Karel, thank you for all the stories and anecdotes, your help whenever needed and the lovely nights over dinner. Most of all, I would like to thank Susanna and Avanish. For the warm welcome, all the good company during all sorts of activities, all the comforting and supporting chats to get each other through difficult times. Thank you Ava for giving me the opportunity to be part of your amazing wedding and being my gym buddy, even if that meant for you to sacrifice sleep or writing another paper overnight. I hope we can all reactivate and maintain our friendship regardless of the distance.

A shout-out to my friends from the badminton group: Amaury, Kingshuk, Koen, Michiel, Ruben, Shin, Siddharta and Simon for a fun time on and off the court, and during recuperation at De Spuye.

Thank you, Manuel G. for checking in on me regularly and offering your help especially during the last year, for always providing me with essential nutrients and a bed when visiting Karlsruhe. Moreover, I am grateful for your and everyone else's step by step recipes and tips on administrative things that accompany a thesis.

Despite writing this dissertation during Corona times (not the beer) with not much else to do (except having a full time job), it didn't make it easier. Thanks to all my friends who cared and asked about my well being. Especially my close friends: Daniel, Hannes, Christoph and everyone else who was willing to listen to me when I needed to vent.

Finally, my deepest gratitude to my parents who supported me throughout my life. In particular during my studies and on my global adventures.

Frankfurt, December 2020

Steffen Benno Fischer

Abstract

Coatings and ceramic green bodies usually contain polymeric additives to prevent cracking caused by drying induced stresses, which requires subsequent removal steps. A new coating formulation using capillary suspensions was found to reduce cracking, while being absent of polymeric additives. This dissertation investigates the drying behavior of capillary suspensions. The cantilever deflection method, commonly used for investigation of drying stresses, is significantly improved. The simultaneous stress and weight measurement technique of the same coating in a temperature and humidity controlled chamber developed in this dissertation is unprecedented. Enhanced by visual observation and coating profiling, we propose liquid flow considerations to explain the observed prolonged constant drying period. Stress measurements performed at different drying conditions and suspension formulations show a decrease in peak stress by up to 40% for the capillary suspension over the regular suspension without polymeric additives. A complex interplay between yield stress, capillary suspension formulation, and humidity that is capable of reducing the peak stress of a regular suspension is revealed. The role of water, an integral part of most capillary suspensions, was further investigated. We find that capillary suspensions can be formed from partially miscible liquid-liquid systems at low added fluid concentrations ($\lesssim 4$ vol%), just outside the miscibility gap, by adding particles followed by mixing. Even when stored in humid conditions, capillary suspension formation is observed. These findings have an effect on undesired flocculation of formulations when stored in a humid environment, but also impact stress reduction during drying.

Zusammenfassung

Partikelbeschichtungen sind allgegenwärtig im täglichen Leben. Sie finden beispielsweise Anwendung in Holzfarben, wo die eingebetteten Partikel UV-Licht streuen und so eine Schädigung des Holzes vermeiden [1], oder in Beschichtungen als Korrosionsschutz auf hoher See [2]. Eine in letzter Zeit an Bedeutung gewinnende Anwendung sind gedruckte Leiterbahnen, Batterien oder Solarzellen [3–6]. Die hierfür treibende Kraft ist u.a. die günstige Produktion von radio frequency identification (RFID) Transpondern, die auf flexible Substrate gedruckt, vielfältige Einsatzmöglichkeiten für das Internet der Dinge (IoT) bieten [7]. Um ein betriebsfähiges Produkt zu erhalten, müssen die funktionalisierten Partikel zunächst in einer Trägerflüssigkeit dispergiert und durch rheologische Zusätze so angepasst werden, dass optimale Druckeigenschaften vorliegen. Anschließend muss die Trägerflüssigkeit durch Trocknung aus der Beschichtung entfernt werden. Während dieses Schrittes können jedoch Spannungen im Film auftreten, die zu Rissen und anderen Defekten führen. Um dies zu verhindern, werden polymerbasierte Binder und Tenside hinzugegeben, die aber nach dem Trockenschritt durch Anlassen ebenfalls wieder entfernt werden müssen. Während dieser Temperaturbehandlung kann es wiederum zu Rissen kommen. Des Weiteren werden hierbei oft Temperaturen benötigt, die über der Glasübergangstemperatur des polymerbasierten Substrats liegen und dieses dadurch schädigen. In einer vorangegangenen Arbeit wurde beobachtet, dass Kapillarsuspensionen zu einer verringerten Rissbildung neigen [8]. Diese neue Klasse von Suspensionen wurde von Koos und Willenbacher [9] entdeckt und charakterisiert. Kapillarsuspensionen besitzen Eigenschaften, die beim Druckvorgang benötigt werden und bestehen neben den Partikeln aus flüchtigen Komponenten, die nachfolgende Verarbeitungsschritte überflüssig machen [10, 11].

Die vorliegende Arbeit strebt die Verbesserung des Verständnisses für das Trocknungsverhalten von Kapillarsuspensionen und den zugrundeliegenden Mechanismen an. Um das Trocknungsverhalten von Filmen, sowie die dabei entstehenden Spannungen zu untersuchen, musste ein Messapparat konzipiert und aufgebaut werden. Dieser ist in Kapitel 2 beschrieben. Das verwendete Messprinzip basiert auf der Biegung einer einseitig eingespannten Blattfeder (Kragträger). Dies ist die vorwiegend verwendete Methode, um

Spannungen von Filmen während der Trocknung unter kontrollierten Bedingungen zu bestimmen. Neben den Spannungen ist die Geschwindigkeit der Trocknung von Interesse. Die Trocknungsrate erlaubt es, Rückschlüsse über morphologische Änderungen, wie beispielsweise den Rückzug des Trocknungsspiegels in den Film, zu ziehen. Dieser Rückzug resultiert in Stofftransportwiderständen, welche die Trocknung verlangsamen. Bis jetzt wurde diese Messgröße bestimmt, indem die Masseänderung eines zweiten beschichteten Trägers in der Kammer gemessen wurde. Die beiden Messungen von Spannung und Gewichtsverlust wurden behandelt, als stammten sie von einer Probe. Ein Problem das hierbei zu Tage tritt, sind Temperaturgradienten in der Kammer, die zu Verfälschungen der individuellen Messungen führen können. Zudem wird angenommen, dass das Profil der beiden Beschichtungen, dessen Dicke und das Trocknungsverhalten identisch seien. Diese Annahme mag beim Aufbringen von niederviskosen Materialien berechtigt sein. Bei viskosen oder gar elastischen Pasten (gelartig) hingegen, wie beispielsweise bei Kapillarsuspensionen, weisen die einzelnen Filme kleine Variationen in der Nassfilmdicke auf. Diese Unterschiede rühren von Kanteneffekten des Substrats. Aus diesem Grund wird ein Messprinzip, basierend auf der Balkenbiegung, entworfen, das in der Lage ist, gleichzeitig die Spannung sowie die Trocknungsrate von ein und derselben Beschichtung in einer Kammer, mit einstellbarer Temperatur und Luftfeuchtigkeit zu bestimmen. Der Andockmechanismus besteht aus einem Magneten, der ein Rotieren und Verschieben der Substrat-Aufhängung verhindert, um Wiederholbarkeit zu gewährleisten. Zudem ist eine Kamera zur visuellen Verfolgbarkeit der Trocknung installiert. Eine ausgeklügelte Hebevorrichtung ermöglicht das schnelle Einbringen des Beschichtungsträgers in die Kammer, sowie dessen Andocken an den Magneten mit korrekter Ausrichtung. Die Beschichtungsvorrichtung ist passgenau für den Filmträger gefertigt, wobei ein schwacher Magnet als Unterlage für das metallene Substrat dient und dieses in vertikaler Position hält. Eine höhenverstellbare Rakel wird anschließend mit variabler Geschwindigkeit über das Substrat geführt und hierdurch beschichtet. Alle benötigten Messgeräte, wie Schichtdickenmessgerät, Temperatur- und Feuchtigkeitssensoren, Kalibriereinheit, Waage und Laserpositions-Photodiode sind mit einem PC verbunden und werden mittels LabView aufgezeichnet, wie in Kapitel 2 beschrieben.

Der in dieser Arbeit weiterentwickelte Messaufbau ist der Grundstein für weitere Untersuchungen zur Trocknung von Kapillarsuspensionen. In Kapitel 3 wird die integrierbare Kamera eingesetzt, um visuelle Änderungen des Films mit den gemessenen Spannungen zu vergleichen. Die untersuchte Modell-Kapillarsuspension liegt im sogenannten "pendular state" vor, d.h. die Zweitflüssigkeit benetzt bevorzugt die Partikel. Die kontinuierliche Phase besteht aus 1-Heptanol mit suspendierten Al_2O_3 Partikeln mit einem

Durchmesser von $d_{50,3} = 0.5 \mu\text{m}$. Das Partikelnetzwerk bildet sich durch Zugabe von 2.5 vol % hochreinem Wasser und nachfolgender Durchmischung mit hoher Scherung. Dies führt zu einer Suspension mit einem Partikelvolumenanteil von $\phi_{\text{solid}} = \phi_{\text{Al}_2\text{O}_3} = 0.2$. Anschließend wird die Trocknung der Kapillarsuspension mit der Formulierung ohne Zugabe der netzwerkbildenden Zweitflüssigkeit (Nullsuspension) bei $40 \text{ }^\circ\text{C}$ verglichen. Wie bereits zuvor in anderen Untersuchungen beobachtet, neigt die Nullsuspension zu seitlicher Trocknung auf dem Kragträger. Dies bedeutet, dass der Film zuerst an den Kanten, aufgrund einer dort höheren lokalen Trocknungsrate, trocknet und schrumpft. Folglich führt dies zu einem Spannungsanstieg und Absinken der gesamten Trocknungsgeschwindigkeit. An den Kanten ist die Kontaktlinie der Trägerflüssigkeit jedoch angeheftet, was zu einem Flüssigkeitsstrom hin zu den Kanten führt. Suspendierte Partikel werden dadurch mitgetragen, analog zum "coffee-ring" Effekt. Die dortige Partikelanhäufung führt zu einer Verarmung an Feststoff in der Mitte der Beschichtung, was sich in der Bildung einer Furche oder Nadellöchern auswirkt. Diese Defekte sind unerwünscht und machen Beschichtungen unbrauchbar. Im Gegensatz dazu, wies die Kapillarsuspension diese Defekte nicht auf. Darüber hinaus zeigt die Bildauswertung eine scheinbar trockene Oberfläche, dessen Auftreten mit einem steilen Spannungsanstieg einhergeht. Interessanterweise bleibt die gesamt-Trocknungsrate konstant, sogar über den Punkt der quasi vollständig geschrumpften Beschichtung (Maximalspannung) hinaus. Um den Materialfluss der kontinuierlichen Phase (1-Heptanol) zu untersuchen, wird sie eingefärbt. Hierbei zeigt die Nullsuspension eine klare Aufkonzentration an den Rändern des Kragträgers, was den Lösemitteltransport an diese Stellen bestätigt. Die Kapillarsuspension zeigt im Gegensatz dazu einen minimalen Tracertransport. Deshalb kann ein starker Lösemitteltransport ausgeschlossen werden, nicht jedoch ein Verschieben der Kapillarbrücken mitsamt der Partikel. Das Einfärben der Zweitphase zeigt nach der Trocknung eine homogene Farbverteilung in der Beschichtung. Dies führt zu dem Schluss, dass weder Partikel noch Kapillarbrücken zu den Kanten transportiert werden.

Um das Schrumpfverhalten der beiden Suspensionen während der Trocknung näher zu untersuchen, wird das Filmprofil ex situ gemessen. Hierbei bestätigt sich, dass die Nullsuspension vorrangig an den Kanten schrumpft, während der Rest der Partikel in der Beschichtung noch suspendiert vorliegt. Die Kapillarsuspension dagegen schrumpft mit einem fundamental verschiedenen Mechanismus. Wie aus den Farboxperimenten zu erwarten war, verdichtet sich der Film an den Kanten zunächst nur minimal. Nach kurzer Zeit aber, stoppt der seitliche Schrumpf, während der Film in der Mitte des Kragträgers noch fast vollständig suspendiert vorliegt. Anschließend trocknet dieser Teil ohne weiter an den Kanten zu schrumpfen, bis das Oberflächenprofil fast identisch mit

dem des ursprünglichen Nassfilmprofils ist. Erst ab diesem Zeitpunkt schrumpft der Film im gesamten Querschnitt weiter und zwar vorrangig in der Höhe, während das Oberflächenprofil praktisch unverändert bleibt. Dieses Verhalten kann mit einem lokalen Anstieg der Fließgrenze an den Kanten (durch die anfängliche Verdichtung) erklärt werden, welche den dort auftretenden Druckkräften entgegenwirkt. Sobald die noch suspendierten Partikel auf die gleiche Höhe, wie weiter seitlich davon verdichtet sind, übersteigen die Druckkräfte im Film die Fließgrenze und folglich setzt sich der Schrumpf homogen fort.

Eine verdichtete Oberflächenschicht mit zurückgezogener Trocknungsfront (Transportwiderstand), widerspricht scheinbar der weiterhin konstanten Trocknungsrate, die sogar über den quasi vollständig geschrumpften Film hinaus anhält. Allerdings kann dieses Phänomen dem Kapillareffekt in den Porenecken zugeschrieben werden, welcher die Flüssigkeit an die Oberfläche des Films "pumpt" und dadurch die Trocknungsgeschwindigkeit aufrechterhält. Die Tatsache, dass diese Beobachtung bis quasi nach vollständigem Schrumpf anhält, führt zu der Hypothese, dass Poren in der Nähe des Substrats zumindest teilweise entleert sind, während die Poren in der Filmoberfläche noch gefüllt sind. Diese Hypothese ist gestützt durch vorangegangene substratnahe [ATR-FTIR](#) Messungen, in denen die Konzentration der Hauptphase in Kapillarsuspensionen signifikant früher gegenüber der Nullsuspension abnahm [8]. Unter Zuhilfenahme von Modellen dreiphasiger Fließphänomene in porösem Gestein, kann geschlossen werden, dass die wasserbasierten Kapillarbrücken einen höheren Eindringdruck gegenüber Luft besitzt und deren Trocknung durch das umgebende Heptanol zudem verzögert ist. Dies führt zu einem zusammenhängenden Flüssigkeitsverbund, der an die Filmoberfläche zur Trocknung transportiert wird und das weitere Eindringen von Luft in den Film unterbindet. Die Präsenz der Kapillarbrücken während der späteren Trocknungsphasen hat zudem einen tiefgreifenden Einfluss auf die Spannungen während der Trocknung. Die praktische Auswirkung des Kapillareffekts führt zu einer verlängerten konstanten Trocknungsrate, die kinetisch gasseitig kontrolliert ist und dadurch schnellere Trocknung ermöglicht. Darüber hinaus führt der zusammenhängende Flüssigkeitsverbund zu einer Beschichtung mit weniger isolierten, gefüllten Poren und dadurch geringerer Konzentration an Restlösemittel.

Die Abhängigkeit des Spannungsmaximums (d.h. die Neigung zur Rissbildung) von der Formulierung und den Trocknungsbedingungen wird in Kapitel 4 untersucht. Es zeigt sich eine Verbindung von der Stärke der Kapillarsuspension (Fließgrenze) und reduziertem Spannungsmaximum bei Trocknungstemperaturen von 30 °C und 40 °C in trockener Luft. Diese Reduktion kann mit dem stärkeren Partikelnetzwerk erklärt werden, welches den kompressiblen Schrumpfkraften entgegenwirkt. Wenn Wasser als Zweitflüssigkeit durch das gleiche Volumen Glycerin ersetzt wird, sinkt die Fließgrenze der entstehenden

Kapillarsuspension. Während der Trocknung kann ein weniger stark reduziertes Spannungsmaximum beobachtet werden, was die Abhängigkeit dessen von der Fließgrenze zeigt. Zudem besitzt Glycerin eine deutlich höhere Siedetemperatur (ca. 290 °C), wodurch es praktisch vollständig im Film in Form von Kapillarbrücken verbleibt und trotzdem nicht zu einer niedrigeren Spannungsspitze gegenüber Wasser führt. Aus diesem Grund scheint der Einfluss der Fließgrenze größer zu sein, als der des eher trocknenden Wassers. Um das mögliche Trocknen der Wasser-Kapillarbrücken zu unterdrücken und dadurch die Spannungsspitze dieser Kapillarsuspensionen weiter zu senken, wird die Luftfeuchtigkeit während der Trocknung erhöht. Entgegen der Erwartung hat dies keinen Einfluss auf das Spannungsmaximum bei einem Feststoffgehalt von $\phi_{\text{solid}} = 0.2$. Stattdessen wird bei erhöhter Luftfeuchtigkeit eine verringerte Spannung der Nullsuspensionen gemessen.

Im weiteren Verlauf wird der Einfluss eines erhöhten Feststoffgehalts in der Suspension untersucht. Aufgrund von Partikelwechselwirkungen weist die Nullsuspension eine höhere Viskosität auf. Das Volumenverhältnis von Zweitflüssigkeit und Feststoffanteil, $\phi_{\text{sec}}/\phi_{\text{solid}} = 0.125$, wird für Wasser und Glycerin beibehalten. Die Probe mit Glycerin weist wiederum eine niedrigere Fließgrenze auf. Erstaunlicherweise führt die Glycerin-Kapillarsuspension zu einer Reduktion der Spitzenspannung von ca. 40 % gegenüber der Nullsuspension und liegt damit unter der Spannung der Wasser-Kapillarsuspension. Dies deutet auf eine höhere Tendenz zur Trocknung der Wasser-Kapillarbrücken bei höherem Feststoffgehalt hin.

Es ist bekannt, dass die Spannung während der Trocknung von der Porengröße abhängt. Kleinere Poren führen zu größeren kompressiblen Spannungen bei der Trocknung. Mittels Kapillarsuspensionen können hochporöse Materialien hergestellt werden, sodass die beobachtete Reduktion der Spannung während der Trocknung auf die größeren Poren zurückzuführen sein könnte, anstatt auf das induzierte Partikelnetzwerk. Dank der in Kapitel 2 entwickelten Messmethode zur gleichzeitigen Bestimmung der Spannung und Gewichtsänderung einer Beschichtung, sowie der Kenntnis, dass ein Film seine maximale Spannung an dem Punkt erreicht, an dem der Film praktisch nicht mehr schrumpft, wird eine durchschnittliche Porosität bestimmt. Grundsätzlich zeigt sich eine höhere Porosität bei Erhöhung des Zweitphasenanteils und damit der Stärke der Kapillarsuspension. Wird jedoch die Porosität der Kapillarsuspensionen von Wasser und Glycerin bei gleichem Volumenanteil verglichen, so sind diese nahezu identisch, führen aber zu deutlich unterschiedlichen Spannungsmaxima. Dies deutet stark darauf hin, dass die Faktoren zur Reduktion der Spitzenspannung bei Kapillarsuspensionen ein Zusammenspiel zwischen der Fließgrenze, Mikrostruktur, Siedetemperatur der Zweitphase, sowie den Trocknungsbedingungen ist.

Um den Aspekt der Trocknung von Wasser-Kapillarbrücken näher zu untersuchen, wird eine gravimetrische Messung, gekoppelt mit einer Gasphasen Massenspektrometrie durchgeführt. Aufgrund der Überschneidung des Wasser- und Heptanolsignals, wird schweres Wasser zur Formulierung der Kapillarsuspension eingesetzt. Die Ergebnisse zeigen deutlich, dass während die Heptanol Gasphasenkonzentration bereits stark sinkt, die Wasserkonzentration erst mit einer Verzögerung folgt. Dieses Verhalten tritt bei 40 °C stärker auf, als bei 30 °C. Wenn bei höherer Temperatur die Heptanol Gasphasenkonzentration abfällt, bleibt die Konzentration schweren Wassers noch konstant. Zudem ist noch ein bedeutender Anteil schweren Wassers in der Gasphase, wenn Heptanol praktisch komplett verdampft ist. Diese Ergebnisse zeigen, dass gerade auch niedriger siedende Kapillarbrücken aus Wasser zwischen den Partikeln während der Trocknung verbleiben. Des Weiteren liefern diese Messungen zusätzliche Hinweise darauf, dass Kapillarsuspensionen das Eindringen von Luft in die Beschichtung unterdrücken und dadurch ein zusammenhängender Heptanolverbund gebildet wird, der zu einer niedrigeren Restkonzentration an Heptanol im Film führt.

Trotz dieser Erkenntnisse bleibt die Wechselwirkung von Wasser in der Kapillarsuspension und dessen Trocknung in feuchter Luft unklar. Eine genauere Betrachtung des flüssig-flüssig Gleichgewichts (LLE) von 1-Heptanol und Wasser (Kapitel 5) zeigt eine Mischungslücke auf. Während die Löslichkeit von 1-Heptanol in Wasser praktisch Null beträgt, löst sich Wasser in 1-Heptanol bei Raumtemperatur geringfügig (≈ 4 vol %). Allerdings ist dieser geringe Anteil genau in dem Bereich, der für die Formulierung von Kapillarsuspensionen notwendig ist. Deshalb stellt sich die Frage, wie sich eine Kapillarsuspension ausbilden kann, wenn der zugegebene Wasseranteil in Abwesenheit von Partikeln prinzipiell komplett in 1-Heptanol löslich ist. In anderen Forschungsarbeiten wurde die Temperaturabhängigkeit der Mischbarkeit von Partikeln ausgenutzt. Eine Temperaturänderung der homogenen Flüssigphase führte zu einer Phasenseparation unter Ausbildung von Kapillarbrücken zwischen dicht gepackten Glaskugeln [12]. Im Allgemeinen wird für die Formulierung von Kapillarsuspensionen die Zweitphase zugegeben, *nachdem* die Partikel in einem ersten Schritt bereits in der Hauptphase dispergiert wurden. Danach wird die Suspension in einem zweiten Schritt erneut dispergiert, was in einem metastabilen Zustand resultieren kann. Um dieses Verhalten näher zu untersuchen, wird Wasser in verschiedenen Mengen in 1-Octanol, 1-Heptanol und 1-Hexanol bei Raumtemperatur gelöst. Aus den Stammlösungen werden Suspensionen mit verschiedenen Partikeln hergestellt: die bereits eingesetzten, unregelmäßig geformten Al_2O_3 Partikeln, Glaskugeln mit 3 μm Durchmesser, und 0.39 μm große nanoaggregierte (Primärpartikelgröße ca. 20 nm) TiO_2 Partikel. Von den aus der Stammlösung hergestellten Suspensionen wird die Fließgrenze bestimmt und

mit der Fließgrenze der herkömmlich hergestellten Suspensionen, d.h. Wasserzugabe erfolgte in einem zweiten Schritt, verglichen. Erstaunlicherweise hat sich in allen Fällen eine Kapillarsuspension mit deutlich erhöhter Fließgrenze gegenüber der Nullsuspension gebildet. Dies zeigt, dass der dreiphasige Zustand in den untersuchten Kapillarsuspension nicht dem metastabilen Zustand entspricht, sondern den Gleichgewichtszustand widerspiegelt. Die Formulierung von Kapillarsuspensionen mittels in der Hauptphase gelösten Zweitflüssigkeit ohne Temperaturänderung, bildet die Basis für neue Anwendungsmöglichkeiten.

Die entdeckte partikelinduzierte Phasenseparation von in 1-Alkanol gelöstem Wasser führt zu der Frage, ob der beobachtete Einfluss der feuchten Luft auf das Spannungsmaximum bei der Trocknung der Nullsuspension in Zusammenhang mit der Mischbarkeit steht. Aus diesem Grund wird die mit verschiedenen Partikeln dispergierten 1-Alkanol Nullproben in einer geschlossenen Kammer mit wassergesättigter Luft über 150 Stunden gelagert. Danach wird die Fließgrenze bestimmt, wobei aufgrund der nicht stabilisierten Partikeln die Suspensionen zuvor erneut gemischt werden. 1-Hexanol, mit der höchsten Wasserlöslichkeit der untersuchten Alkanole, weist einen signifikanten Anstieg der Fließgrenze für die Proben aus Aluminiumoxid und Glas auf. Darüber hinaus zeigen die Glasproben einen Anstieg der Fließgrenze aller untersuchten Alkanolen, die über den Zeitraum hoher Luftfeuchtigkeit ausgesetzt waren. Dieses bemerkenswerte Ergebnis impliziert, dass eine dünne Beschichtung bestehend aus einer leicht wasserlöslichen, kontinuierlichen, öligen Phase und einer großen Oberfläche, Wasser aus feuchter Luft absorbiert, was dann zu Phasentrennung in Form von Kapillarbrücken zwischen den Partikeln führen kann.

Im zuvor vorgestellten Spannungsmessapparat wurden Messungen in trockener Luft, sowie unter hoher Luftfeuchtigkeit (ca. 85 %) bei Raumtemperatur durchgeführt. Die untersuchte Probe, Al_2O_3 dispergiert in Heptanol, zeigt hierbei ein deutlich reduziertes Spannungsmaximum und weist weitere typische Trocknungsmerkmale einer Kapillarsuspension, wie einen verlangsamten Spannungsabfall, auf. Daraus folgt, dass die Trocknung in feuchter Luft, nicht nur das Verschwinden von Kapillarbrücken in Kapillarsuspensionen unterdrückt, sondern bei ausreichend langsamer Trocknung, sich auch Wasser-Kapillarbrücken in Nullsuspensionen ausbilden können. Dies führt zu niedrigeren Spannungen im Film und deshalb zu einer reduzierten Rissanfälligkeit und Defekten. Diese Erkenntnisse sind auch von Wichtigkeit für Suspensionen, welche eine kleine Wasserlöslichkeit besitzen und in feuchter Umgebung gelagert werden, da dies zu ungewünschter Gelbildung führen kann.

Abschließend werden die zuvor detailliert beschriebenen Erkenntnisse in Kapitel 6 kurz zusammengefasst und mögliche weitere Untersuchungen beschrieben. Darunter sind Verbesserungen des Messaufbaus zur Spannungsmessung selbst, wie auch die Erweiterung zur *in situ* Messung des Filmprofils. Ein realistischerer Vergleich der Spannungen

durch Unterdrücken der seitlichen Trocknung, würde mittels Entwicklung eines bewehrten Kragträgers ermöglicht. Des Weiteren kann die Sichtbarmachung der Phasenseparation und Bildung von Kapillarbrücken aus der Lösung unter einem Konfokalmikroskop weitere Aufklärung über die Vorgänge hervorbringen.

Summary

Hard particle coatings are ubiquitous in daily life. They can be found in wood paints, where embedded particles scatter UV light and prevent damage to the wood [1], or in marine coatings to protect surfaces from corrosion [2]. A recently popularized application for such coatings is that of printed electronic circuits, batteries, solar cells and other features [3–6]. One driving force is the inexpensive production of devices such as radio frequency identification (RFID) tags on flexible substrates for the internet of things (IoT) [7]. In order to obtain operational products, the functional particles have to be dispersed in a fluid and rheologically tailored to appropriately apply the coating onto the substrate. Afterwards, the bulk liquid needs to be evaporated to obtain a dry coating. During this step, however, drying stresses occur, which can manifest in cracks and other drying defects. These shortcomings can be prevented by adding polymeric binders and surfactants. However, these additives need to be removed after drying by means of temperature treatments. This annealing process again poses the risk of fracture and, more importantly, can be destructive to polymeric substrates with low glass transition temperatures. In our previous work, we found that capillary suspensions can suppress cracking during drying [8]. This class of suspensions, recently discovered by Koos and Willenbacher [9], possesses the characteristics needed for printing applications [10, 11] and can be comprised of only volatile components, making subsequent processing steps superfluous.

This dissertation strives to improve our understanding of the drying behavior of capillary suspensions and the underlying mechanisms of stress development based on experimental findings. In order to investigate the stress evolution and drying behavior of any kind of coatings, a measurement setup had to be designed and built, as described in [chapter 2](#). The employed measurement technique is called “cantilever deflection method”. It is the predominant technique for determining stresses during drying of coatings under controlled conditions. Besides the stress, the drying rate of a coating is of additional interest. The drying rate allows one to draw conclusions about morphological changes, such as retraction of the liquid into the film, which results in mass transport resistances and hence slows down the drying rate. So far, this measure has been obtained by placing a second coated substrate inside the chamber on a weighing tray. The two different measurements – stress

and drying rate – were treated as if it were obtained from a single film. A problem that arises is the fact that the invisible temperature gradients may cause differences between the films, falsifying observations. Additionally, one assumes that the coating shape, thickness, and drying behavior of the two films are identical. This assumption may still be valid when applying low viscosity coatings, but as the coatings become more viscous or even elastic (gelled), as is the case in capillary suspensions, the films always exhibit variations in the wet film profile. This is due to coating and edge effects from the substrate. Therefore, I designed a modernized cantilever deflection technique that is capable of simultaneously measuring the stress and drying rate of a coating in a chamber with adjustable temperature and humidity. Design details include a magnet with a latch mechanism to prevent cantilever yaw, roll and pitch, as well as a camera that can track visual changes of the coating. Moreover, a sophisticated cantilever fixture inserting and lifting tool assures rapid introduction of the sample into the chamber as well as attachment to the magnet with correct orientation at a repeatable measurement position. A coating rig was milled to precisely fit the cantilever fixture in a recess. A weak magnet on a support ensures an equal position and height of the polished steel substrate. A height adjustable coating blade is then dragged at a variable speed over the cantilever. All peripheral measurement devices such as stylus height profiler, temperature and humidity sensors, calibration device, scale and laser position sensor were connected to a computer and recorded with LabView, as detailed in [chapter 2](#).

The developed stress measurement apparatus is the foundation for further studies of capillary suspension drying. In [chapter 3](#), we make use of the visual observation capabilities and relate changes in the coating appearance with its stress evolution behavior. The examined model capillary suspension is in the pendular state, i.e. the small amount of added liquid preferentially wets the particles. The continuous liquid is 1-heptanol in which Al_2O_3 particles with a $d_{50,3} = 0.5 \mu\text{m}$ are suspended. Particle network formation is induced by adding 2.5 vol% ultra-pure water and subsequent mixing in a high shear mixer. The formulation results in a suspension with a particle volume fraction of $\phi_{\text{solid}} = \phi_{\text{Al}_2\text{O}_3} = 0.2$. We then examined the drying of a regular suspension without added water and the capillary suspension in dry air at a temperature of 40 °C. As already observed by other researchers, the regular suspension clearly shows lateral drying when the film is dried on a cantilever. That is, the coating dries at the edges first due to a higher evaporative flux. This phenomenon directly translates to an accelerated stress increase and decrease of the overall drying rate. At the edges, however, the pinning of the contact line causes a mass flow of the solvent from the film's center, which drags particles to the edges (coffee-ring effect). This particle accumulation at the edges leads to a particle depletion

in the center of the cantilever, referred to as trench, and pinholes. These defects can render coatings unusable and are generally not desired. In contrast, we found that the capillary suspension samples do not show signs of these drying defects. Moreover, an accelerated stress increase coincides with the appearance of a dry surface in the capillary suspension coating. Interestingly, the overall drying rate remains practically constant for long times, even beyond the point of full consolidation (beyond the peak stress). In order to investigate the mass flow of the continuous phase, we dyed the heptanol. The regular suspension clearly shows dye accumulation at the edges for the regular suspension, confirming solvent and particle transport. In contrast, the capillary suspension only shows minimal dye accumulation, indicating a different flow behavior during drying. While we can exclude major heptanol flow in the capillary suspension sample, we cannot exclude movement of particles or capillary water bridges to the edges. Therefore, we dyed the water liquid bridges with a water soluble dye and found a uniform color distribution on the coating, suggesting that water bridges and particles dry uniformly without migrating towards the edges.

In order to elucidate the shrinkage behavior of both suspensions during drying, we performed *ex situ* height profile measurements. The results show that the regular suspension dries predominantly near the edges, leading to consolidation while the center has shrunk but is still supersaturated. In stark contrast, the capillary suspension behaves fundamentally different. As expected, the edges also dry first, although to a much lesser extent. However, the shrinkage near the edges stops at some point, while the supersaturated center continues to dry until a profile with nearly identical uniformity as the wet coating is obtained (e.g. the shrinkage is uniform across the full sample width). It is only at this point that shrinkage continues, but now, the surface shrinks uniformly and predominantly in height while retaining its shape until full consolidation of the coating is achieved. We explain this behavior by an increase in yield stress near the edges that balances the compressive forces during drying of the edges. Once the supersaturated region has evaporated, the compressive stress becomes larger than the yield stress of the coating and, thus, the sample continues to shrink.

A consolidated upper layer (increased mass transport resistance) seemingly contradicts the measured constant drying rate that lasts even beyond full compaction. However, we attribute this phenomenon to capillary corner flow that “pumps” the liquid to the surface, maintaining a constant drying rate. The fact that it continues beyond compaction leads to the hypothesis that the particle layers near the substrate are at least partially dry when the surface layers are still saturated. This hypothesis is supported by previous [ATR-FTIR](#) measurements [8], in which the concentration of the bulk liquid measured near

the substrate appeared to dry significantly faster. Using models from three phase flow phenomena in porous rocks, we conclude that capillary water bridges have a higher air invasion pressure and their evaporation is delayed by the surrounding heptanol. This leads to a connected continuous liquid cluster that is transported to the surface of the film preventing further air invasion. The presence of these higher vapor pressure bridges during the later stages of drying also has a profound impact on the drying stress. The practical result of the capillary corner flow is a prolonged constant rate period that can be kinetically controlled by air flow conditions (e.g. enabling faster drying). Moreover, the connected liquid cluster in capillary suspensions leads to lower undesired residual solvent in the dry coating. From the visual observations and profile measurements, we conclude that capillary suspensions lead to more homogeneous and defect free coatings without the need for subsequent processing.

The dependence of the peak stress, i.e. its proneness to cracking, on the coating formulation and the drying conditions is investigated in [chapter 4](#). Beginning with the capillary suspension strength (yield stress), we find a correlation between yield stress and reduced peak drying stress at both 30 °C and 40 °C in dry air. This can be explained by the stronger particle network in capillary suspensions that resists shrinkage. When the secondary liquid water is exchanged for the same volume fraction of glycerol, the yield stress in the capillary suspension decreases. As a result, the peak stress does not decrease as much as with the same volume of water, showing the effect of the yield stress on the drying stress. Glycerol also has a higher boiling point and is not expected to evaporate. Despite these long lasting bridges, the peak stress is not lower compared to the water capillary bridges. Therefore, the effect of the yield stress appears to dominate over water evaporation. In order to address potential drying of the water bridges, we increased the humidity during drying and expected that the suppressed water evaporation will further lower the peak stress for the water capillary suspensions. However, we did not find dependence of humidity on the peak stress at $\phi_{\text{solid}} = 0.2$. Instead, we observe a peak stress reduction of the pure suspension at higher humidities.

We then examined the influence of an increased solid content of $\phi_{\text{solid}} = 0.25$ the suspension. Due to increased particle-particle interactions, the regular suspension is more viscous. The ratio of $\phi_{\text{sec}}/\phi_{\text{solid}} = 0.125$ for water and glycerol remained constant but, as before, the yield stress is lower for the glycerol sample. Surprisingly, we find that the glycerol sample reduces the peak stress by approximately 40% compared to the pure suspension, which is more than the water capillary suspension, indicating an effect of the bridges' tendency to evaporate at the higher solid loading.

The peak stress is also known to depend on the film porosity. Smaller pores cause larger compressive drying stresses. Capillary suspensions can be used to create highly porous materials, therefore the stress decrease could be caused by larger pores and not the network effect. Thanks to our developed simultaneous stress and weight measurement device and the fact that a fully consolidated film is obtained when the peak stress is reached, we can calculate the average film porosity. Indeed, we find a lower coating porosity with increasing secondary liquid content. However, when comparing the porosity of the same volume water and glycerol capillary suspension, we find almost identical porosities of the dry films but clear variations in peak stress. This strongly suggests that the factors for the peak stress reduction is an interplay between the capillary suspension's yield strength, microstructure, and secondary liquid's vapor pressure as well as drying conditions.

In order to investigate the tendency of the water capillary bridge to evaporate, we performed a thermogravimetric analysis (TGA) coupled with head space mass spectrometry (MS). Due to an overlay in mass peaks, we used heavy water to formulate the capillary suspension. The results clearly showed that when the amount of heptanol in the gas phase drops, there is a delay in the reduction of the heavy water concentration. This behavior is even more pronounced at 40 °C than 30 °C. When the heptanol head space concentration starts to decrease, heavy water remains nearly constant. Additionally, when heptanol evaporation has virtually stopped, there is still a significant amount of heavy water detected in the gas phase. These findings reveal that the capillary water bridges, despite a higher vapor pressure, persist in the coating during drying. Moreover, it provides further evidence that capillary suspensions inhibit air invasion during drying, thus maintaining the connected heptanol cluster, which leads to lower residual heptanol in the coating.

Despite these findings, the interaction of water in the capillary suspension and during the drying thereof into humid air remains unclear. Examining the liquid-liquid equilibrium (LLE) of 1-heptanol and water (chapter 5) reveals a miscibility gap with a mutual solubility. The solubility of 1-heptanol in water is practically zero, while the miscibility of water in 1-heptanol is small but nonzero at room temperature (≈ 4 vol%). Importantly, this fraction is in the range used to formulate capillary suspensions. Thus, the question arises how a capillary suspension can form when the amount of water added is completely miscible in heptanol in the absence of particles. Other researchers made use of the temperature dependent phase separation in wet granular media, where the temperature change induced the growth of capillary water bridges between densely packed glass beads [12], but no temperature-induced phase separation is employed here. In general, capillary suspensions are formulated by adding the secondary phase *after* the particles have already been

dispersed in the continuous phase in a first step. Afterwards the suspension is dispersed again in a second step. This may lead to a meta-stable state. To further elucidate this behavior, we used the 1-alkanol series from 1-octanol, 1-heptanol, and 1-hexanol in the order of increasing water miscibility at room temperature and dissolved certain amounts of water in a stock solution. We then added different particles: the previously used, irregularly shaped Al_2O_3 particles; 3 μm spherical glass beads; and 0.39 μm sized nano-aggregate TiO_2 (20 nm primary particle size). The particles were then mixed in a high shear mixer and the yield stress was compared with the respective material system formulated in the conventional way, e.g., by adding water after suspending the particles in the 1-alkanol bulk phase. In all cases, we found a drastically increased yield stress compared to the respective pure suspension. This shows that the three-phase capillary suspension state is an equilibrium state rather than a meta-stable state. Using secondary liquids dissolved in the bulk phase opens up new pathways of formulating capillary suspensions without the need to induce a phase separation through a temperature change.

The discovered particle induced phase separation of dissolved water in 1-alkanols posed the question if the observed influence of the humidity on the stress development is somehow related to the miscibility. Therefore, we stored pure 1-alkanol samples with the respective initially suspended particles at room temperature in an enclosed chamber with water saturated air over 150 hours. Due to the non-stabilized suspensions, we re-mixed the samples prior to determining the yield stress. The results for 1-hexanol, with the highest water solubility in the series, exhibited a significant increase in yield stress for the alumina and silica system. Moreover, the silica samples showed an increase in yield stress for all tested 1-alkanols exposed to humid air over the examined period of time. This remarkable result implies that when thin coatings with a large surface area, composed of a slightly water soluble continuous phase, are exposed to humid air, water can dissolve in the coating and subsequently phase separate between the particles forming capillary water bridges as in capillary suspensions. A drying experiment performed in our designed apparatus with alumina particles suspended in heptanol, dried at room temperature and 85% relative humidity, showed a drastically reduced peak stress. The stress curve for the pure suspension dried in humid air displays typical features of a drying capillary suspension, such as a slow stress release. Thus, we can conclude that drying capillary suspensions, and even regular suspensions, in humid air not only suppresses capillary water bridge evaporation but can actually form capillary bridges at sufficiently slow evaporation rates. As a result, these coatings exhibit lower peak stresses and, hence, are less prone to cracking and drying defects. This finding is also of interest when particle formulations with small water solubility are stored in humid environments, which can lead to undesired gelling.

Finally, in [chapter 6](#), these results are briefly summarized and some potential subsequent research is discussed. This includes improvements to the stress measurement apparatus itself as well as expanding the simultaneous measurements with *in situ* film profiling. Developing a walled-cantilever design, which significantly suppresses lateral drying, enables a more realistic comparison of stress values during drying. Furthermore, a visualization of capillary bridge formation from solution with confocal imaging can shed light on the phase separation process.

Contents

Preface	i
Acknowledgements	iii
Abstract	vii
Summary	xvii
Nomenclature	xxix
1 Introduction	1
1.1 Stress formation during drying	2
1.2 Suspension drying	3
1.3 Capillary suspensions	4
1.4 Stress characterization	10
1.5 Film stress measurements	12
1.6 Motivation and goal of this work	13
1.7 Manuscript outline	14
2 Apparatus for simultaneous stress and weight measurement	17
2.1 Abstract	17
2.2 Introduction	18
2.3 Stress measurement techniques	18
2.4 Design of the stress measurement setup	21
2.4.1 Apparatus setup	21
2.4.2 Drying chamber	22
2.4.3 Coating procedure	23
2.4.4 Inserting and attaching procedure	25
2.4.5 Data acquisition	27
2.4.6 Calibration	28
2.5 Application Example/Results	30
2.6 Conclusions	31
3 Using an added liquid to suppress drying defects	33
3.1 Abstract	33

3.2	Introduction	34
3.3	Materials and Methods	36
3.3.1	Sample preparation	36
3.3.2	Coating process	37
3.3.3	Stress measurement and drying chamber	38
3.3.4	Film shrinkage	39
3.3.5	Surface profilometry	39
3.4	Results	40
3.4.1	Comparison of stress curve features with drying images of a coating	40
3.4.2	Dyed samples	43
3.4.3	Cross sectional profile change during drying	47
3.5	Discussion	50
3.6	Conclusions	55
3.7	Supplementary material	58
4	Influence of drying conditions on the stress and weight development of capillary suspensions	61
4.1	Abstract	61
4.2	Introduction	62
4.3	Materials and Methods	64
4.3.1	Sample preparation	64
4.3.2	Coating process	65
4.3.3	Stress measurement in the environmentally controlled drying chamber	66
4.3.4	Shear yield stress measurements	68
4.3.5	Thermogravimetric analysis with mass spectrometry (TGA-MS)	68
4.4	Results and Discussion	70
4.4.1	Stress development differences in capillary suspensions	70
4.4.2	Peak stress comparison	75
4.4.3	Film morphology at the peak: Residual fluid	78
4.4.4	Residual saturation	81
4.4.5	Capillary bridge evaporation	83
4.5	Conclusions	86
5	Capillary bridge formation at room temperature in binary liquids with small miscibility	89
5.1	Abstract	89
5.2	Introduction	90
5.3	Materials and Methods	92
5.3.1	Materials	92
5.3.2	Sample preparation	95
5.3.3	Yield stress measurements	96
5.4	Results and discussion	97
5.4.1	Yield stress comparison with different formulation routes	97

5.4.2	Residual water content	99
5.4.3	Effect on drying applications	106
5.5	Conclusions	108
5.6	Supplementary material	110
6	Summary and Outlook	111
	List of Figures	117
	List of Tables	121
	List of Publications	123
	Journal articles	123
	Conference contributions	124
	Oral presentations	124
	Poster presentations	125
	Bibliography	127

Nomenclature

Acronyms

ATR	attenuated total reflectance
CMC	carboxymethyl cellulose
CRP	constant rate period
CT	computed tomography
DAQ	data acquisition
FRP	falling rate period
FTIR	Fourier-transform infrared spectroscopy
IoT	internet of things
IP	invasion percolation
KIT	Karlsruhe Institute of Technology
KUL	KU Leuven
LLE	liquid-liquid equilibrium
MID	multiple ion detection
MS	mass spectrometry
PID	proportional integral differential
PSD	position sensing detector
RFID	radio frequency identification
RH	relative humidity
SMaRT	Soft Matter, Rheology and Technology

TGA	thermogravimetric analysis
USB	universal serial bus

Latin symbols and variables

A_{131}	Hamaker constant. Interaction potential between material 1 and material 3
c	concentration
$c_{\text{H}_2\text{O}}^0$	water concentration at standard conditions
d	cantilever deflection
$d_{50,3}$	volumetric median particle diameter
E	Young's modulus
F_c	capillary force
h	Planck constant
k_B	Boltzmann constant
L	length
m_{final}	film weight after drying
m_{liquid}	liquid weight
n	refractive index
n	number of carbon atoms
p_c	capillary pressure
P_y	compressive yield stress
r_i	principal radius of species i
R	ideal gas constant
s	distance between spheres
t	thickness
T	absolute temperature
V	volume

$V_m^{\text{H}_2\text{O}}$ molar water volume

Greek symbols and variables

$\gamma_{i/m}$ interfacial tension between species i and species m

γ shear strain

ϕ_{solid} particle volume fraction

$\phi_{\text{H}_2\text{O}}$ water volume fraction

ϕ_{sec} secondary liquid volume fraction

ϵ dielectric constant

$\bar{\nu}_e$ mean main electronic adsorption frequency

σ stress

σ_y shear yield stress

ν Poisson's ratio

θ contact angle

ξ floc radius

General subscripts

solid solid

s substrate

c coating

l liquid

v vapor

1 Introduction

The recent digital transformation in industry and society is largely driven by the internet of things (IoT) in which devices are connected and communicate. A big role in that technology is fulfilled through radio frequency identification (RFID) tags and other sensors [7], electrically conductive circuits that must be produced at low cost and in high numbers. A cost-efficient method for their production is accomplished through established printing technologies, such as screen printing or inkjet printing [13]. Applications for printed electronic devices range from RFID and other sensors to Li-ion batteries [4, 6]. However, obtaining an optimized finished product entails many challenges, starting with the formulation of conductive suspensions to render the conductive material applicable. The conductive particles are embedded in a liquid matrix and enriched with thickening agents, binder, and surfactants to ensure proper application and an inherent stability of the film during processing. However, the additives remain in the film and inhibit the formation of a conductive percolating network, which requires further processing steps such as curing at elevated temperatures. This can be problematic when flexible substrates with low glass transition temperatures are used [14].

In general, films and coatings from particulate suspensions are ubiquitous and can be found in many areas where surfaces need to be protected, such as in marine coatings [2], scratch resistant coatings in automotive applications, and paints [1]. In each of these applications, the carrier liquid has to evaporate after successful application to form a defect free dry film. A failed film causes conductivity loss in printed electronics, rust in marine applications, or wood rot in paints. Therefore, drying represents a crucial step in film formation. Understanding the mechanisms underlying the drying behavior of a formulation is essential for a successful product development.

Drying of particle suspensions can be divided in two principal stages: The constant rate period (CRP) and the falling rate period (FRP) [15]. During the CRP, the suspension dries at a rate close to or equal to that of the bulk fluid because the air-suspension interface is equal to that of air and the bulk liquid without mass transport resistances in the film. While the drying rate does not change during this period, the thickness of the particulate film shrinks due to volume loss of the evaporated liquid. Other effects include the change

of microstructure in terms of a spatial variation in particle concentration. In stabilized suspensions with particle mobility, Cardinal et al. [16] mapped different drying regimes that can predict the microstructure of a drying film. They found that the local particle concentration depends on the drying rate as well as the particle diffusivity and size. In the evaporation dominated regime, a consolidated particle layer forms at the top of the film by particle accumulation. In the sedimentation regime, the particles settle and accumulate at the substrate. Both inhomogeneities can be countered by a higher particle diffusivity, which leads to a uniform particle distribution in the diffusion dominated regime. In practice, for example, this can be observed via a spatial distribution for additives in green tapes for ceramic bodies [17], in skin formation in polymeric coatings[18], or as binder migration during drying of Li-ion batteries [19, 20]. At some point during evaporation, the particles within the film have fully consolidated and formed a microstructure. This structure inhibits the evaporation and the drying rate transitions into the FRP. The phenomenological mechanisms are further discussed in the next section.

1.1 Stress formation during drying

During the initially uninhibited drying rate, a microstructure starts to develop, which influences the aforementioned drying regimes. At some point, often when the film has fully shrunk, the liquid film covering the upper surface particles starts to recede into the void space between particles (pores). Depending on the wetting of the particles by the drying fluid and pinning of the liquid on the particles, the liquid cannot recede into the particle film. The surface tension between the liquid and air then forms a curved menisci, as shown in Figure 1.1a. Depending on the aggregation behavior and drying conditions, the particles can have a wide distribution of separation distances. The space between particles can be imagined as capillary tubes with different radii $r_1 \dots r_n$. The capillary rise observed inside two tubes with radii r_1 and r_2 , and a three phase contact angle (air-water-glass) θ is shown in Figure 1.1b. The reason for the rise is the interfacial tension and the resulting upward capillary force. This force creates a negative Laplace pressure in the tube liquid, which in turn pulls liquid from the reservoir into the tube until an equilibrium between capillary pressure and hydrostatic pressure is reached. The capillary pressure difference p_c is described by the Young-Laplace equation:

$$p_c = \frac{2\gamma_{lv} \cos \theta}{r} \quad (1.1)$$

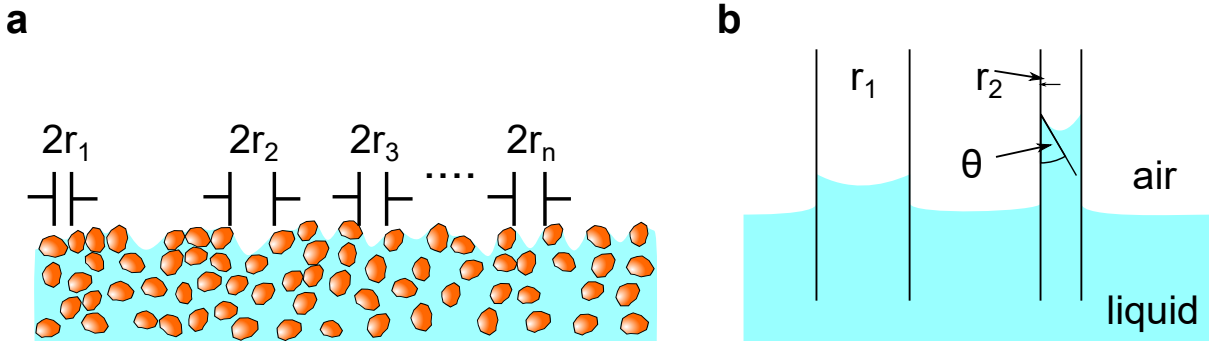


Figure 1.1: (a) Meniscus formation in a drying coating. r_1 to r_n denote the radii of the meniscus inscribing the space between particles. (b) A capillary tube inserted in a wetting liquid. Due to the surface tension the liquid level rises inside the tubes with contact angle θ . Due to the smaller radius $r_2 \leq r_1$ the water level rises higher in the smaller tube.

Where the capillary pressure p_c , depends on the liquid-vapor interfacial tension γ_{lv} , the contact angle θ , and the radius of the capillary tube r . Translating the capillary tube behavior to the porous film, the curved menisci can cause capillary flow from the film interior to the surface, while exerting a compressive pressure on the surrounding particles because the liquid cannot rise above the surface layer. Upon initial small curvature, the continued evaporation causes a decrease in contact angle θ and thus an increase in capillary pressure according to Equation 1.1. If the particle film comprises soft particles (above film forming temperature), such as latex, the increasing stress causes particle deformation and coalescence, which relaxes the stresses [21, 22]. However, the stress cannot be relieved by deformation when hard particles, such as ceramics, are used. Therefore, according to Griffith's criterion for brittle materials, if an energy release gained by forming a new surface is larger than the surface tension energy created by the surface, then cracking occurs, which releases the stresses evolved during drying of a coating [23, 24].

1.2 Suspension drying

Drying of a sessile droplet differs significantly from free floating droplets in air. While the floating liquid droplets dry uniformly in all directions, the substrate in sessile drops limits the direction and type of drying. Two extremes can be observed for sessile droplets drying on a substrate: drying of the droplet with a constant radius but changing contact angle; or drying with a constant contact angle and shrinking radius [25]. In reality, both states usually occur sequentially during drying, depending on the interplay of fluid and substrate properties [26]. At a contact angle $\theta = 90^\circ$, the drying rate is constant across the drop surface, as illustrated in Figure 1.2a. At a contact angle of $\theta \leq 90^\circ$, the droplet dries in the constant radius mode for more than 90% of the drying time [27]. The reason

for this phenomenon is the substrate surface roughness that pins the three phase contact line, resulting in a change to the contact angle. This interaction between liquid and substrate influences the local drying rate across the surface [27, 28]. At smaller contact angles, the drying rate has a mathematical singularity at the contact line that manifests in a significantly increased drying rate near the contact line compared to the center of the droplet, as sketched in Figure 1.2b [29]. This behavior has a noticeable effect during drying of particle laden droplets such as coffee. Instead of leaving a uniform layer of particles after drying, one observes coffee stains at the perimeter of the initial droplet. Deegan et al. [28], were the first to identify the increased drying rate at the contact line, as the reason for the coffee-ring effect. The pinned contact line with an angle of less than 90° causes an increased drying rate near the edge. For the contact line to remain pinned, the evaporated liquid needs to be replenished from the center of the droplet via liquid mass flow towards the edges. The induced flow carries particles to the contact line as sketched in Figure 1.2c. The deposited particles form a compact structure that further promotes pinning and meniscus formation between the particles induces capillary flow [26, 28]. The same mechanism occurs in suspensions with higher volume fractions but the effect can become less noticeable. It is worth noting that the Kelvin equation, which describes the vapor pressure of a droplet, only has a significant influence at very small droplet sizes in the μm to nm range.

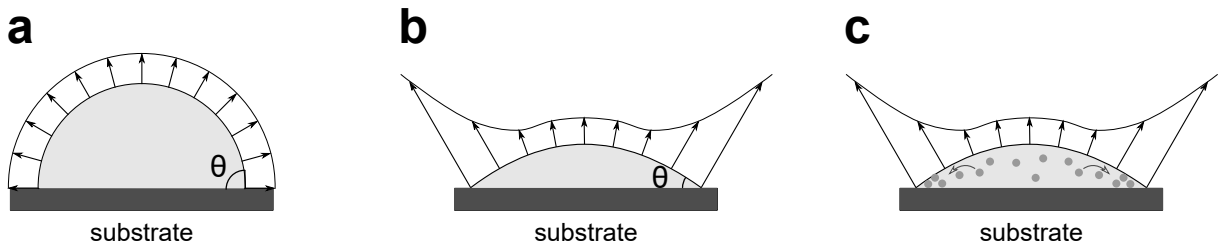


Figure 1.2: (a) A sessile droplet with a three phase contact angle of $\theta = 90^\circ$ causing a homogeneous drying rate across the surface illustrated with arrows. (b) At contact angles $\theta \leq 90^\circ$ the drying rate is significantly increased near the contact line. (c) Schematic of the coffee-ring effect. Particles are carried to the contact line where they deposit. This promotes pinning and induces capillary flow from the center to the edges.

1.3 Capillary suspensions

Generally speaking, suspensions are particles distributed in a carrier liquid. The particle size strongly influences a suspension's behavior towards aging. While small, colloidal particles in the nanometer range are small enough to be affected by thermal (Brownian) motion, larger particles have no thermal motion and, if there is a density difference, they

will eventually float on top of the liquid if lighter or settle if denser [30]. However, this is only true when the particles do not interact with each other. In reality, attractive forces between particles cause them to aggregate and form larger clusters creating inhomogeneities and flocs in suspensions. This behavior can be suppressed by modifying the particle-particle interactions. Surfactants or polymers adsorb to the particles and create steric repulsion that prevents particle-particle contact. Similarly, charged particles are electrostatically stabilized and can be combined with charged surfactants or a charged polymer layer, resulting in electrosteric stabilization [30, 31].

A weakly stabilized suspension formulation can undergo slow aggregation and is destroyed over time. Alternatively, suspensions with strong stabilization can be deliberately destabilized by adding salts to diminish the repulsive interactions between particles and even to allow attraction to dominate, leading to agglomeration. This induced flocculation is often employed in wastewater treatment [32]. A floc is a fractal arrangement of particles with voids. If the volume fraction of particles in a sample is sufficiently high, the flocs can form a sample spanning percolating network. This structural arrangement, with solid-like behavior, is termed a gel [30].

Koos and Willenbacher [9] observed a drastic change in rheological properties after a small amount of water was mixed with particles suspended in oil and vice versa. Small amounts of added liquid, in the range of a few volume percent, caused the suspensions to transition from a fluid-like state to a highly elastic, solid-like state with a yield stress, as shown in Figure 1.3a. Interestingly, the addition of the secondary liquid transitions the sample towards an elastic specimen regardless of whether the added fluid preferentially wets the particles or not. The reason for the increase in elasticity is the formation of capillary bridges formed by the secondary fluid between the particles resulting in a liquid-liquid-solid state. If the added liquid preferentially wets the particles, i.e. exhibits a three phase contact angle $\theta_{\text{sec}} \leq 90^\circ$, the bridge forms pendular bridges, hence it is called the pendular state. A schematic of the bridge is shown on the inset of Figure 1.3a on the left. The capillary state has a the three phase contact angle $\theta_{\text{sec}} \geq 90^\circ$. The particles arrange around the added liquid to reduce the length of the interfacial area, thereby “shielding” the non-wetting fluid from the bulk liquid [33, 34]. Microscopic images of the two states with glass beads and dyed water are shown in Figure 1.3b. Surface treatment renders the glass beads either hydrophilic or hydrophobic, leading to the pendular networks (Figure 1.3b.i), or to the capillary state networks (Figure 1.3b.ii) respectively. The existence of these two states has additionally been shown by confocal microscopy imaging in several publications [35–40].

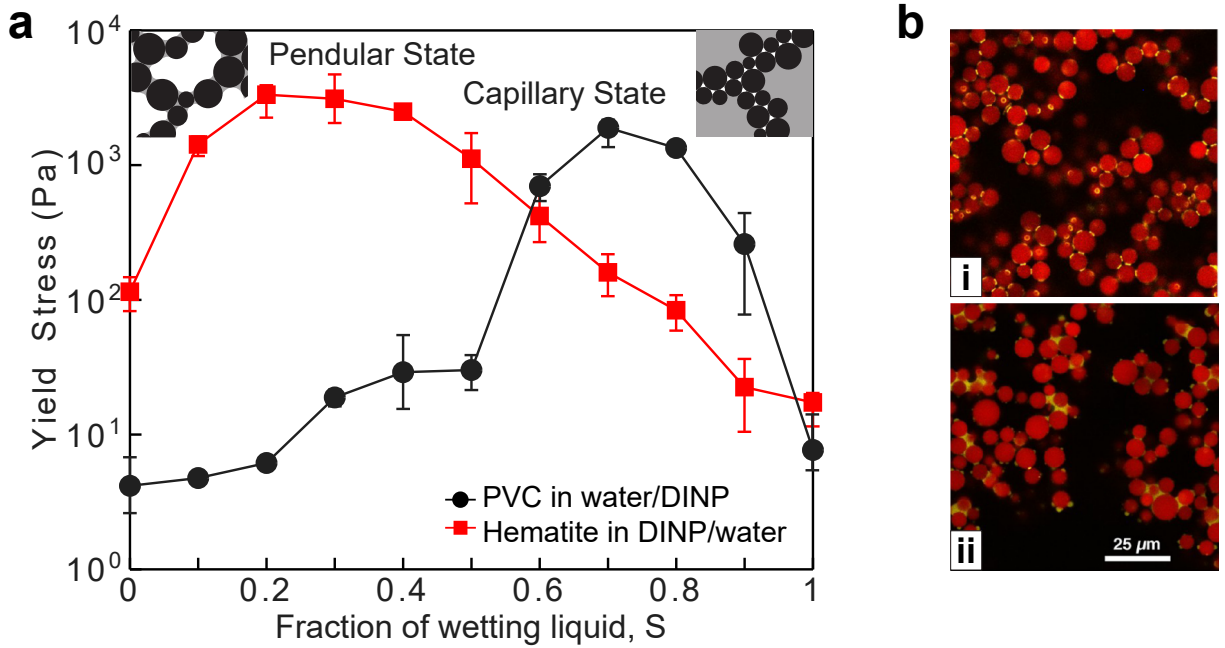


Figure 1.3: (a) Addition of a liquid immiscible with the bulk liquid of a suspension increases its yield stress by orders of magnitude. This behavior occurs irrespective of the secondary liquid’s wetting properties. The preferentially wetting case leads to the pendular state, while the non-wetting case leads to the capillary state. (b) Confocal images of capillary suspensions with the secondary liquid (water) dyed yellow. (b.i) shows glass beads (red) with a hydrophilic surface leading to the pendular state with $\theta = 61^\circ$ while (b.ii) depicts the capillary state with $\theta = 94^\circ$ resulting from the hydrophobic surface. Subfigure (a) is reproduced with permission from AAAS [9] and Elsevier [34]. Images in subfigure (b) are reproduced with permission from ACS [35].

The change in sample appearance can easily be seen by increasing the amount of water. In accordance with the particle volume fraction, the amount of secondary liquid is denoted as ϕ_{sec} and is defined as volumetric ratio of secondary liquid over total volume. At a low level between $0 \leq \phi_{\text{H}_2\text{O}} \lesssim 0.04$ (depending on the suspension system), the yield stress drastically increases [10]. The effect can be visualized with a simple tilt test as pictured in Figure 1.4. Samples with increasing amounts of water (from left to right), but constant fraction of alumina particles suspended in 1-heptanol, were placed on a board. Then, the plate was tilted to approximately 45° for several seconds and the result is shown in Figure 1.4a. The sample on the far left without added water ($\phi_{\text{H}_2\text{O}} = 0$) started flowing and flows the furthest. The second sample with $\phi_{\text{H}_2\text{O}} = 0.01$ did not flow as far and the following samples did not flow at all. Additionally, the protrusion out of the plane without spreading for the last sample ($\phi_{\text{H}_2\text{O}} = 0.03$) indicating a larger yield stress, is visible. Upon further a tilt to $\approx 80^\circ$ (Figure 1.4b), the first two samples continue to flow. In contrast, the third sample ($\phi_{\text{H}_2\text{O}} = 0.02$) is now found further away from its starting point while retaining its original shape to a large degree. This clearly indicates another feature of capillary suspensions: slip. A thin oil film between the board and sample allows the

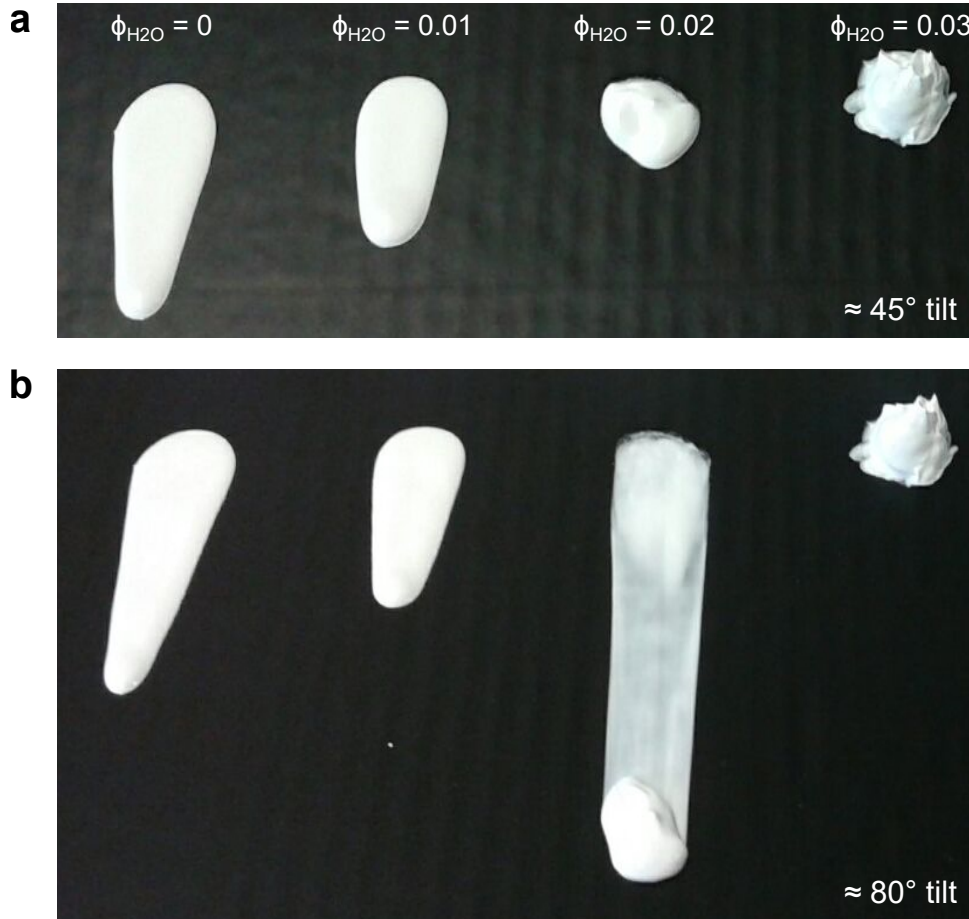


Figure 1.4: Example of the visual change in a sample's yield stress and flow behavior for alumina particles suspended in heptanol and addition of small amounts of water (from $\phi_{\text{H}_2\text{O}} = 0$ to $\phi_{\text{H}_2\text{O}} = 0.03$) at a tilt of (a) $\approx 45^\circ$ and (b) $\approx 80^\circ$ of the substrate. Increasing the amount of water significantly increases the sample's yield stress.

specimen to move without shearing the rest of the sample. The specimen on the far right ($\phi_{\text{H}_2\text{O}} = 0.03$) was unaffected by tilting and exhibited neither flow nor slip.

Besides its high yield stress, another rheological property of a capillary suspension is its shear-thinning behavior [10]. At an increasing shear rate, the sample spanning network collapses, starts flowing, and approaches the viscosity of the suspension without added liquid at high shear rates. After shearing the sample, it can rejuvenate and rebuild its sample spanning network [41]. In wet granular matter, such as sand castles, shearing of pendular bridges results in rupture of the bridge when a critical particle distance is reached. This behavior is dependent on the capillary bridge volume [42, 43]. In contrast, the capillary force F_c , described in Equation 1.2 for spherical particles, is independent of the bridge volume at small particle distances [44]:

$$F_c = \frac{2\pi r \gamma_{i/m} \cos\theta}{1 + 1.05\hat{s} + 2.5\hat{s}^2}, \text{ with } \hat{s} = s\sqrt{\frac{r}{V_l}} \quad (1.2)$$

where r is the radius of the particle, $\gamma_{i/m}$ is the interfacial tension between species i and m , θ is the contact angle, s the distance between spheres and V_l is the volume of the bridge. The attractive capillary force, i.e. bridge formation, is only re-established when the particles again come into contact, which makes this force hysteretic [44]. Natalia et al. observed comparable behavior microscopically in capillary suspensions [39]. At high shear rates, the bridges in the pendular state sample rupture and the viscosity decreases. However, when the shear rate was decreased, the viscosity and elastic attractive force increased while the sample was still under shear. This shows that there is a balance between viscous forces causing rupture of the bridges and regeneration of the elastic capillary force when flocs tumble, make contact with each other and once again are bridged by the secondary liquid. The capillary state behaves similarly. At high shear rates, the trapped liquid is ruptured and forms single smaller free droplets. These smaller droplets are distributed throughout the sample and possess a large interfacial energy due to the increased liquid-liquid interfacial area. At decreasing shear rate, the droplets act as scaffolding such that particles are “drawn” to the liquid-liquid interface in an effort to decrease the interfacial energy. This thereby arranged structure causes network formation [33, 39]. When sheared under confinement at low shear rates, the particles come into contact and form capillary liquid bridged, anisotropic clusters that predominantly align in the vorticity direction, leading to vorticity rolls.

The detailed microstructure of the pendular state capillary suspensions at rest was investigated by Bossler et al. [37]. By means of confocal microscopy and fractal dimension analysis, they showed that the particles in a sample spanning network form a combination of differently packed structures, as sketched in Figure 1.5. Individual particles with radius a , connected via capillary bridges, are arranged into flocs, as outlined with a dashed circle and labeled with their radius ξ . These clusters, which possess a higher fractal dimension, are connected to other clusters at the interfloc region shaded in gray. The interconnected flocs form a sparse backbone structure, described by a lower fractal dimension. While most particles are connected to each other through this sample-spanning network, only few particles form the network backbone capable of transmitting forces [37], as illustrated by the red line in Figure 1.5. Due to the nature of this obtained heterogeneous gel structure, its yield strength is determined by the weakest link, often the connection between the clusters. The shear modulus, on the other hand, is dependent on the floc dimensionality and relative strength of the intra- and inter-floc bonds.

As previously mentioned, the microstructure of a suspension greatly affects its strength and, therefore, macroscopic rheological behavior [30]. The non-linear relationship between the yield stress and the amount of added secondary liquid, shown in Figure 1.3 as well as in

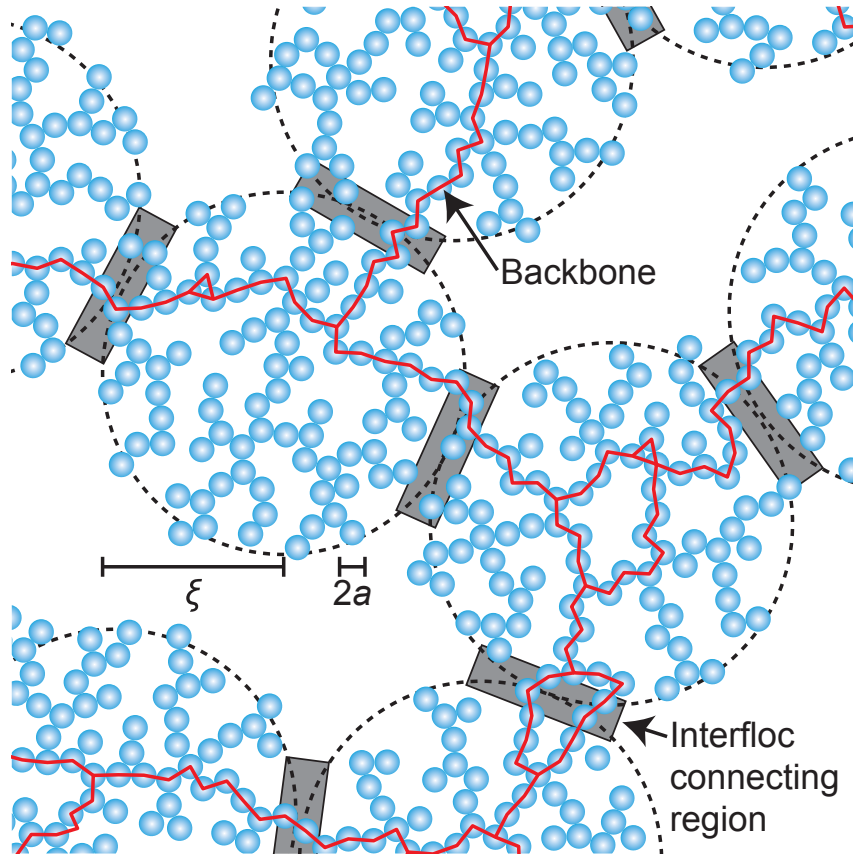


Figure 1.5: Sketch of a capillary suspension's microstructure in the pendular state. Denser clusters comprising particles bridged by the secondary liquid are connected with other clusters, forming a sparse backbone structure. This sample spanning network leads to a gel network with its weakest point being the interfloc connection shown in gray. Reprinted with permission from AIP Publishing [37].

several other publications, strongly indicates a complex interplay between microstructure, mixing conditions and yield stress [8–10, 34, 36–38, 45–52]. The fractal dimension approach used by Bossler et al. [37] showed a heterogeneous network structure consisting of a sparse backbone with connected clusters. However, a clear descriptive link between the sparse microstructure and the rheology remains insufficient. In an effort to better account for the structural variations, Bindgen et al. [53] further examined pendular state capillary suspensions (attractive particle network) by means of a mathematical network study based on graph theory. They introduced the clustering coefficient c in conjunction with the coordination number z .

$$c = \frac{2e}{z(z-1)} \quad (1.3)$$

This clustering coefficient accounts for the number of connections among the surrounding particles e , normalized by the number of bonds z between neighboring particles relative to a centered particle. For instance, a sphere surrounded by three spheres that are not in

contact with each other, has a coordination number of $z = 3$ but $e = 0$. When the same amount of surrounding spheres touch each other, they form a bond triangle where e equals two bonds. This results in the higher clustering coefficient of $c = 2/3$. That is, for $c \rightarrow 1$, a floc shows higher local clustering. Their results demonstrate that the coordination number and clustering coefficient can be correlated to changes in the storage and loss modulus when increasing the secondary fluid fraction. Such semi-local measures can also be applied to other materials with an inhomogeneous microstructure [53].

1.4 Stress characterization

During drying of suspensions with particle loadings below the gel-point (or glass-transition), the coating shrinks solely due to sedimentation and evaporation of the continuous fluid with a constant drying rate. However, the very instant a meniscus forms (floculated state), compressive forces arise (Equation 1.1) [54]. These forces then act on the particle network with the same degree [55]. Upon exceeding a threshold, the compressive yield stress P_y (below which the particle network is able to elastically store the arising stresses), the particles start yielding, which leads to an irreversible deformation of the microstructure [56]. Thus, P_y is a measure that can be used to characterize a coating's ability to withstand stresses during drying.

The compressive yield stress as a function of particle volume fraction (ϕ_{solid}) of hard particle suspensions can be determined by different techniques such as gravitational sedimentation, centrifugation, as well as pressure filtration and osmotic consolidation [55]. For example, the cake height at various speeds during centrifugation can be used to calculate the corresponding pressures. Another approach uses “destructive sectioning”, in which the resulting volume fraction gradient in the cake is determined at one speed [55]. In general, however, the determination of the compressive yield stress of a sample is significantly more cumbersome and time consuming than measuring the shear yield stress. Since compressive and shear yield stresses both describe a network's rigidity (inter-particle strength) against plastic deformation, it would be convenient to have a direct relationship between them [57]. Channell and Zukoski [56] found a linear relationship for alumina particles (AKP-15). Zhou et al. [57] compared shear and compressive yield stress in different particle systems as a function of volume fraction. They found that for alumina suspensions, the linear relationship breaks when the solid volume fraction exceeds $\phi_{\text{solid}} \approx 0.45$. The ratio of compressive to shear yield stress is then an increasing function of the particle load [57]. Nonetheless, the ever-present link between these measures allows for qualitative conclusions based on shear yield stress measurements.

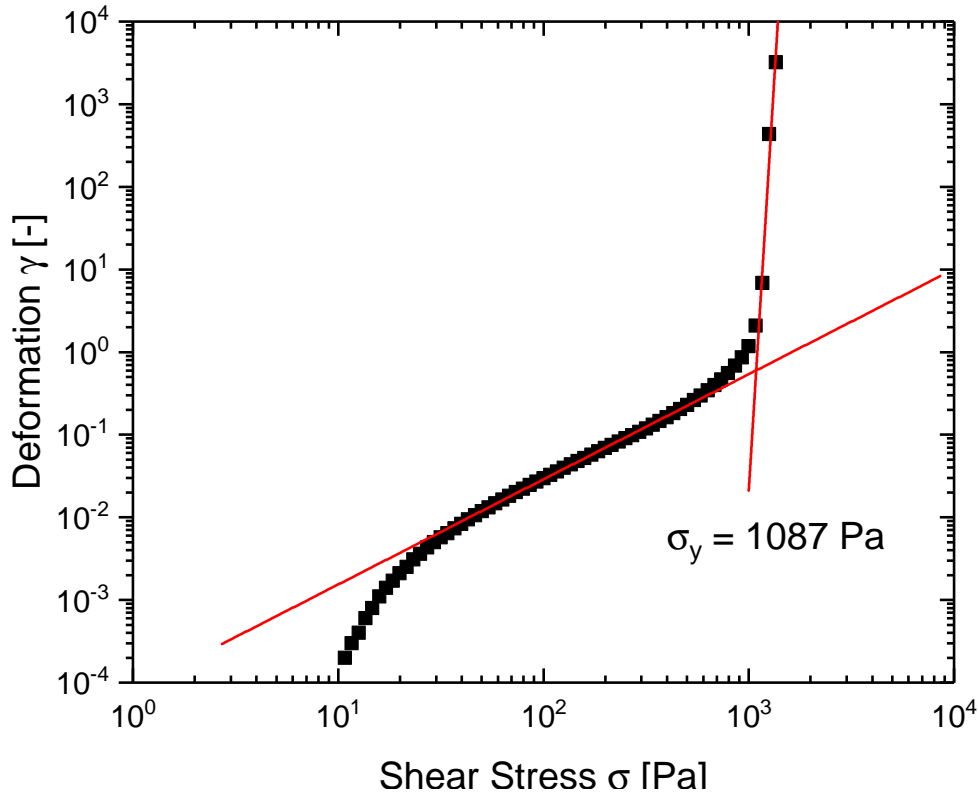


Figure 1.6: Exemplary shear stress vs. strain curve with added tangents. The apparent yield stress is obtained at the tangent intersection. Data represents the behavior of a capillary suspension formed with alumina particles at a solid volume fraction of $\phi_{\text{solid}} = 0.25$ suspended in 1-heptanol with an added water content of $\phi_{\text{H}_2\text{O}} = 0.031$ at 30 °C.

Shear yield stress measurements of suspensions are performed with a rheometer and present a straightforward and established characterization method. Suitable geometries for suspensions are plate-plate or vane and cup setups. While the former uses smaller sample sizes, the latter is more robust towards slip. After loading the sample into the cup and lowering the vane geometry, the sample is allowed to relax the stresses induced during loading. Afterwards, a logarithmic shear stress (σ) ramp is applied stepwise and the resulting strain γ (deformation) is measured. A typical result is the stress-strain plot as shown in [Figure 1.6](#). In this thesis, the tangent method was used to determine the yield stress. Upon increasing the stress, the strain also gradually increases ($\gamma \sim \sigma$) until a point where the sample starts yielding, which manifests as a rapid increase in deformation ($\gamma \sim \sigma^n, n > 1$). The intersection of the two tangents, shown in red in [Figure 1.6](#), is then recorded as the yield stress.

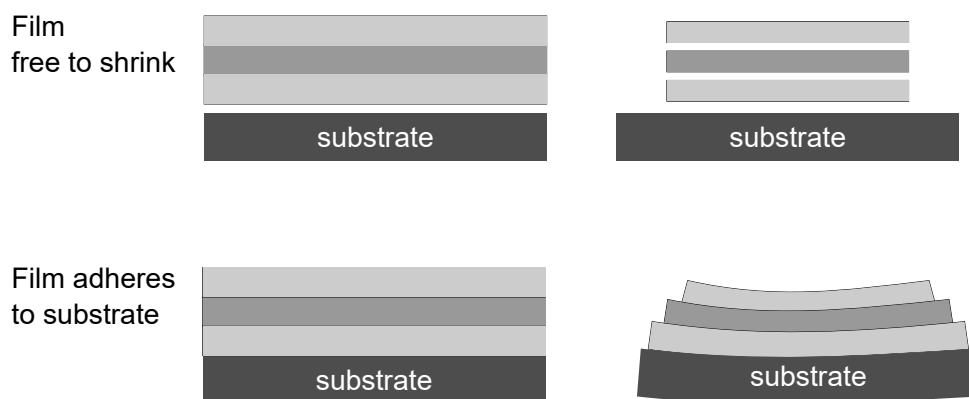


Figure 1.7: Comparison of freely shrinking hypothetical film layers (top row) versus a film adhering to a substrate (bottom row). The freely shrinking film does not exhibit any stress. On the other hand, when the connected film layers adhere to the substrate, stresses occur and the substrate bends [58, 59].

1.5 Film stress measurements

During drying of particulate films, the arising capillary pressure described in [section 1.1](#) exerts stress on the film network. If the coating is allowed to freely shrink, i.e. is unconstrained by adhering to a substrate, the shrunken film would be stress free, as sketched in [Figure 1.7](#) [58, 59]. However, in reality, the film adheres to the substrate and is, therefore, constrained from shrinking, which leads to a stress caused by the film that is exerted on the substrate. As a result, the substrate bends to a degree that depends on its rigidity and dimensions. This effect of substrate bending can be used to measure the stress in drying coatings by measuring the deflection from its initial position. Various methods have been developed, most of which determine the overall, averaged, stress in a film. A technique that is capable of measuring the spatial resolution of the stress occurrence, namely membrane bending, was presented by von der Ehe and Johannsmann [60]. While the measuring principal is also based on bending the membrane, a dotted pattern is added to the substrate. A change in local stress causes the dot pattern to distort, which is captured with a camera. This leads to a spatially resolved stress formation. However, while this technique overcomes the drawback of spatial stress resolution, it is lacking the ability to easily set the drying conditions. The beam bending, or cantilever deflection method, which is described in detail in [chapter 2](#), allows the drying conditions to be set as well as other measures of interest to be implemented. This includes the drying rate, for instance, which makes this technique the predominant method for stress measurement, despite the overall stress value [61].

1.6 Motivation and goal of this work

The mechanism of meniscus formation and resulting stresses, described in [section 1.1](#), can lead to damage of the dried coatings. In order to prevent these defects, the coatings are modified with additives. Rheological aids such as thickeners are added especially in ceramic formulation. Binders that “glue” the particles during later stages of drying are also added to take up stresses and prevent body fracture [62, 63]. Finally, surfactants are added to decrease the surface tension, resulting in lower capillary pressures, as can be seen from [Equation 1.1](#) [54, 64]. However, some products, such as ceramic green tapes or printed electronics, require the removal of these organic substances in order to sinter the particles or create necks to obtain a conductive percolating network. To do so, an intermediate annealing, or pyrolysis step is introduced. If the ideal conditions, such as sufficiently high temperature, are not met during this step, organic residues may remain in the film. Further, this step may induce large stresses that lead to fracture and render the body unusable [65, 66]. Wedin et al. [67] found that the addition of thickeners, such as carboxymethyl cellulose (CMC), significantly increased the peak stress of a coating during drying, and thus, its proneness to cracking.

An alternative method used to manipulate the rheological behavior of pastes and particulate coatings is available with the capillary suspension concept, as described in [section 1.3](#). The most prominent difference between these suspensions compared to conventional formulations is the absence of polymeric additives. The rheological properties can be tuned by addition of an additional immiscible liquid that eventually evaporates during drying, leaving a green body free of undesired polymeric residues and thus saving subsequent processing steps. In addition to these advantages, we found capillary suspensions can dry with fewer or even absent defects [8]. The reasons for the crack reduction were hypothesized to stem from the capillary forces caused by the trapped liquid. The induced sample spanning network was hypothesized to counter the forces occurring during drying, as sketched in [Figure 1.8](#). The formed menisci at the coating’s air-liquid interface induces the surface force $F_{\gamma_{lv}}$ (illustrated with black arrows). In a capillary suspension, this force is distributed and countered by the network structure and individual capillary forces F_c between particles, drawn in gray. However, a more detailed investigation of the drying behavior of pendular state capillary suspensions is needed to understand the underlying mechanisms. In this dissertation, I shed some light on the different mechanistics of capillary suspension drying and their implications on stress formation. The centerpiece for developing a better understanding of the drying

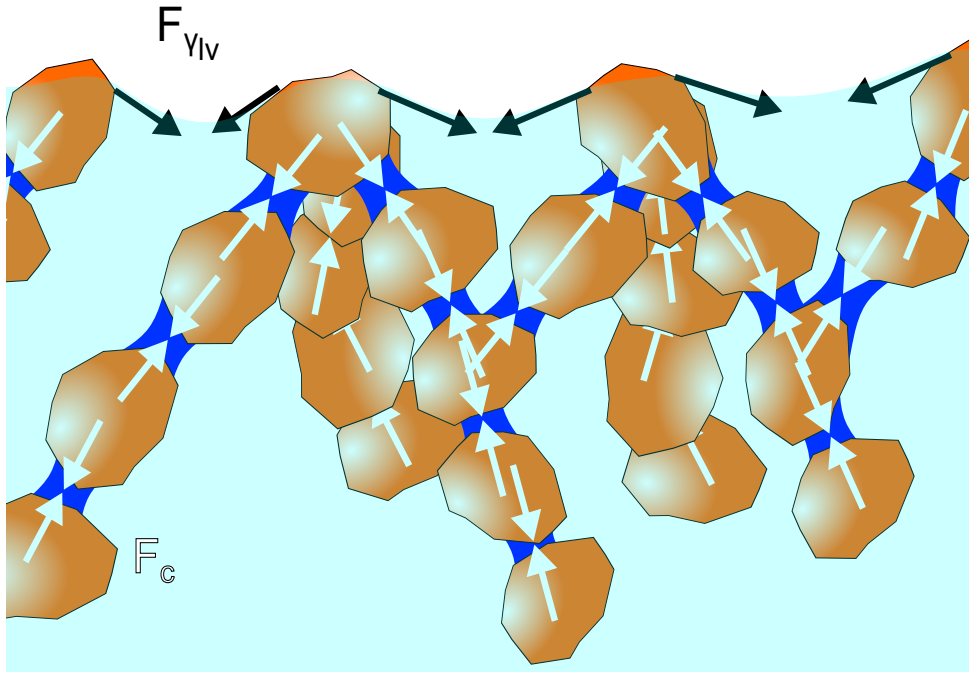


Figure 1.8: Schematic illustrating occurring forces in a capillary suspension during drying. The surface force $F_{\gamma_{lv}}$ drawn in black caused by meniscus formation. We hypothesize that this force is countered by the sample spanning capillary bridge forces F_c drawn with white arrows.

behavior is the design and optimization of a stress measurement apparatus that allows the investigation of the stress evolution at different drying conditions and formulations.

1.7 Manuscript outline

In order to enable an investigation of the stress development during drying, I designed and built the measurement setup that is presented in [chapter 2](#). The novel design is based on the cantilever deflection method, which allows the film drying rate to be reliably linked with average stress build up. The suspended weighing mechanism and unique cantilever attachment method enables the investigation of different drying conditions, such as elevated humidity and temperature of various kinds of coatings, ranging from polymeric films to ceramic pastes. In contrast to existing setups, we are able to obtain the two measures from a single film *in situ*. Thus, faulty conclusions caused by inhomogeneities in drying conditions within the chamber, which can significantly impact the drying behavior of the film, can be excluded.

The designed apparatus described in [chapter 2](#) is employed in [chapter 3](#) to investigate drying effects on capillary suspensions. Understanding the microstructural interfacial processes are key to obtain functioning coatings and energy efficient drying processes. Multiple techniques are combined to relate measured drying stresses to changes in the film

weight and the visual appearance of coatings. We compare the behavior of formulations prepared from a regular suspension to a capillary suspension in the environmentally controlled drying chamber. We find that the three-phase attractive particle network dries fundamentally differently compared to the normal suspension. We measure the film height profile during drying *ex situ* and use dye-tracer to further elucidate fluid flow inside the coating during drying. The insights gained experimentally are used to propose a mechanistic capillary flow scheme explaining the macroscopically observed drying features of capillary suspensions.

In [chapter 4](#), we again use the measurement setup developed in [chapter 2](#). For the first time, we are able to directly obtain and relate the stress development and weight loss of the same coating at various temperatures and relative humidity. We compare the peak stress with the obtained dry film porosity, calculated from the weight measurements, for suspensions at different solid content and corresponding strength in the capillary suspension system. Furthermore, we investigated the effect on peak stress when the capillary suspension's secondary liquid possesses a higher boiling point than the bulk fluid. In order to determine if a capillary suspension's capillary bridges (formed with a higher vapor pressure liquid) persist during drying, we used a thermogravimetric analysis coupled with mass spectrometry. Linking the experimental results with the mechanistic drying scheme and three-phase flow considerations obtained from the work in [chapter 3](#) allows us to better understand the drying behavior of capillary suspensions and provides new possibilities for optimized coating formulations.

Over the course of the research for this thesis, we observed time effects in the elastic behavior of the capillary suspension formulation upon repeated high shear mixing and storage. Moreover, the results during drying in humid air shown in [chapter 4](#) strongly suggest an interaction caused by the water from humid air with the regular suspension. Literature data revealed a partial solubility of the secondary liquid (water) in the bulk fluid (1-heptanol) in the order of a few volume percent, which is also the amount used to form capillary suspension in the presence of adequate particles. In [chapter 5](#), we investigate a new formulation route for capillary suspensions explicitly using this solubility. While capillary suspensions are generally formed by the addition of a small amount of secondary liquid to a pre-dispersed regular suspension, we present a formulation route starting from the dissolved secondary fluid. The phase separation is solely induced by the particles and the three-phase equilibrium. We investigate the material strength with deliberately dissolved secondary fluid as well as through storage in an enclosed humid chamber. The yield stress of a homologous series of 1-alkanols as bulk liquid with increasing water solubility is investigated. Furthermore, we explore the feasibility of this concept with

various particle types: irregularly shaped, sub-micron alumina particles; micron-sized spherical silica glass beads; and titanium dioxide with nanometer-sized primary particles. This research reveals the important interplay between humid air and oil-based suspensions, and how it can play an advantageous role during drying of suspensions or cause problems when storing oil-based suspensions in a humid environment. These key findings lead to a holistic understanding of capillary suspension drying and the endeavour to obtain defect free particulate films.

Finally, the work and results of this dissertation are briefly summarized in [chapter 6](#). An outlook with proposed future work is also included. This outlook addresses improvements and extensions of the stress measurement setup as well as improvements to the material system.

2 Apparatus for simultaneous stress and weight measurement during film drying in an environmentally controlled chamber

Full title: Apparatus for simultaneous stress and weight measurement during film drying in an environmentally controlled chamber [68].

Authors: Steffen B. Fischer, Erin Koos

Status: published and selected as “Editor’s pick”

Bibliographic data: *Rev. Sci. Instrum.* 91(12):123904, 2020.

doi: <https://doi.org/10.1063/5.0030739>

Reproduced from Rev. Sci. Instrum. 91, 12 (2020), with the permission of AIP Publishing. Authors do not need permission from AIP Publishing to reuse your own AIP Publishing article in your thesis or dissertation.

<https://publishing.aip.org/resources/researchers/rights-and-permissions/permissions/>

The article has been adapted in this thesis to reflect the numbering of references and citations in accordance with the manuscript.

2.1 Abstract

The drying behavior of coatings is essential for the development of formulations in order to obtain reliable and defect free finishes. There are two major measures of interest: the development of the stress responsible for cracking and the drying rate that gives insight into the morphological structure. The cantilever deflection method is the predominant way of determining stresses under defined drying conditions such as temperature and humidity. However, both measures of interest are currently obtained using two different coatings when dried in a chamber, or a single coating with simultaneous measurements that can only be dried under ambient conditions. In this paper, we present an apparatus design based on the cantilever deflection method that allows simultaneous measurement of the stress and drying rate in an environmentally controlled chamber.

2.2 Introduction

Modern coatings are found in a vast variety of products and markets. Whether it be in the automotive industry as varnishes, protective paints for wood, marine anti-fouling coatings or printing of conductive pastes or batteries [1, 2, 4–6, 69]. In the strive to create environmentally friendly waterborne formulations, absent of volatile organic compounds, the suspension formulation becomes even more critical as they are prone to defects. Drying of these coatings can lead to cracking or other defects caused by stress formation within the coating [70–72]. The drying process can be divided in different stages. At first, the suspension dries and shrinks with the characteristics of the bulk fluid at a constant rate with negligible stress increase [15]. Second, as the particles have compacted, the fluid recedes into the coating thus forming menisci. Chiu et al. were the first to experimentally show that stresses that occur during drying are caused by the capillary tension induced menisci [54]. This understanding helps modifying coating formulations to reduce drying defects.

There are different stress measurement techniques available with varying levels of additional measure integration. These include setting the drying conditions, measuring the drying rate, and visually observing the drying by means of a camera, among others. The drawback of some of the employed techniques is that measurement results stem from different coatings. Drawing conclusions from these examinations is only valid if the obtained films are nearly identical, which is the case for easily spreadable and coatable materials such as low viscosity polymer blends. Application of thick, elastic pastes, on the other hand, often leads to local variations in thickness that greatly affect drying rates and stress build up, making a comparison between different films suspect. In this work, we present an apparatus design that allows us to simultaneously record the stress and drying rate of the same coating at specified drying conditions. The next section briefly describes different stress measurement techniques before introducing our new apparatus design.

2.3 Stress measurement techniques

Stress measurement techniques have been evolving since the early work on the tension of metallic films by Stoney in 1909 [73]. Since then, most techniques developed have been based on the deflection of a substrate. An optical technique was presented by Raju and co-workers [74]. The measuring principle is based on a linear change in birefringence caused by a stress-dependent increase from optically isotropic to optically anisotropic properties of the fixed substrate. They claim to obtain a more accurate stress value due

to the absence of a stress relaxing deflection of the substrate. A direct comparison of their set-up with bending techniques were difficult due to a lack of adjustable drying conditions. An *in situ* drying rate was not determined.

Other techniques correlate a substrate's deflection evoked by shrinkage of an adhering coating. The result is an average stress of the coating. Details are described later in [subsection 2.4.6](#). In contrast, von der Ehe and Johannsmann [60] developed the membrane technique that allows spatial resolution of the stresses. The sample dries on a semitransparent membrane that mirrors an array of dots placed underneath. A camera detects distortions of the image, which are related to the local vertical deflection and subsequently used to compute the spatial stress [75]. Their technique only measures stresses, other measures of interest have to be determined separately. Interferometry makes use of generated Newton's rings of a monochromatic light source to determine the curvature of a material [54]. A sample is coated on the substrate and placed on an optical flat (glass). As it deflects, a thin air film is generated. Part of the monochromatic light ray coming from the bottom is reflected (ray 1) at the glass-air interface. The other part of the incident beam (ray 2) refracts and is subsequently reflected at the interface of the air film and substrate accompanied by a phase shift. Interference of ray 1 and ray 2 lead to constructive and destructive interference patterns with a distance of half the light's wavelength known as Newton's rings allowing the determination of the deflection at a given length. Suspending the optically flat substrate from a scale allows simultaneous measurement of weight loss and shrinkage as carried out by Chiu and Cima [54] and Guo and Lewis [55]. Bauer and co-workers [64] extended this method by using a transparent substrate, which allows the film saturation and drying front to be tracked. Drying conditions were ambient and not adjustable.

Drying stresses often anisotropically propagate in stress fronts, which are difficult to track. However, the integrated stress can be determined by the predominant stress measurement technique: the cantilever deflection method [61]. One end of the beam is clamped while the other end is free to bend as sketched in [Figure 2.1](#). With this technique, however, it is only possible to measure an overall stress. This includes stresses caused by other effects such as an uneven coating or lateral drying caused by the narrow cantilever [76–78]. The adhering and shrinking coating exerts stress on the substrate causing it to deflect. A photo diode (position sensing detector (PSD)) records the distance a reflected laser beam has traveled due to the curvature of the cantilever. This technique facilitates stress measurement at specified drying conditions by placing the clamped cantilever in an environmentally controlled chamber.

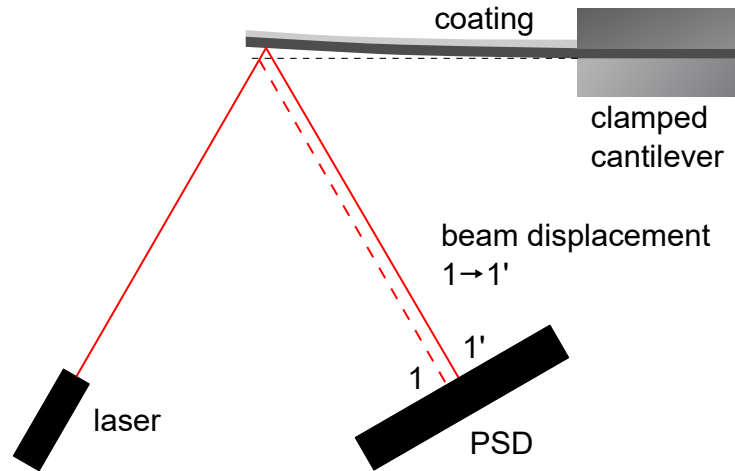


Figure 2.1: Sketch of the cantilever deflection technique. The laser beam is reflected at the bottom of the substrate and recorded by the position sensing detector (PSD). Upon shrinkage induced bending of the cantilever, the laser travels from point 1 to 1' on the PSD.

Since the cantilever deflection can be small (a few micrometers), rapid and precise placement inside a drying chamber would be required for simultaneous measurements. To date, this has not been possible. Instead, most researchers coat a second cantilever and insert it in the same chamber in order to obtain the drying rate under the specified conditions. This second cantilever is then placed on a suspended balance pan connected to a weight scale outside the chamber [21, 67, 76, 78–82]. However, this assumes identical coatings as well as spatially identical drying conditions inside the chamber that are challenging to obtain. So far, obtaining a true simultaneous measurement of stress and drying rate of the same coating was associated with trade-offs Fu et al. [83]. obtained the simultaneous measurement by placing the clamped cantilever directly on a weight scale with the drawback of drying at ambient conditions. Kiennemann and colleagues (2005) [84] obtained the drying rate at different temperatures by placing the sample on a heated plate sitting on a balance but without information about the occurring stresses.

Our design of the cantilever deflection set-up allows the simultaneous measurement of stress development and drying rate of the same coating in a temperature and humidity controlled environment. Such a chamber enables the development of ideal drying conditions. In the following section, we will describe the design and peripheral devices in detail.

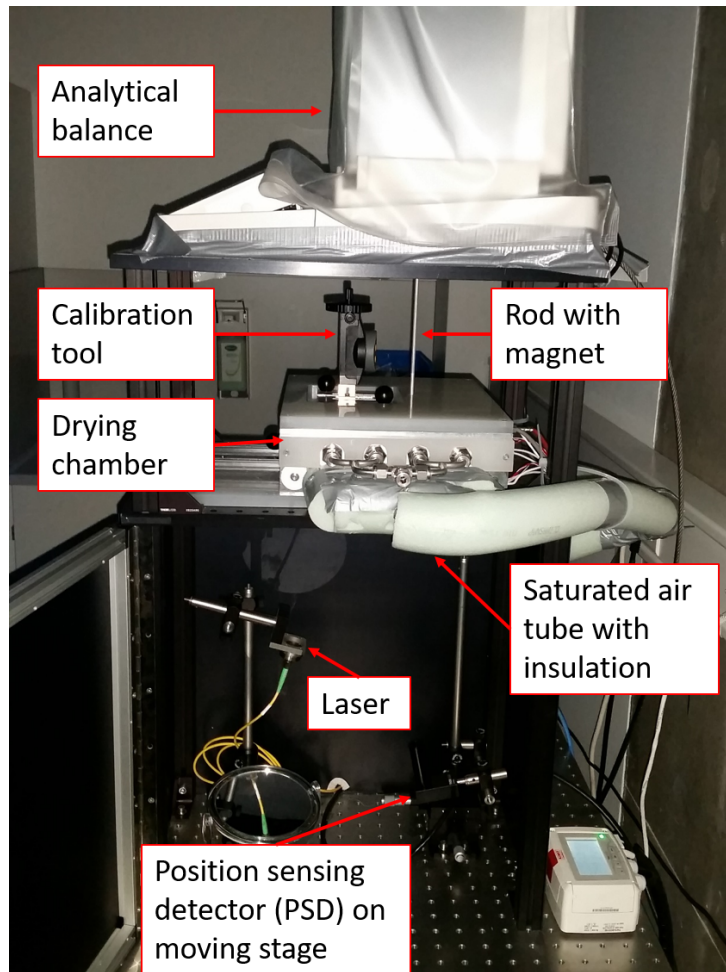


Figure 2.2: Photograph of the stress measurement apparatus on top of an optical table. The cantilever fixture is inside the chamber, suspended on a rod from the analytical balance. The calibration tool is removed before a stress measurement.

2.4 Design of the stress measurement setup

2.4.1 Apparatus setup

The stress measurement set-up is built on a vibration reducing, passively isolated optical table topped with a breadboard (Nexus, Thorlabs, USA). The essential parts of the apparatus are built on top of the breadboard, as shown in [Figure 2.2](#), with supporting parts beneath. An aluminum frame is used to secure two horizontal plates (approximately) 700 mm and 450 mm above the breadboard. An analytical balance (Sartorius Cubis MSA 224S, Sartorius Lab Instruments GmbH & Co.KG, Göttingen, Germany) is placed on top of the upper plate, which is machined with a 50x50 mm opening. Through that hole, a rod reaching into the drying chamber is connected with the suspension weighing mechanism of the scale. The attachment mechanism is described in [subsection 2.4.4](#). The lower plate is

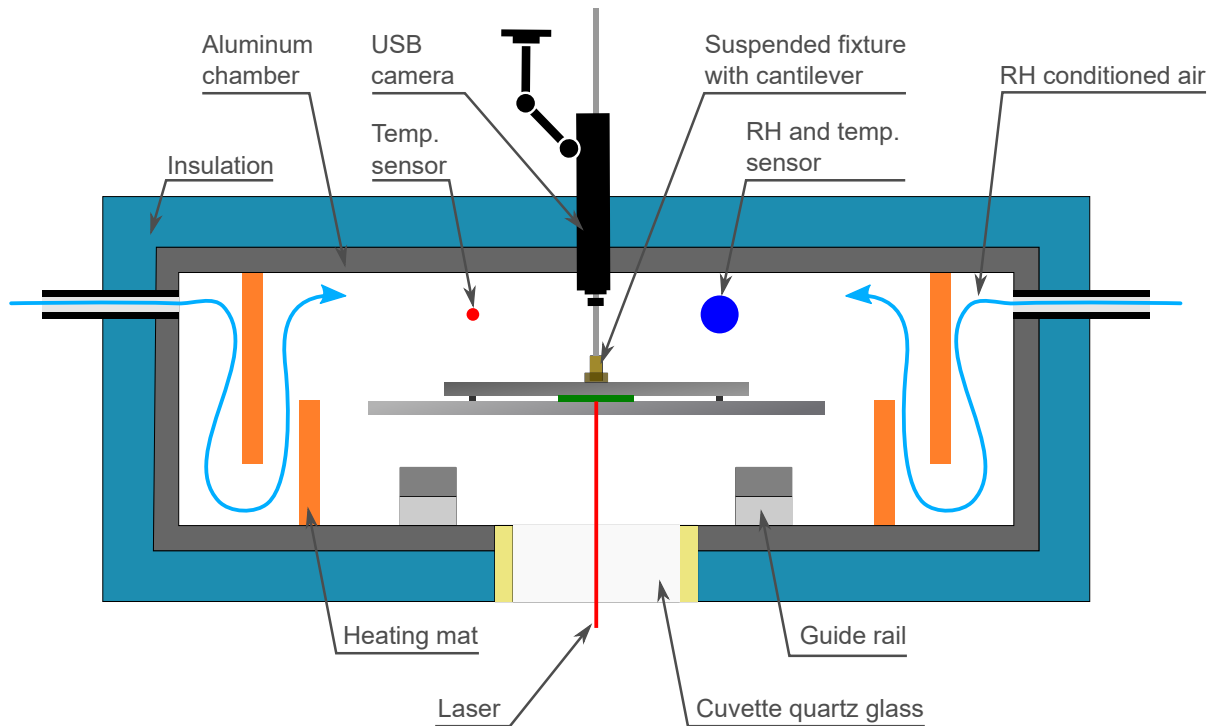


Figure 2.3: Front view of the aluminum drying chamber (dark grey) covered with polycarbonate insulation sheets (blue). The cantilever with fixture suspended from a rod is placed centrally. A humidity sensor registers the water content of the air inlet on either side of the chamber. Temperature sensors track and control the heating mats (orange).

machined with a hole of 50 mm. Mounted on top is the insulated drying chamber equipped with air feed tubes on the sides and described in more detail in [subsection 2.4.2](#). An opening in the roof of the chamber allows the insertion of the calibration tool and is replaced by a lid during measurement and an optional universal serial bus (USB)-camera. On top of the large breadboard (bottom of [Figure 2.2](#)) a laser (TLS001, 635nm, Thorlabs, USA) is mounted on the left and the lateral position sensing detector (PDP90A, Thorlabs, USA) on the right. Both are attached to posts to adjust their height and in-plane adjustments are made via moving stages equipped with micrometer screws. For safety precautions as well as exclusion of other light sources, the laser and PSD are enclosed by a door and anodized aluminum sheets. The set-up is leveled by manually changing the pressure in the vibration isolators.

2.4.2 Drying chamber

A schematic showing the interior of the drying chamber is shown in [Figure 2.3](#). Before air enters through the tubes on either side of the chamber, it can be conditioned to the desired humidity. This is accomplished using the manual air control unit shown in [Figure 2.4](#). At first, dry compressed air passes the pressure regulator and is split into two

flows with individually adjustable volumetric flow rate as depicted in [Figure 2.4a](#). The pressure regulator is used to protect the flowmeter from overpressure from the centrally provided pressurized air. Each flowmeter has a range of 0-10 l/min. One of the air streams flows through a bubbler placed on a heating plate as photographed in [Figure 2.4b](#). The bubbler can be heated via a water bath to raise the absolute air saturation as needed. This is necessary when the established absolute water saturation of air is insufficient at the obtained wet bulb temperature. The water saturated air stream and dry air stream are then mixed and enter the drying chamber while passing the vertically arranged heating elements (orange in [Figure 2.3](#)). An insulation layer (blue) around the aluminum chamber prevents excessive heat loss. The sheets are made of polycarbonate with a thickness of 15 mm and can resist a constant temperature of 120 °C. The drying temperature is regulated with a proportional integral differential (PID) controller with the sensor (not shown) centered in longitudinal direction and approximately 10 mm above the cantilever. The silicon heating mats (HORST GmbH, Lorsch, Germany) are protected from overheating by means of a safety shut-off if a specified temperature is exceeded. Their nominal temperature is 200 °C but the safety shut off was set to 170 °C. The PID settings have to be chosen accordingly. With a step wise temperature increase, uniform chamber temperatures up to 90 °C can be reached. The humidity, registered by the relative humidity (RH) sensor (dark blue circle), can be manually adjusted by means of changing the flow rates of saturated and dry air streams on the flowmeters. Due to poor insulation of the humid air tubing and, thus, water condensation inside the tube, the attainable relative humidity inside the chamber at 40 °C is limited to 50%. Care has to be taken with thermal bridges at the air inlet. Condensed water may drain and damage the equipment. An additional temperature sensor (red circle) allows temperature gradients inside the chamber to be measured. In the middle of the chamber, the suspended fixture with the clamped cantilever is connected to the analytical balance. In order to further prevent heat losses as well as to maintain the specified drying conditions, the 50 mm hole through which the laser (red line) passes is closed with a 1.5 mm thick cuvette quartz glass (Hellma GmbH, Germany).

2.4.3 Coating procedure

A prepared sample is coated onto the cantilever outside the chamber. For that, we machined a steel slab with a recess for the cantilever as well as the fixture as depicted in [Figure 2.5a](#). To ensure an equal height for the coating support and the fixture, their surfaces were sanded together. Rails were added such that the coating blade only moved along one axis. Below the cantilever we added a support topped with a weak magnetic strip as shown in [Figure 2.5b](#). This method maintains a constant contact of the cantilever

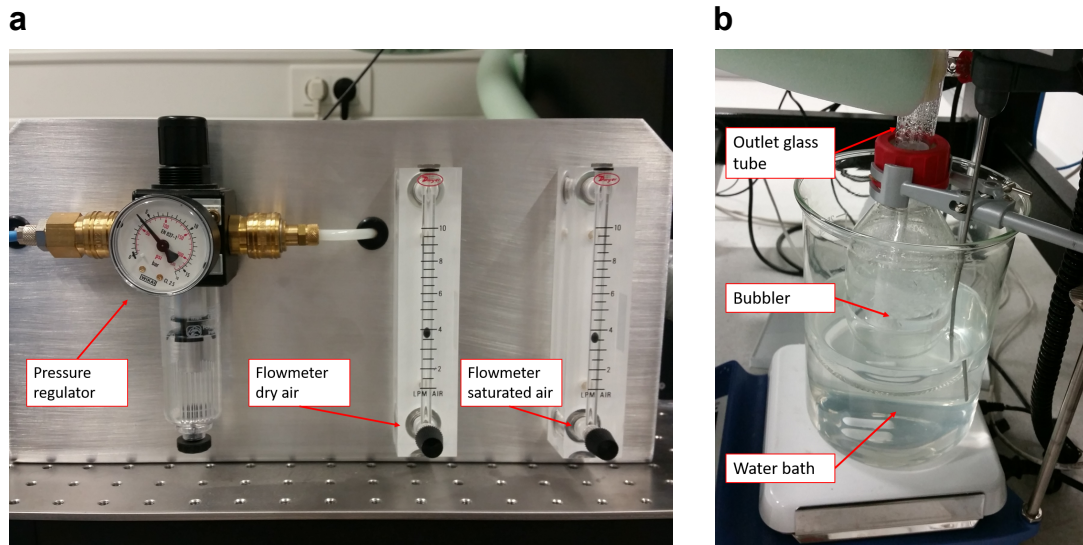


Figure 2.4: (a) Manual air control unit. The pressure regulator limits the compressed air pressure. Airflow is split and passes through two flowmeters. One stream is directed through a heatable bubbler to obtain water saturated air (b). Both streams are mixed and flow into the chamber.

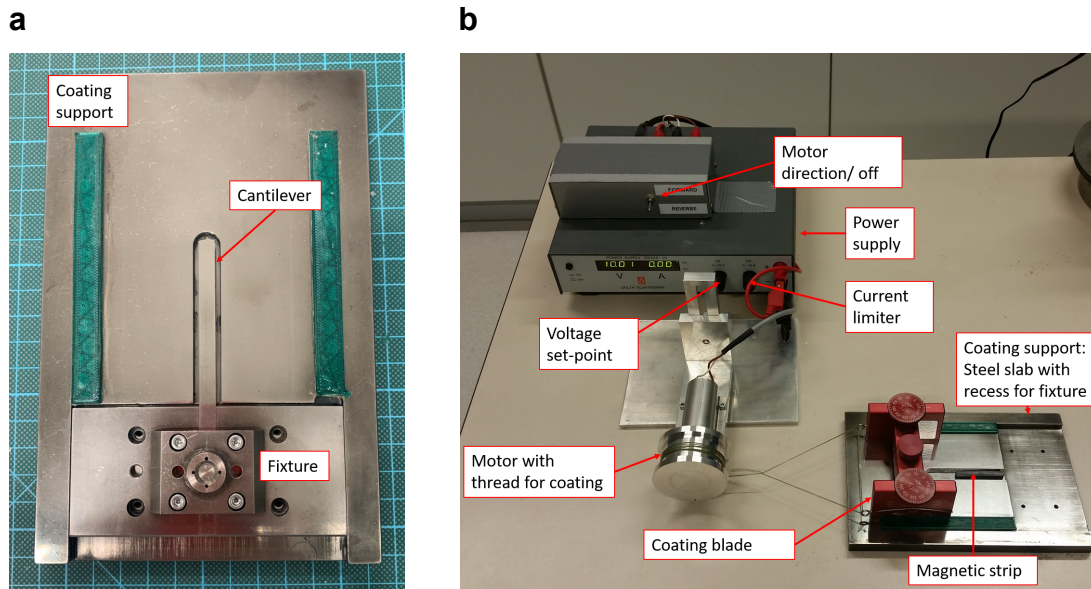


Figure 2.5: (a) Coating support machined from a steel slab with recess for the fixture and cantilever (the grid is 10 mm). (b) Power supply for adjusting the coating speed through voltage. Turning the switch starts dragging the coating blade. Image in (a) is reproduced from [85] with permission from John Wiley & Sons, Inc.

between coating procedures and aids in attaining repeatable film thickness. The coating blade (ZUA 2000, Zehntner GmbH, Sissach, Switzerland) with the desired gap height is dragged by a string along the cantilever. The coating speed is adjusted by means of supplying a voltage (up to 12 V) to a small motor, such that a coating speed of up to 0.29 m/s can be achieved. The speed can be further increased by mounting a larger reel than

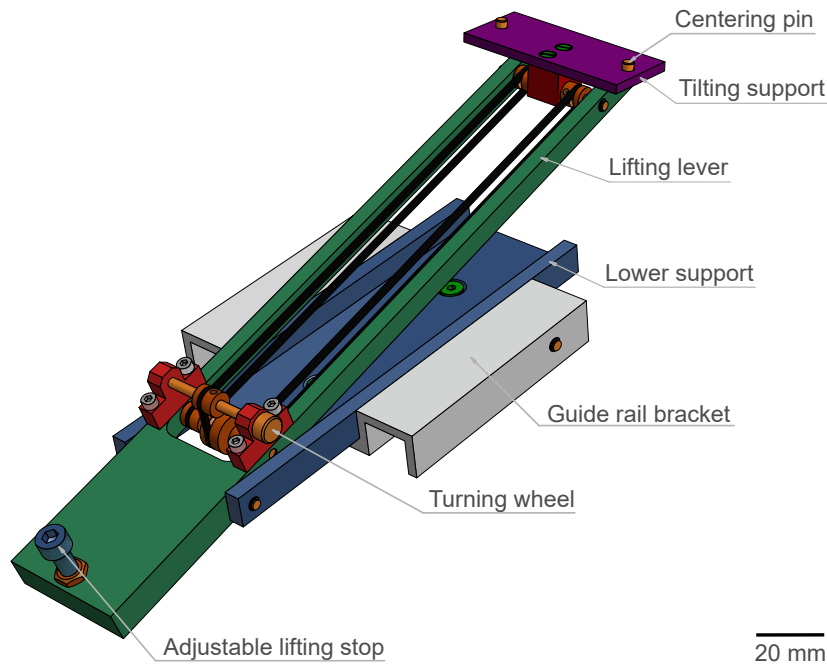


Figure 2.6: Tool for lifting the cantilever fixture at a precise position and orientation in order to connect to the suspended weighing mechanism. The lifting lever (green) lifts the cantilever above the lower support (blue) and the tilting support controls the angle of the fixture.

the current one, which measures 47.74 mm in diameter. Afterwards, the fixture is inserted in the chamber as described in the next section.

2.4.4 Inserting and attaching procedure

After the cantilever has been coated, the fixture is quickly inserted into the drying chamber. The simultaneous stress and suspended weight measurement poses several challenges. First, the space to access the chamber is very limited. Large openings as well as a long insertion period would significantly prolong the time to establish equilibrium conditions upon closing the door. Second, the position and orientation of the cantilever needs to be as constant as possible between measurements to increase repeatability of the measurements. The insertion tool, as well as the attachment mechanism used to enable weight tracking have to be designed such that the fixture is lifted and attached with the correct orientation. The three relevant degrees of freedom are roll, pitch, and yaw. The design of our developed tool is sketched in [Figure 2.6](#). The guide rail bracket (gray) is placed on the rails mounted in the chamber and allow linear movement of the tool into and out of the chamber. A lifting lever (green) lifts the fixture against the lower support (blue). The tilting support (purple) is connected to the accessible turning wheel outside the chamber via the belt drive principle. Fitted centering pins attached to the tilting support maintains the yaw with

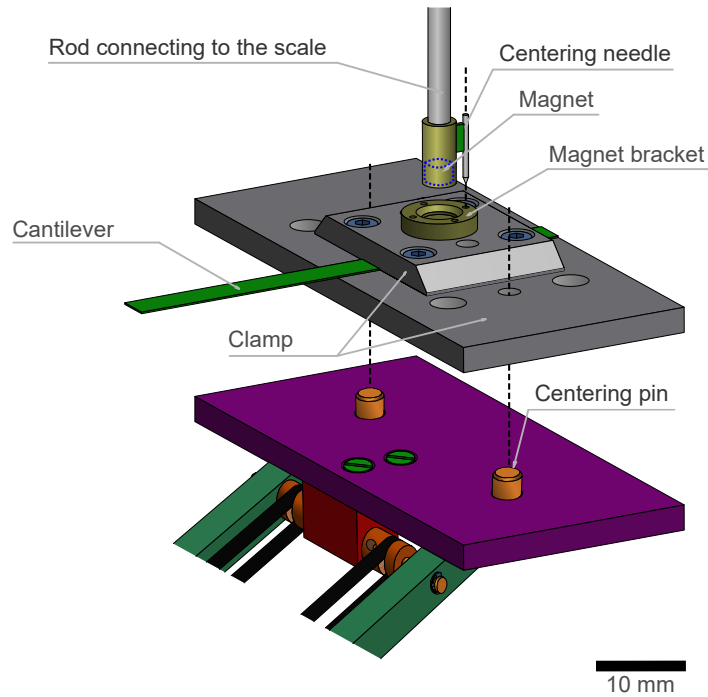


Figure 2.7: Attaching mechanism with lifting tool. The centering pins and needle ensure repeatable orientation of the cantilever. A magnet connects the cantilever clamp with the rod, which in turn connects to the suspension weighing mechanism of the analytical balance.

good precision during lifting and insertion. The interplay with the fixture and attaching mechanism is depicted in [Figure 2.7](#).

The attaching mechanism is equipped with a neodymium magnet strong enough to hold the fixture with the clamped cantilever, preventing roll and pitch, but weak enough that the fixture can be later released without damaging the film. Furthermore, the magnet has an attached centering needle that ensures minimum yaw and correct x , y , and z positioning between each measurement. The needle neatly fits in a small hole drilled in the magnet bracket, which in turn is mounted on the cantilever fixture. The entire insertion and attaching mechanism can be described as follows. After placing the coated fixture on the lifting tool and opening the chamber door, the tool is placed on the guide rails and pushed inside the chamber until it stops at a defined distance. The fixture is lifted until it is stopped and is maintained at the elevated position. At this point, the tilting support and fixture is tilted in forward position, and aligned so that the centering needle penetrates the hole in the magnet bracket. Afterwards, the tool is retracted from the chamber while turning the wheel, which brings the cantilever into a horizontal position. At a nearly horizontal position, the magnet lifts the fixture off, after which the tool is lowered, fully retracted from the chamber, and the door closed. With some practice, this procedure takes less than 15 seconds and ensures an accurate and repeatable positioning of the cantilever.

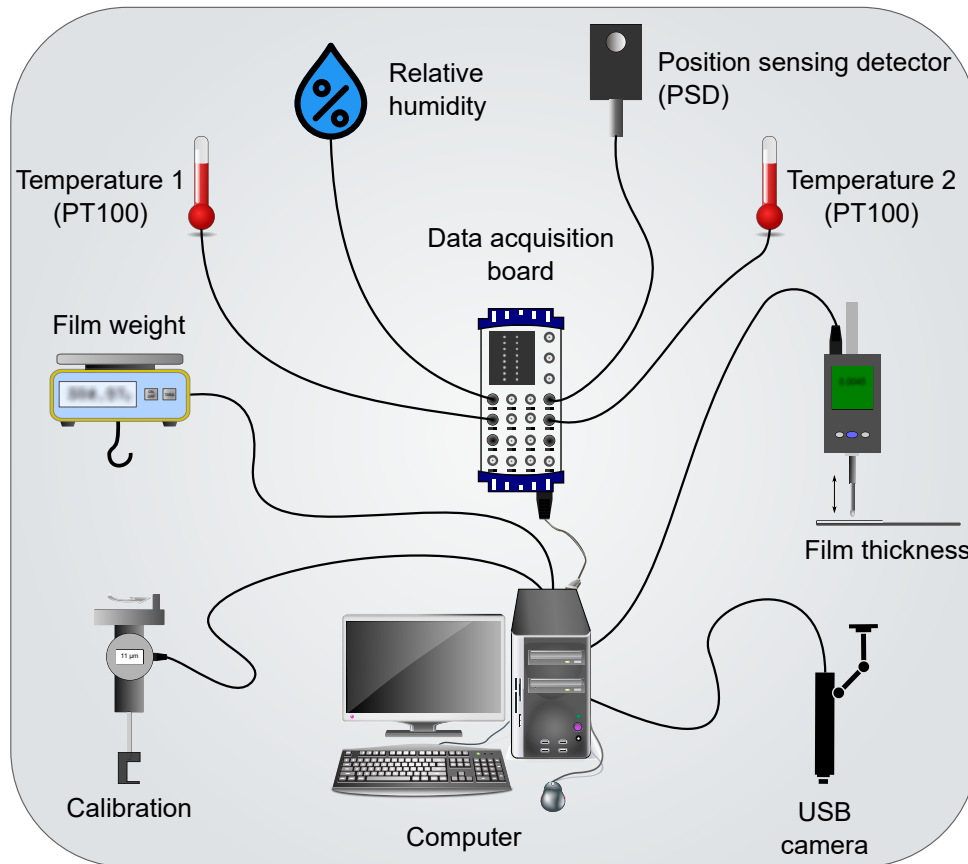


Figure 2.8: Digitally integrated and acquired data. Measures include chamber sensors as well as pre-processing (calibration) and post processing (film thickness). Data is received via DAQ board or direct USB to the computer. Data is recorded with LabView.

Given that the PSD, the suspension weighing mechanism with needle and the fixture with cantilever are properly aligned, there should only be little variation in the PSD's x-position. Otherwise the alignment of the individual parts has to be checked. Another source of error could be an uneven coating leading to a change in the roll direction and thus a change in the laser's x-position on the detector.

2.4.5 Data acquisition

The aim of the data acquisition (DAQ) is a fully integrated system to prevent transcription errors in further data processing. A sketch of the devices used is shown in Figure 2.8. A DAQ board (NI USB-6218, National Instruments, USA) collects the signals from the temperature transducers, the relative humidity sensor as well as three voltage signals from the PSD corresponding to the x-position, y-position, and the sum. The film weight is obtained via a universal serial bus (USB) connection with a Sartorius query protocol that upon query sends the numerical value. All signals are processed and displayed in LabView during the measurement. The sampling rate can be set to at least 500 ms.

After each experiment, the film thickness obtained from the stylus micrometer indicator is requested through a [USB](#) input tool (Digimatic [USB](#), Mitutoyo, Japan) and appended to the measurement data with LabView in order to obtain a single file containing all necessary information. Further data processing such as stress calculation can be done in any suitable program. Similarly, the calibration tool is connected via [USB](#) and a desired amount of measurement points per deflection can be recorded.

2.4.6 Calibration

Calibration of the set-up is an essential part for obtaining the stresses during drying. The beam bending theory is based on Stoney's work for uniaxial film stress [73]. While the length of the cantilever is generally much longer than wide, the cantilever covering coating is much thinner than the wide. Therefore, the stress contribution in width cannot be neglected, leading to a biaxial in-plane stress [86]. Later, Corcoran developed a correlation that relates the deflection/curvature of a beam or plate with the stress in a coating causing that deflection [87]. The adequate equation is applied by all techniques determining stresses through curvature of a substrate. For the cantilever deflection d , the stress σ is given by

$$\sigma = \frac{d \cdot E_s t_s^3}{3t_c L^2 \cdot (t_s + t_c)(1 - \nu_s)} + \frac{d \cdot E_c (t_s + t_c)}{L^2 \cdot (1 - \nu_c)} \quad (2.1)$$

where subscripts s and c represent substrate and coating, respectively. The substrate currently used in our design is a steel cantilever with thickness $t_s = 0.196$ mm, the Young's modulus $E_s = 210$ GPa, Poisson's ratio $\nu_s = 0.3$, and the cantilever's free length $L = 40$ mm.

A drawback preventing the straightforward application of [Equation 2.1](#) is its second term. It contains the coating's Young's modulus E_c at the time of measurement. As it is usually challenging to obtain, one tries to have an experimental design that allows dropping the second term. The temporal coating thickness t_c can be obtained through laser thickness measurements. However, in our current design we used a stylus micrometer indicator (ID-H530, Mitutoyo, Japan) with a precision of ± 1.5 μm and measured the dry film thickness. This is a good approximation since significant drying stresses predominantly arise at the compacted state. In order to drop the second term $E_s \gg E_c$ and $t_s \gg t_c$ needs to apply [87]. Using a steel cantilever, the first approximation applies for most coatings (particle coatings for instance [84, 88, 89]). In our case, the introduced error is $\sigma_c < 10\%$ [83, 87], for a coating thickness $t_c < 100$ μm .

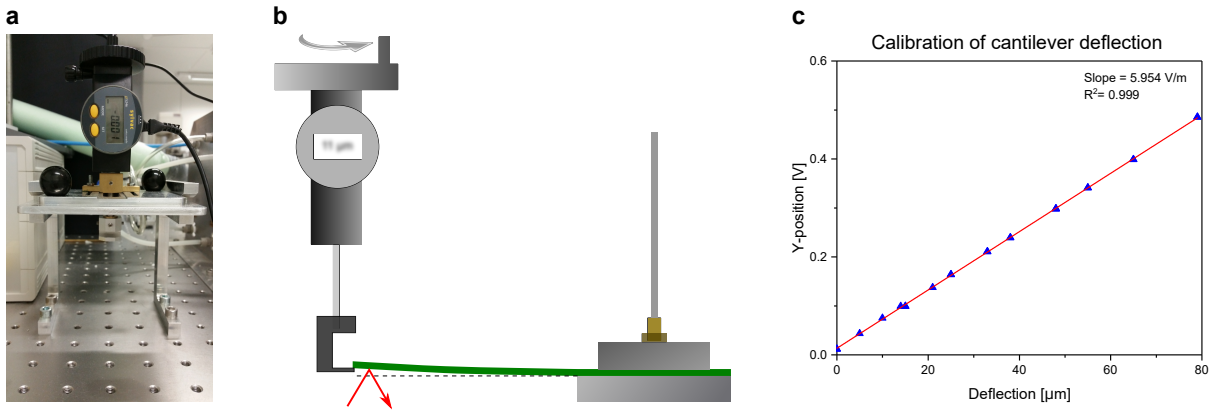


Figure 2.9: (a) Micrometer head with non-rotating spindle and U-shaped tool. (b) Sketch showing the deliberate deflection of the cantilever by a known distance causing the laser beam to move on the PSD. (c) Graph of the PSD voltage response upon cantilever deflection. The slope of the regression line allows to determine the cantilever deflection at a given voltage.

Generally speaking, Corcoran’s equation is only valid with the following assumptions [59, 87]:

- ideal adhesion between coating and cantilever;
- isotropic elastic properties of the coating and substrate;
- no plastic deformation of the coating or substrate;
- uniform biaxial stress in the coating;
- and a small cantilever deflection.

By ignoring the second term of Equation 2.1, the deflection is the only unknown to determine the drying stress. This is achieved by deliberately deflecting the cantilever a known distance with a micrometer head (Sylvac SA, Switzerland, Figure 2.9a). The U-shaped tool is attached to the non-rotating spindle and only touches the cantilever at the very end as sketched in Figure 2.9b. A step-wise increase in deflection causes the laser beam to move on the PSD which results in a linear voltage change as shown in Figure 2.9c. The slope of the linear regression can then be used to calculate the cantilever’s deflection at a given voltage change registered by the PSD. With the obtained deflection and dry film thickness, the temporal stress development can be computed. As can be seen from Equation 2.1, choosing a cantilever material with an appropriate Young’s modulus, allows adapting the setup in a way such that the prerequisite assumption for small deflections is met. That is, coatings with large stress development should be measured on a substrate with higher Young’s modulus such as steel. Alternatively, glass or silicon wafers can be used. However, we found that using materials different from the clamp material can cause distortions at elevated temperatures caused by stress induced through a variation in

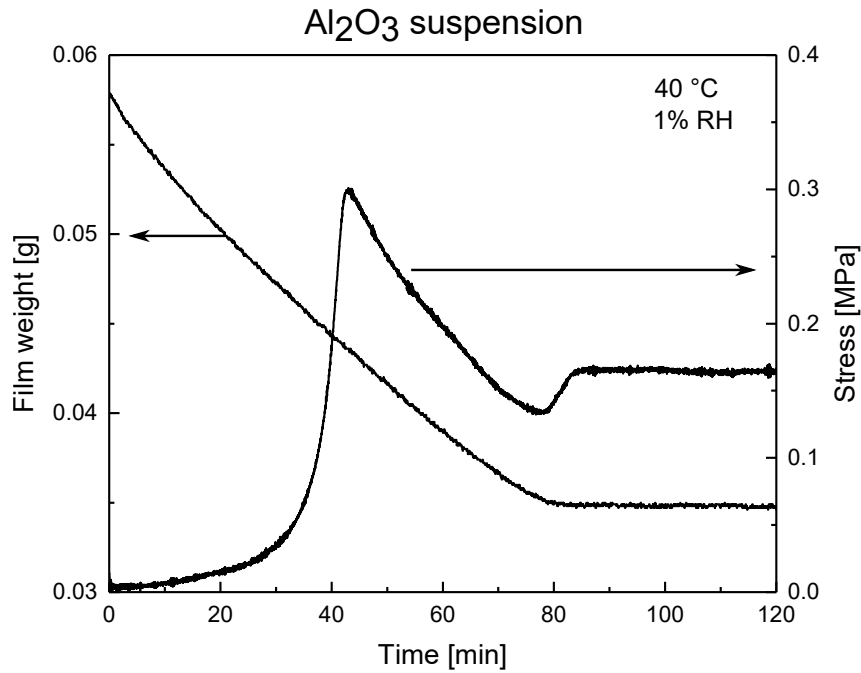


Figure 2.10: Simultaneous stress and weight measurement of 25 vol % alumina particles suspended in 1-heptanol with 3.1 vol % added glycerol, dried at 40 °C and 1% relative humidity over time. The left y-axis shows the film weight and the stress is shown on the right. Changes in drying rate can reliably and directly be related with the stress profile.

thermal expansion coefficients. Furthermore, the cantilever thickness can be chosen within technical and handling limits.

2.5 Application Example/Results

With the data obtained from an experiment as well as the calibration, one can directly compare changes in drying rate with the stress profile of the same coating. An exemplary result is illustrated in [Figure 2.10](#). This measurement shows the drying behavior of a capillary suspension prepared with alumina particles suspended in 1-heptanol and addition of a small amount of glycerol. The drying temperature was set to 40 °C and 1% relative humidity (RH). One can see that the initial drastic increase in stress is not correlated to the drying rate. Moreover, when the film is dry and the weight constant within the scale's resolution, there is still a stress increase that results in a coating with a constant residual stress. Further examples where this set-up was employed for investigation of capillary suspensions (also with the [USB camera](#)) can be found in Fischer and Koos [85, 90].

2.6 Conclusions

The drying behavior of coatings gives valuable insight into how to improve formulations in order to prevent defects such as pinholes or cracks, which are related to drying stresses. Since drying conditions, such as humidity impact the microstructural development and potential binder migration to the surface (skinning), reducing the drying rate, it is important to correlate both factors. The drying conditions will influence the drying rate, to show, for example, how the drying of multicomponent formulations under humid conditions can be beneficial for a stress reduction. Therefore, a test set-up with a controllable environment is advantageous. However, it was not previously possible to obtain the stress and drying rate simultaneously using the same coating in such a chamber. Either two specimen were dried in a chamber and results combined as if it was one, or results from simultaneous measurements, which could only be performed in ambient conditions, were extrapolated to the conditions of interest. In this work, we present an experimental set-up that allows the simultaneous observation of stress growth and drying rate of the same coating. This is of special interest for investigation of pastes where identical coatings are challenging to produce in a lab environment. The apparatus allows films to be reliably measured starting very shortly after the film spreading.

Data Availability Statement

The data that support the findings of this study are available from the corresponding author upon reasonable request.

Acknowledgments

The authors would like to thank Olaf Jörg and his team from the mechanical workshop as well as Bernhard Schweigler and Stefan Kollbach from the electrical workshop at the Institute of Mechanical Process Engineering and Mechanics at the Karlsruhe Institute of Technology (KIT), Germany for their input and precise work. Moreover, Herman Tollet from the CIT department at KU Leuven, Belgium is thanked for his passion when later corrections were necessary. Prof. Kyung H. Ahn from Seoul National University in South Korea is thanked for the opportunity to perform initial experiments in his lab as well as Dr. Sunhyung Kim for discussions and introduction to stress measurements. Finally, we acknowledge financial support from the German Research Foundation, DFG under project number KO 4805/2-1 and the Research Foundation Flanders (FWO) Odysseus Program (grant agreement no. G0H9518N).

3 Using an added liquid to suppress drying defects in hard particle coatings

Full title: Using an added liquid to suppress drying defects in hard particle coatings [90].

Authors: Steffen B. Fischer, Erin Koos

Status: published

Bibliographic data: *J Colloid Interface Sci* 582(Part B):1231–1242, 2021.
doi: <https://doi.org/10.1016/j.jcis.2020.08.055>

Authors can use their articles, in full or in part, for a wide range of scholarly, non-commercial purposes: Inclusion in a thesis or dissertation (provided that this is not to be published commercially).

www.elsevier.com/about/policies/copyright.

The article has been adapted in this thesis to reflect the numbering of references and citations in accordance with the manuscript. Additionally, the written part of the supplementary materials part has been included in the text.

3.1 Abstract

Hypothesis: Lateral accumulation and film defects during drying of hard particle coatings is a common problem, typically solved using polymeric additives and surface active ingredients, which require further processing of the dried film. Capillary suspensions with their tunable physical properties, devoid of polymers, offer new pathways in producing uniform and defect free particulate coatings.

Experiments: We investigated the effect of small amounts of secondary liquid on the coating's drying behavior. Stress build-up and weight loss in a temperature and humidity controlled drying chamber were simultaneously measured. Changes in the coating's reflectance and height profile over time were related with the weight loss and stress curve.

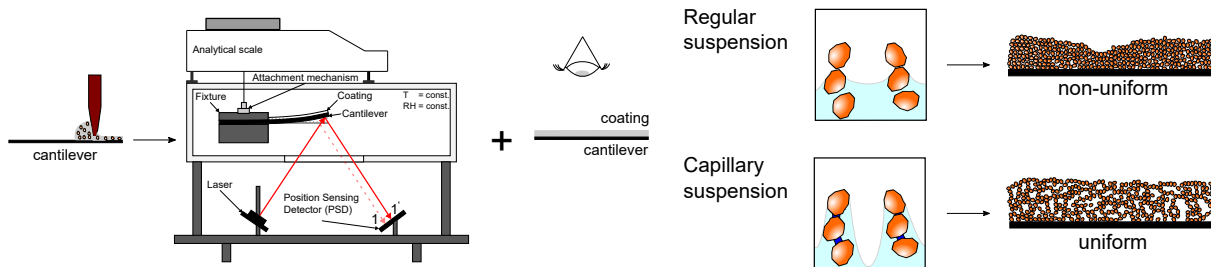


Figure 3.1: Graphical abstract to “using an added liquid to suppress drying defects in hard particle coatings”.

Findings: Capillary suspensions dry uniformly without defects. Lateral drying is inhibited by the high yield stress, causing the coating to shrink to an even height. The bridges between particles prevent air invasion and extend the constant drying period. The liquid in the lower layers is transported to the interface via corner flow within surface pores, leading to a partially dry layer near the substrate while the pores above are still saturated. Using capillary suspensions for hard particle coatings results in more uniform, defect free films with better printing characteristics, rendering high additive content obsolete.

3.2 Introduction

Particle coatings are widely used in various applications, such as protective paints and varnishes [2], production of thin film batteries [4], printing RFID tags for the IoT [5, 6], and printing solar cells at low cost [3]. In all these applications, correct functionality is indispensable. However, during drying of such coatings shrinkage occurs, which can cause cracks and other defects that can destroy their function. This can, for instance, allow mold growth in painted woodwork or rust in metals when they should be fully covered with protective paints and varnishes, or a loss of conductivity in the case of printed conductive pastes. This type of defect can also be observed in nature, for instance in the cracking of mud and silt [91]. These problems are not just limited to cracks. An inhomogeneous dry film thickness in the calendaring step during Li-ion anode production can cause stresses leading to fracture, or to an undesired porosity distribution in the cross section of the electrode [92, 93].

Drying of soft and hard particle suspensions typically follow the same basic stages of drying [15]. Before their application, the functional particles are suspended in a continuous phase. Initially, in the constant rate period, the drying film behaves as if there were no particles present. After establishing the equilibrium wet bulb temperature, the drying rate stays constant as long as the surface of the film is covered with liquid. Within the coating, however, changes in the microstructure caused by transport mechanisms can have

an influence on the coating properties. Cardinal et al. [16] mapped out three different regimes for colloidal suspensions: the sedimentation regime, in which particles settle in the liquid; the evaporation dominated regime where particles accumulate at the liquid-air interface, forming a consolidated layer and drying ‘top-down’ until a maximum packing is reached; and the diffusion controlled regime, which opposes the previously mentioned effects and forms a uniform coating. After the constant rate period, the next drying stage occurs when the film has compacted. Further evaporation forms pinned menisci between the particles on the interface. These menisci deepen and increase the capillary pressure in the pores. The pressure, p_c , can be described by the Young-Laplace equation:

$$p_c = \frac{2\gamma_{lv} \cos \theta}{r} \quad (3.1)$$

where the capillary pressure depends on the liquid-vapor interfacial tension, γ_{lv} , the contact angle θ , and the radius r of a capillary tube inscribing the neck between particles.

As drying continues and the liquid-vapor interface, also called drying front, recedes into the porous body, the drying rate decreases due to added vapor diffusion resistance from the pores to the surface. In the initial drying stage, the capillary pressure contracts its surroundings and the film shrinks. Later, when the film is fully compacted the capillary pressure induces stresses. If the top layers shrink first, there is a strain mismatch with the layer adhering to the substrate, which renders the bottom layer incapable of shrinking. This stress mismatch during drying can lead to cracking [58, 80]. Cracking during drying can be prevented by adding binders that take up stresses, i.e. sterically oppose the capillary pressure contracting the particles, resulting in a strong dry film. Another way of lowering the stresses in particle coatings is by decreasing the capillary pressure [62] e.g., by adding surfactants to lower the water-air interfacial tension [54, 64], according to Equation 3.1. This approach works well as long as the additives can remain in the film and no subsequent treatment of the coating is needed, as is the case in paints. Surfactants and binders, however, can be problematic if the coating obtained after drying is merely an intermediate step, such as a ceramic green body, where a subsequent pyrolysis step is needed before sintering. The same is true for printed electronics where neck formation between particles aids in the formation of an electrically conductive percolated network. The burn out can cause two major problems. First, if the pyrolysis conditions are not properly identified, organic residues may remain in the film, which can reduce the efficacy of the coating [65]. Second, since the polymers occupy space between the particles, non-uniform burn out can cause shrinkage and therefore the introduction of additional stresses and possible cracks [66].

Another phenomenon occurring during drying of particle laden droplets and coatings is lateral drying. Deegan et al. [28] have identified capillary flow as the root cause for the coffee-ring effect in which suspended coffee grounds accumulate at the edges of a drying droplet. The underlying mechanism is the pinning of the air-liquid-substrate contact line, which prevents a contraction of the interface towards the center. In order to balance evaporation losses, a fluid flux towards the pinned contact line occurs. This capillary flow has also been observed in film drying and manifests as lateral drying of coatings as observed by many researchers [54, 55, 94–96]. These capillary flows can lead to cracking as well as drying defects such as dimples or particle depleted trenches [72].

As previously mentioned, cracking can be diminished by the addition of soft polymers or surfactants, but this may cause problems or require additional processing steps for some applications. To reduce the amount of additives, Jin et al. [97] added a surfactant stabilized emulsion to a colloidal suspension. The effect was an increase in the shear moduli with a corresponding dramatic change in cracking. Another concept for suspension formulation uses capillary suspensions [9, 34, 41], where a small amount of a liquid immiscible with the bulk fluid was added to a suspension, which resulted in a dramatic change of its yield stress and elastic properties. In our previous work [8], we observed a remarkable decrease in crack formation for capillary suspensions even in the absence of surfactants. This paper investigates this phenomenon using a stress measurement apparatus to examine the stresses that are responsible for cracking. We compare the obtained stress curve with the visually observed drying features and put forward a hypothesis for the observed changes in the drying behavior of the capillary suspension in comparison to the regular suspension without added secondary liquid.

3.3 Materials and Methods

3.3.1 Sample preparation

Two different suspensions were formulated, differing only in the addition of a small amount of water. Alumina particles (α -Al₂O₃, CT3000SG, Almatix GmbH, Germany) with an average particle size of $d_{50,3} = 0.5 \mu\text{m}$ according to the supplier, were chosen for the solid phase. For the continuous phase, 1-heptanol (>99%, Alfa Aesar) was used. Particles were dispersed in multiple steps (at least twice for two minutes at 3500 rpm) with a Speedmixer DAC 150.1 FV (Hauschild & Co. KG, Germany) to obtain smooth samples with particle volume fractions of $\phi_{\text{Al}_2\text{O}_3} = 0.2$. To form capillary suspensions, ultra-pure water (atrium 611 DI, Sartorius AG, Germany) was added to achieve a water volume

fraction of $\phi_{\text{sec}} = 0.025$, while maintaining a solid content of $\phi_{\text{Al}_2\text{O}_3} = 0.2$. The specimens were mixed at 3500 rpm in increments of two minutes, to prevent the samples from excessively heating. The mixer is designed in such a way that degassing after mixing is not necessary. The samples were stored in the polypropylene Speedmixer cups wrapped in parafilm until use. Films were coated onto stainless steel cantilevers, as detailed in the Supplementary Information.

For some experiments the samples were dyed in order to trace concentration gradients. Before mixing, a stock solution of 1-heptanol was prepared by adding trace amounts (266 ppmw) of oil red EGN (Sigma-Aldrich, Germany). It is highly soluble in oils and appears red in the form of powder as well as in solution, while practically immiscible in water. The secondary phase, water, was dyed with a stock solution (50 ppmw) of fluorescein, disodium salt (ACROS Organics, Belgium), which is UV active. It is highly soluble in water and immiscible in the oil. The dye appears red when dry, whereas it fluoresces in solution under UV light to appear yellow-green. For these experiments, a handheld UV lamp was added to the experimental setup.

3.3.2 Coating process

The samples were coated on stainless steel cantilevers with dimensions measuring 6 mm wide, 40 mm long, and 200 μm thick. The cantilever was clamped into a fixture between two small steel plates and placed in a milled and surface sanded coating support. The cantilever and fixture are shown in the supplementary information [Figure 3.2](#). Before coating with a ZUA 2000 doctor blade (Zehntner GmbH, Sissach, Switzerland), the samples were re-mixed for one minute at 3500 rpm in the Speedmixer, reconstituting well-mixed suspensions without agglomerates. The distinctly different rheological properties of a capillary suspension, such as shear thinning, high yield stress, as well as wall slip [41] required varying the coating parameters for each suspension. While the best film results for the regular suspension without any added water ($\phi_{\text{sec}} = 0$), were obtained at a coating speed of 0.07 m/s and a set gap size of 260 μm . The capillary suspension ($\phi_{\text{sec}} = 0.025$) required a pre-coating step with a spatula to spread the paste. The coating speed was increased to 0.29 m/s and the coating knife gap height was reduced to 230 μm in order to obtain a similar average dry film thickness. The doctor blade was dragged over the cantilever by means of a self built film applicator driven by a voltage regulated motor. Dry film thickness was measured with a digimatic micrometer indicator (ID-H530, Mitutoyo, Japan) with a precision of 0.0015 mm. Since the dry films are very delicate, special care had to be taken in carefully lowering the measuring stylus on the coating to prevent

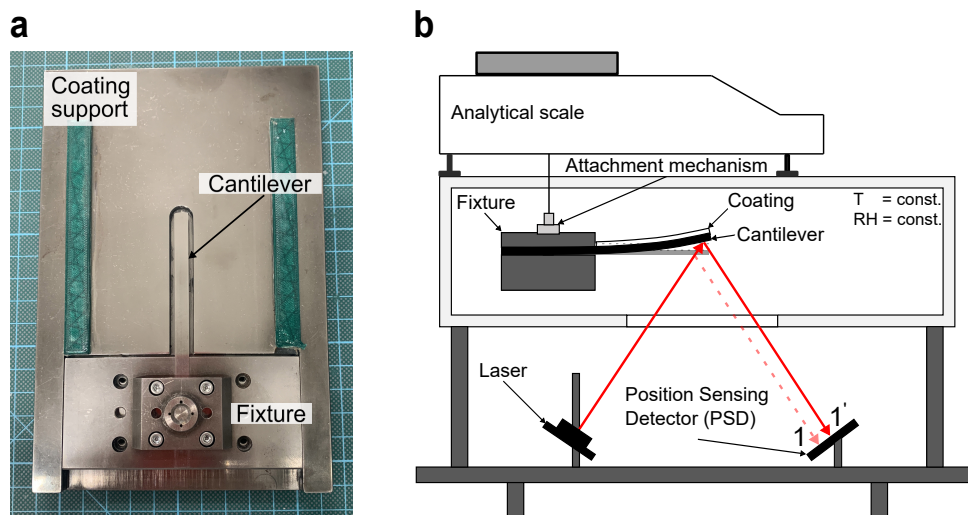


Figure 3.2: (a) Steel made coating rig with the clamped cantilever fixture placed in the recess of the rig. To maintain the cantilever's position, it is supported from below. Upon sample deposition, a coating blade with preset gap height is moved between the green rails along the cantilever with a constant coating velocity. (b) Schematic of the humidity and temperature controlled drying chamber. After coating, the fixture is inserted into the chamber, and attached to the analytical balance. Subsequently, the weight loss and cantilever deflection, tracked by the position sensing detector, are recorded.

excessive compression of the coating. The experiments reported here all had dry film thicknesses of $75 \pm 5 \mu\text{m}$.

3.3.3 Stress measurement and drying chamber

The stresses during drying are measured using the cantilever deflection method where bending of the substrate due to shrinkage of a well-adhered film is recorded with a laser. The drying rate is more difficult to obtain. Usually, a second cantilever is simultaneously coated and inserted in the drying chamber in order to link stress development and drying rate [80]. However, small differences of the coatings and drying conditions may lead to inaccuracies in attributing observed changes. To overcome these drawbacks, we designed a setup such that it is capable to simultaneously measure the stresses and drying rate of the same sample. The fixture with the sample coated cantilever (Figure 3.2a) is placed in a temperature and humidity controlled chamber (Figure 3.2b). The fixture is suspended from a scale while measuring the cantilever deflection with a laser. Drying was carried out in dry air at $40 \text{ }^\circ\text{C}$ with approximately 1% RH.

For this work, we placed a universal serial bus (USB) camera, lit with LEDs through a hole in the top of the chamber, below the scale. This camera imaged the front part of the cantilever, away from the clamp. Video recording was started simultaneously with the stress measurement to ensure comparability. For experiments with undyed samples, the LED light of the camera was turned on to illuminate the specimen. For the dyed

samples, we used indirect lighting through the chamber door, which is made of PMMA. Due to the restricted space available for the camera and its lack of wide angle capabilities, we only recorded the first 27 mm of the total coating length of 40 mm. The snapshots were processed in ImageJ [98]. The image intensity was adjusted using an adjacent area that was not subject to drying in order to account for changes in light or camera shutter adjustments. Subsequently, the obtained gray values were contrast enhanced with a constant color palette for each measurement, referred to as false color in the figures below.

3.3.4 Film shrinkage

For the film shrinkage measurements, the drying setup of Prof. Schabel's Thin Film Technology group (TFT) at the Karlsruhe Institute of Technology (KIT) was used, as described in Baunach et al. [99] and Jaiser et al. [19]. The drying chamber constitutes a temperature controlled movable plate, which was set to 30 °C or 40 °C. Relative humidity could not be controlled in this experiment. A laser profiler (LJ-G015, Keyence, Japan) with a line width of 7 mm covering the whole scanning width of the cantilever (6 mm) is mounted to the chamber. The impinging air flow was shut off in order to achieve comparable conditions as in the drying chamber used for stress measurements. After coating the cantilevers, we placed them on the heated plate and measured the profile thickness in intervals of ten and five minutes for the lower and higher temperatures, respectively. It is noted that the drying conditions from a heated plate differ somewhat from a drying chamber. While drying times may be different, the qualitative change of shrinkage should remain similar.

3.3.5 Surface profilometry

Four cantilevers were coated with a regular suspension as well as a capillary suspension with $\phi_{\text{sec}} = 0.025$ according to the previously mentioned method, and subsequently dried in the stress measurement chamber at temperatures of 30 °C and 40 °C at 1% RH. Afterwards, their film thickness profile was measured with a DektakXT stylus surface profilometer (Bruker, USA). A map scan was performed with a resolution of 100 μm per trace spanning 5000 μm . The examined cantilever area was chosen such that it reflected special features of the dry film.

3.4 Results

3.4.1 Comparison of stress curve features with drying images of a coating

The stress profile, image intensity and photographs of the coatings at different drying times are shown in [Figure 3.3](#) for both the regular suspension in the upper row (a,b) and for the capillary suspension with an added water content of 2.5 vol% in the lower row (c,d). [Figure 3.3a](#) and [Figure 3.3c](#) show the film stress profiles, as measured during the drying process at 40 °C. The stress values are shown on the top panel right y-axis, and change in mass, expressed as the liquid loading on the left y-axis. The time-variant loading of the film is defined as:

$$\text{solvent loading} = \frac{m(t) - m_{\text{final}}}{m_{\text{final}}} = \frac{m_{\text{liquid}}(t)}{m_{\text{dry}}} \quad (3.2)$$

and can therefore, be greater than unity. Since the liquid loading depends on the gravimetrically determined difference in evaporated liquid, the solvent loading can only be compared if the attained films have similar residual fluid content in the film, as is the case for the films investigated in this work. Otherwise, a larger amount of residual fluid is attributed to the mass of the dry film. We further restricted these experiments to average dry film thicknesses of $75 \pm 5 \mu\text{m}$ to ensure the comparison of films without cracks and interference of other mechanisms. Additionally, we avoid bias introduced through stress dependence on film thickness as observed by Tirumkudulu and Russel [21]. We identified six different points in time according to the following criteria, labeled with Roman numerals (uppercase for the pure suspension and lowercase for the capillary suspension).

- I: the start of the measurement;
- II: the point where the stress increases faster than the initially linear slope (red tangent);
- III: the rapid increase in stress preceding the peak stress;
- IV: the peak stress of the measurement;
- V: the rapid decrease in stress following the peak stress;
- VI: a trough as the stress approaches the residual value.

[Figure 3.3b](#) and [Figure 3.3d](#) show photographs of the cantilevers at these key points. The images on the right have been recolored from blue to bright yellow (colormap below [Figure 3.3d](#)) to better show gradients and differences between images. These images are also available as [Video 1](#) ([Figure 3.3b](#)) and [Video 2](#) ([Figure 3.3d](#)). The intensity span for the color map was maintained within and between samples. The change in color is also depicted on the lower panels of [Figure 3.3a](#) and [Figure 3.4c](#), which show the intensity

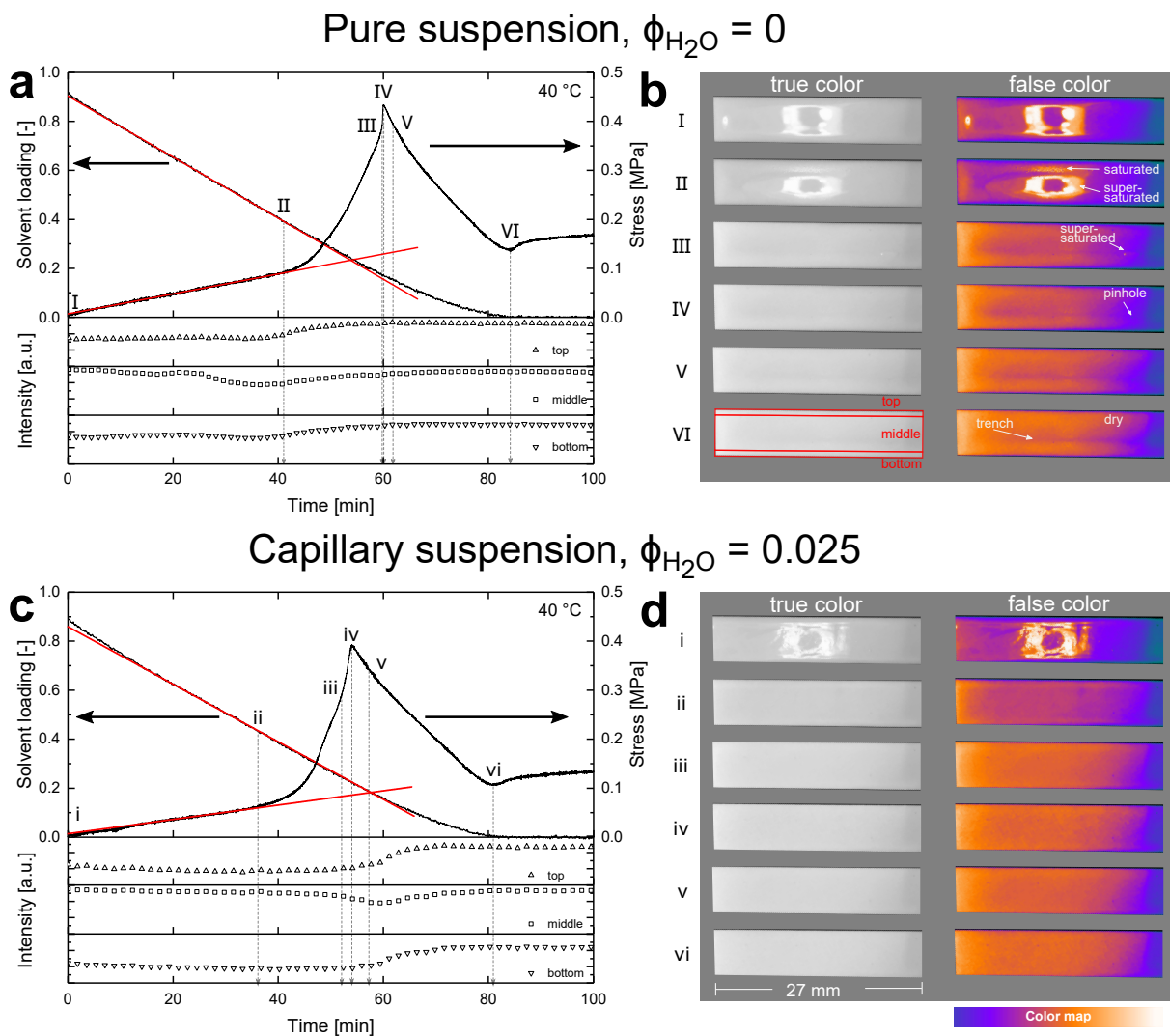


Figure 3.3: Results for (a,b) pure suspension without added water and (c,d) capillary suspension with $\phi_{\text{sec}} = 0.025$. The graphs in (a) and (c) show the solvent loading (top, left axis) and film stress (top, right axis). The lower panels describe the captured intensity change in three segments of the investigated coating (marked in b.VI). The top and bottom segments are narrower to capture lateral drying, whereas the middle segment is an average value of the remaining observable coating. The red lines mark the tangents in the constant rate period. The photographs in (b) and (d) show the cantilevers at different drying stages, marked in the graphs with Roman numerals. The films are directly lit with the camera's LED light, which is visible in the form of a circular ring of light that is reflected by a region of supersaturation as shown in b.II. The left column shows the true color image. In the right column, the true color image is converted to gray scale values and subsequently contrast enhanced with white showing bright areas and the dark areas in blue as depicted in the color map below (d). Both experiments were conducted at 40 °C and the scale is the same for all images. Videos of the false color images shown in (b) and (c) are available as [Video 1](#) and [Video 2](#), respectively.

values as an average value for narrow strips on the cantilever's edges as well as the middle of the cantilever (as marked in [Figure 3.3b.VI](#)). The behavior of films during drying is shown in [Figure 3.3](#). The coating is illuminated using direct LED lighting, visible as a circular ring in the glossy liquid coating in [Figure 3.3b,d](#), which amplifies intensity changes caused by drying features.

The stress curves for the pure suspension ($\phi_{\text{sec}} = 0$, [Figure 3.3a](#)) exhibits the typically observed stress increase, as labeled on the right y-axis [54]. There is a gradual stress increase up to point II, which coincides with the constant rate drying period. At that point, the tangent, shown in red, starts deviating from the constant mass loss (left y-axis). The images of the cantilever show that the first clear change in intensity appears in the middle segment for the regular suspension after about 25 minutes when the average intensity curve drops until point II is reached. This decrease is linked to the lateral drying, which reduces the reflected area. This decay is not visible at the edges, likely due to the curvature of the film near the edges (non-reflective narrow top and bottom segments in image I). However, we observe an intensity increase in all three segments near point II, when the stress increase accelerates beyond the linear slope. At this point, we see an increase in the reflection when the saturated (compacted) edges start to reflect the light (along and across the cantilever) and are superimposed with the decreasing reflection of the supersaturated area predominantly visible in the middle section. This observation can clearly be seen in the color enhanced image II in the center of the top segment. After that, the total intensity asymptotically increases and no further conclusions can be drawn from an intensity change. The supersaturated area subsequently decreases in width and length along the cantilever. The interface between the supersaturated and saturated regions has a pointy shape as shown in [Figure 3.3b.II](#). As the supersaturated region retracts towards the center of the cantilever, a particle depleted area, i.e. a trench [72], forms at its tip (as marked in [Figure 3.3b.VI](#)). A dimple, or pinhole ([Figure 3.3b.IV](#)), forms when the final droplet shaped supersaturated area disappears, as denoted in the contrast enhanced image [Figure 3.3b.III](#). The color changes towards yellow, indicating a dryer area, from the outside in as lateral drying continues. The trench and pinhole remain darker, making the contrast more visible.

The capillary suspension ($\phi_{\text{sec}} = 0.025$) results are displayed in [Figure 3.3c,d](#). Comparing the reflection of both suspensions in the first true color image, the surface of the capillary suspension appears rougher (scattered reflection), possibly due to the absence of a liquid film on the surface. As drying proceeds, there is no clear change in intensity in all three segments of the capillary suspension until point ii is reached. While there is barely a change in intensity between points i and ii, the comparison of the images at the respective

points reveals a difference. Even at point ii, which is reached earlier in the capillary suspension (36 min compared to 41 min in the pure suspension), the surface of the coating is no longer glossy and looks dry and devoid of a liquid surface film. However, the film is still in the constant rate period. Contrary to the regular suspension, the intensity of the middle segment decreases at point ii when the stress increase accelerates rather than increases. This continues until after point v, where the intensity in all three segments increase again. However, there is no clear link between this increase and any distinct points in the stress curves or images. After the peak, at point v, we reach the most obvious difference between the stress response for the two formulations. The constant rate period for capillary suspensions appears to be prolonged until point v, indicating the retraction of the liquid level into the film *after* the consolidation point, which is reached at the peak stress (point iv) according to the common theory of drying [55].

3.4.2 Dyed samples

To examine the mobility of the bulk liquid relative to the particles, experiments with dyed heptanol are shown in Figure 3.4. The stress response of these measurements resembles the undyed samples shown in Figure 3.3, albeit with a slight shift in the key times and maximum stress intensities. In the drying of the dyed regular suspension without added water (Figure 3.4b), the image intensity values (bottom curves) show a clear decrease for the upper edge of the cantilever (top rectangle), which indicates lateral drying that is more pronounced from the upper edge. A decrease in intensity can be explained by lower light reflection from dry parts compared to a glossy wet surface. This change in intensity is indicated in Figure 3.4b with a change in true color from darker red to a brighter red. The contrast enhanced picture depicts this behavior as a change from blue to more yellow. In II, a contrast difference marks the contour line of the supersaturated suspension. At point III, just before the final rapid stress increase (right y-axis), the intensity level in all three areas begin to rise. This intensity increase starts at approximately the same time across the cantilever denoting a reduction in the supersaturated area. This can be observed in terms of a color change towards more white on the true color or yellow on the false color images, respectively. Between point III and IV, which represent the final rapid stress rise, neither the averaged intensity values nor the images show any change in this short period of time. At point V, the initial stress release following the peak, the intensity increases but this change is gradual. In the images, however, a particle depleted area forming a trench down the center of the cantilever becomes visible. Additionally, the top left corner of the cantilever, which dried first, shows a darker red color. At point VI, there is an additional recognizable change of stress. Here, the stress reaches a local minimum, before

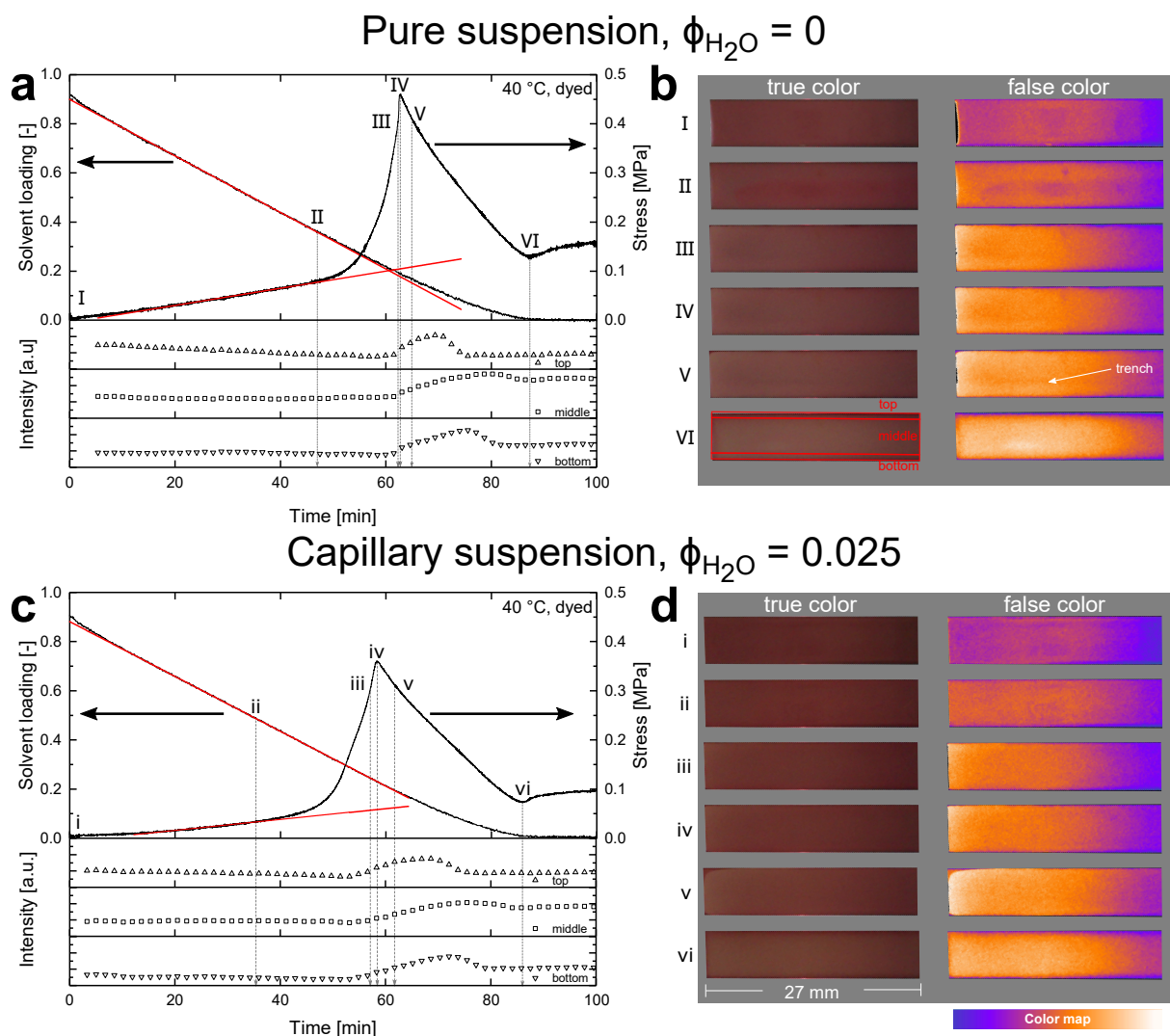


Figure 3.4: Results for experiments with dyed bulk heptanol phase showing (a,b) pure suspension without added water and (c,d) capillary suspension with $\phi_{\text{sec}} = 0.025$. The graphs in (a) and (c) show the liquid loading (top, left axis) and film stress (top, right axis). The lower panels describe the captured intensity change in three segments (marked in b.VI) of the investigated coating. The top and bottom segments are narrow to capture lateral drying, whereas the middle segment is an average value of the remaining observable coating. The red lines mark the tangents in the constant rate period. The photographs in (b) and (d) show the cantilevers at different drying stages marked in the graphs with Roman numerals. The left column shows the true color image. In the right column, the true color image is converted to gray scale values and subsequently contrast enhanced with white showing bright areas and the dark areas in blue as depicted in the color map below (d). Both experiments were conducted at 40 °C and the scale is the same for all images.

increasing towards a residual stress value. Looking at the fluid loading, it is evident that the last of the heptanol begins to dry, further compacting the film. Moreover, this seems to be in accordance with a small minimum of the intensity in the middle segment of the cantilever. One explanation could be fluid transport from the inside of the film towards the surface, with subsequent precipitation of the dye changing the reflection intensity of the light. In the images, this change was too small to be observed in the center of the film. At the edges, on the other hand, it is clearly more red than in the center of the cantilever. Looking at the false color image in [Figure 3.4b.VI](#), this is clearly visible as narrow blue area at the edges, transitioning to yellow with an almost white patch in the lower left middle segment.

Comparing the capillary suspension ([Figure 3.4c,d](#)) with the sample without added liquid ([Figure 3.4a,b](#)), we see particular differences. The stress increase (right y-axis) deviates from the constant rise (point ii) at an earlier time (35 min) for the capillary suspension than the regular suspension (47 min). At this time, the drying rate of the capillary suspension (left y-axis) is still constant, which is in contrast to the regular suspension where the stress and liquid loading curves both deviate at point II. There is also less change in the intensity of the top edge; the change of intensity between the beginning of the measurement and point ii appears to be more uniform. Between points ii and iii, the intensity increase, at approximately 55 minutes coincides with an inflection point in the stress curve. Here, the start of the intensity gain is not related to the final stress increase (point iii) near the peak but takes place about five minutes earlier. At point iii, we observe a moderate continuation of the stress increase towards the peak with a lower slope than for $\phi_{\text{sec}} = 0.025$. The contrast keeps gradually and uniformly changing albeit remaining darker near the edges. The capillary suspension coating does not show a sign of trench forming near the peak stress at point iv. However, drying appears to be lateral as well, observable from the darker top corner in the images at point v. The prolonged increase of the middle segment intensity supports this observation. At point vi, the middle segment seems to exhibit a small local intensity minimum in accordance with the local stress minimum. The final capillary suspension coating shows some dye accumulation at the edges but a more uniform dye distribution across the cantilever. The dyed heptanol, which acts as the bulk phase of the suspensions, seems to be transported to the edges of the cantilever, a sign of lateral drying. This mass transport appears to be reduced for capillary suspensions.

In order to elucidate the mass transport behavior of the water liquid bridges, we dyed them yellow with a water soluble dye, as shown in [Figure 3.5](#). In [Figure 3.5a](#), the stress profile is very similar to the capillary suspension with dyed bulk phase in [Figure 3.4c](#).

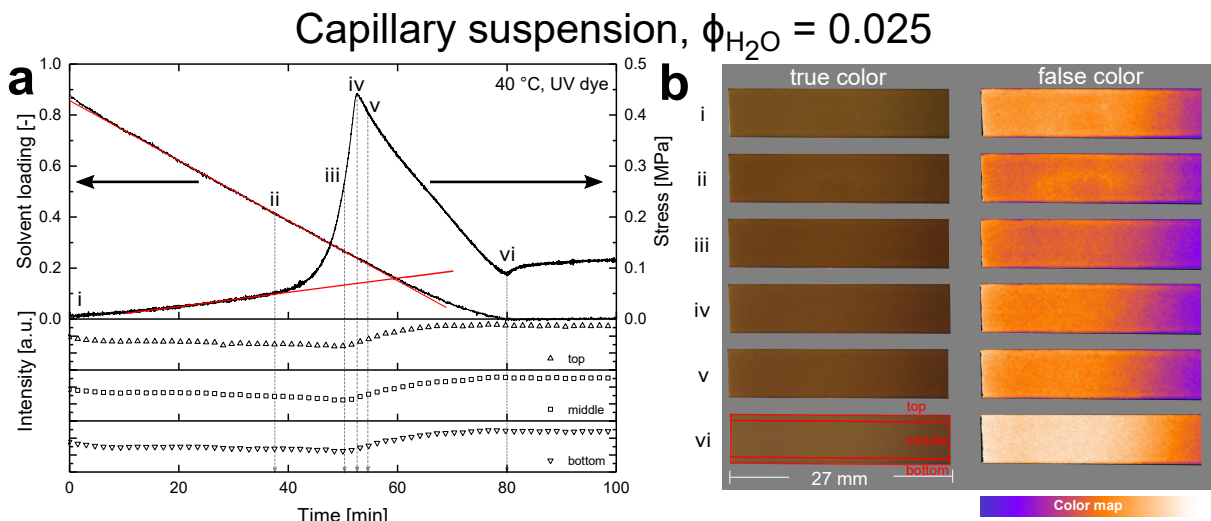


Figure 3.5: Results for experiments with dyed secondary water phase $\phi_{\text{sec}} = 0.025$. The graph in (a) shows the liquid loading (top, left axis) and film stress (top, right axis). The lower panels describe the captured intensity change in three segments (marked in b.vi) of the investigated coating. The top and bottom segments are narrow to capture lateral drying, whereas the middle segment is an average value of the remaining observable coating. The red lines mark the tangents in the constant rate period. The photographs in (b) show the cantilevers at different drying stages marked in the graphs with Roman numerals. The left column shows the true color image. In the right column, the true color image is converted to gray scale values and subsequently contrast enhanced with white showing bright areas and the dark areas in blue as depicted in the color map below (b). The experiment was conducted at 40 °C and the scale is the same for all images.

In this sample, point ii, marking the beginning of the stress rise, and the end of the constant rate period for the regular suspension, occur at nearly the same time as the previous capillary suspension sample, but the stress peaks at a slightly earlier time (53 min instead of 58 min) and has a higher value (0.45 MPa instead of 0.36 MPa). The intensity values shown in the lower panels of Figure 3.5a gradually decrease after the start of the measurement indicating a decreasing light reflection on the coating surface. The intensity begins to increase on the entire cantilever at, or shortly after, point iii when the rate of stress development subsides slightly. In contrast to the dyed bulk phase experiments, the dye intensity of the coating increases uniformly in all three segments, approaching their final values. This concurrent gain at the edges as well as in the middle part of the cantilever suggests a uniform drying where there is a uniform change over time across the cantilever. There is no visible accumulation of dye at the edges. This suggests that the capillary bridges, and thus the particles, are not transported towards the cantilever edges due to lateral drying.

Combined, the experiments in the drying chamber show key differences between the two formulations. The capillary suspension exhibits an extended constant rate period with the end of the linear regime occurring near the peak stress rather than near the initial stress rise as it does in the pure suspension. The images show that while both samples

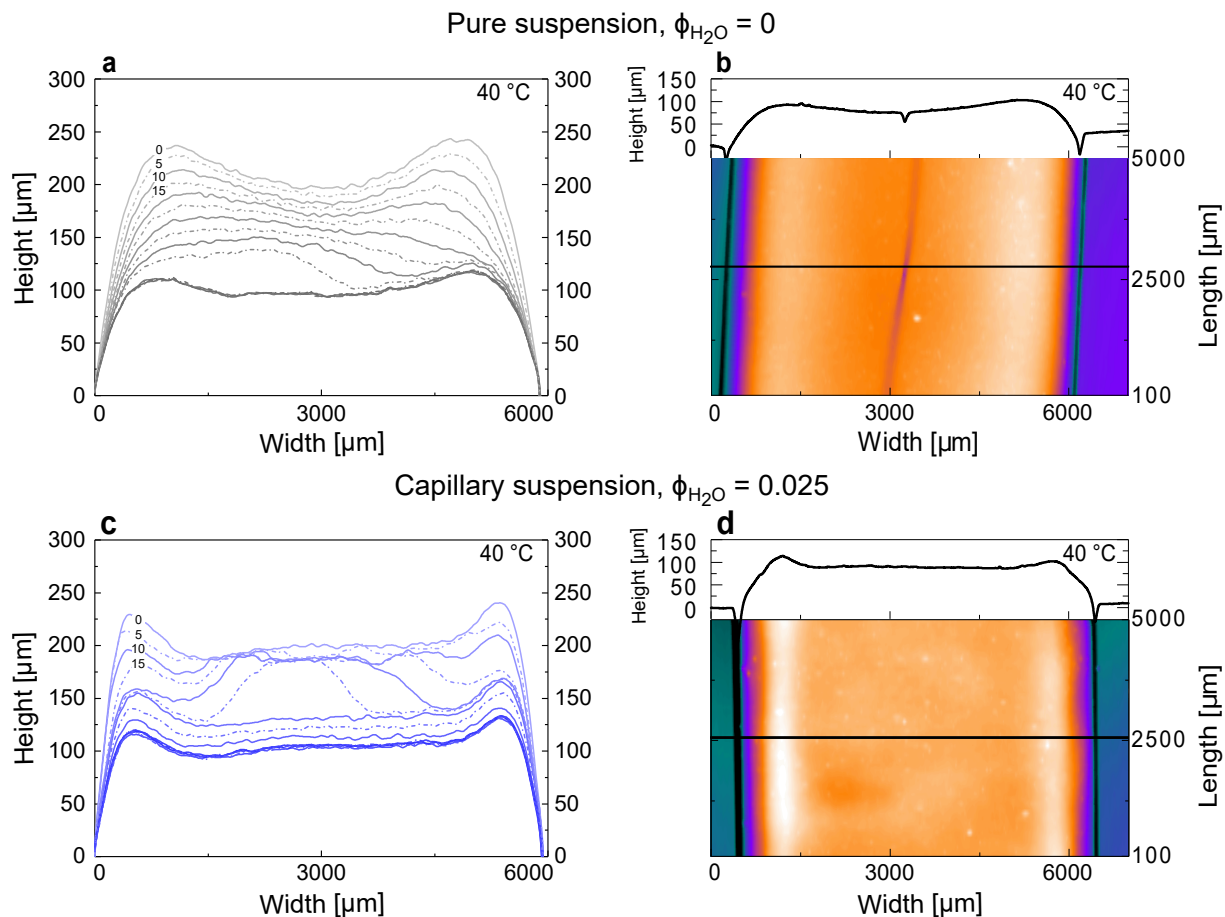


Figure 3.6: Film profile measurements of (a, b) pure suspension and (c, d) capillary suspension. The laser profiles during drying,¹ shown in (a) and (c) were taken every five minutes during contact drying at 40 °C and are displayed with solid and dashed lines in an alternating fashion. Increasing opacity of the curves indicate later stages of drying. The profiles in (b) and (d) capture a five millimeter surface section for films dried in the stress measurement chamber. The horizontal black line shows the cross sectional cut for the height profile in the upper panel.

undergo lateral drying, this is reduced in the capillary suspension. Any lateral drying in the capillary suspension is also not associated with particle transport and particle depleted areas (trenches or pinholes) do not develop, unlike the pure suspension. Differences in the lateral drying are further explored by investigating the film profile, as shown below.

3.4.3 Cross sectional profile change during drying

In the previous section, we observed a different drying behavior for capillary suspensions that suggests less prominent lateral drying. Additionally, light reflected and scattered on the coating surfaces implies a different topology. Therefore, we studied the change of a coating cross section for two suspensions over time, as shown in Figure 3.6a,c. Over the

¹ Performed at Prof. Schabel's lab. See [subsection 3.3.4](#)

course of drying on a heated plate, the height profile was measured in intervals of five minutes. The profiles in the graphs are depicted with more color saturation, as well as alternating dashed lines for increasing time steps. After coating the regular suspension ($\phi_{\text{sec}} = 0$) on the cantilever, we observed a significantly elevated film at the outside of the cantilever (Figure 3.6a). These edge effects depend on the intrinsic properties of the coating, such as elasticity or interfacial tension, as well as extrinsic application properties, such as coating speed or technique [92]. As drying begins, the film shrinks vertically across the cantilever, but this shrinkage is more pronounced at the edges. After about 25 minutes, the edges are nearly the same height as the center, implying that the film undergoes lateral drying. Pinning of the contact line causes the contact angle between the film and cantilever to decrease while the film is shrinking. Afterwards, the lateral drying slows and the evaporation in the center again dominates. This evaporation is enhanced on the right hand side of the profile, perhaps due to unbalanced natural convection. After roughly 50 minutes, the final compacted film structure is reached. This point should correspond to the peak stress (point IV) in Figure 3.3a and Figure 3.4a with the differences in time arising from the different drying methods. The compacted profile has a more leveled surface shape compared to the wet state, but is still clearly lower in the center. This final, dense state is maintained during the remainder of the drying process. The profiles of a film dried at 30 °C, shown in the supplementary information Figure 3.8, exhibits similar behavior albeit without the asymmetric drying. The small peaks and valleys between profiles are measurement uncertainties of the device.

The profile of a dry film, which was dried in the environmental chamber, is shown in Figure 3.6b, where lower areas are blue and elevated regions are red. The black line denotes the location of the height profile. The suspension without added water shows a very similar dry profile as in Figure 3.6a with slight superelevations despite the different drying conditions. Here, we have highlighted a trench covering almost the entire length of the cantilever with a pinhole in it. The dimple, representing the deepest depression of the trench is shown in the black height profile in Figure 3.6b. Additionally, the dry film surface is uneven across the whole cantilever. When we dried the regular suspension at a lower temperature, see Figure 3.8, we did not observe a trench formation but the pinhole is still present. Comparing the dry film thickness for the regular suspension at 40 °C (Figure 3.6a) and at 30 °C (Figure 3.8) combined in (Figure 3.9c), we can see a more even surface in the center and steeper, more prominent superelevations towards the edges at the elevated temperature, even while starting from a very similar wet film profile. This observation is also visible in the samples dried in the drying chamber and measured with the stylus when comparing Figure 3.6b and Figure 3.8b. Drying of the regular suspension

leads to particle depleted spots such as dimples or, at higher temperatures under more prominent lateral drying to trenches as already observed by others [72].

The drying profiles of a capillary suspension are shown in Figure 3.6c,d. The initial wet coating profile is substantially different from the regular suspension. The coating edge angle is closer to 90° than for the regular suspension, resulting in a better shape accuracy [50]. This shape accuracy is attributed to their high yield stress, shear thinning and excellent yield-recovery behavior [41]. The capillary suspension does have sharp superelevations but the height profile between the high edges is flatter. The height of the superelevations and the difference between the center height are roughly equal to the suspension without added water. These superelevations are a fault of the coating process caused by the cantilever edges and the intrinsic properties, as discussed earlier. Upon the start of drying, lateral drying occurs where the superelevations at the edges dry first, shrinking while the center remains at the same approximate height. After 15 minutes, the edges of the film lower beyond the height of the center as the lateral drying front propagates inward. In contrast to the regular suspension, the supersaturated wet area in the center remains at the same thickness such that a hill is formed. This persists until the superimposed lateral drying rates meet and the highest point in the center starts to evaporate. After 30 minutes, the hill on the surface has fully evaporated and the center once again forms a flat profile. This time corresponds to the beginning of the stress rise (point ii in Figure 3.3, Figure 3.4, and Figure 3.5), but is not coincident with the end of the constant rate period. Afterwards, the surface maintains its shape, while continuing to decrease in total height. Once the surface center is flat, it barely changes its form and appears to settle as a uniform body until the final thickness is reached. The final profile is obtained after 45 minutes. As with the pure suspension, this point where the film is fully compact should correspond to the stress peak (point iv). The profile of the dry film, Figure 3.6d, shows the superelevations and an otherwise flat profile devoid of defects. Unlike the pure suspension, there is no dimple or trench. This is remarkably different from the regular suspension since the final surface shape is already formed very soon in the drying process. At lower temperatures, the behavior is qualitatively the same (Figure 3.8), where we first see lateral drying and shrinkage of the superelevated edges. The evaporation is more prevalent on the right side of the film. As with the 40°C sample, the final film is flat with no defects at 30°C .

In summary, the pure suspension exhibits lateral drying throughout. The edges settle faster than the center, leaving a supersaturated area that leads to drying defects. The capillary suspension shape distinctly differs during drying. Initially, the edges dry in a lateral fashion until shrinkage stops before complete edge consolidation is reached. The

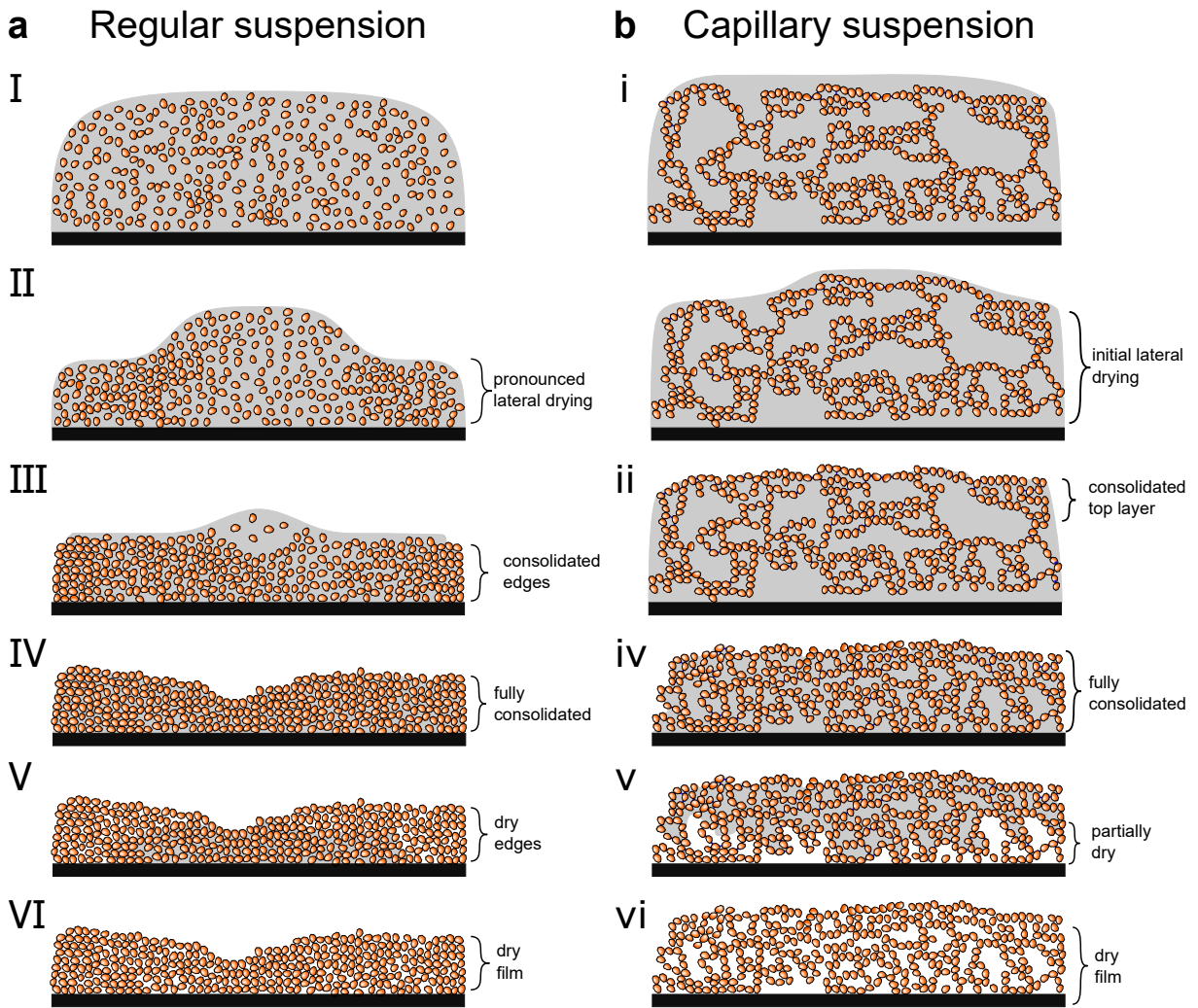


Figure 3.7: Schematic drawing of (a) a regular suspension without added secondary liquid and (b) a capillary suspension with added water. Key points in the drying process are marked using Roman numerals.

center nearly remains at the initial height and starts decreasing until a homogeneous surface has formed. Subsequently, the entire upper cross section homogeneously shrinks to the final coating thickness.

3.5 Discussion

The sketches in [Figure 3.7a](#) summarize the drying behavior of the regular suspension. These sketches are consistent with the experimental results and confirm the findings of other researchers for film drying of particulate coatings [21, 54, 55, 64, 72, 96, 100]. Initially, the film is supersaturated ([Figure 3.7a.I](#)). This supersaturation is confirmed by the highly reflective surface in the undyed sample ([Figure 3.3b.I](#)). As drying begins, the supersaturated coating transitions toward a saturated one through lateral drying

(Figure 3.3b.II). The lateral drying occurs as visually observed in the shrinking of the reflective region towards the center (Figure 3.3b.II) and darker region in the center of the cantilever for the dyed sample in Figure 3.4b.II. This is further supported by laser profiling during drying (Figure 3.6a). This lateral drying is uninhibited in terms of mass transport and solvent evaporates at a constant rate. As drying continues in the sedimentation regime (Figure 3.7a.II), particles start settling near the edges. This denser packing is seen in Figure 3.3a as the increase in the edge intensity beginning at II when the film enters the sedimentation regime. Increasing the particle loading at the edges also causes the fluid volume fraction to decrease, as shown in the steady decrease in bulk fluid intensity in Figure 3.4a at the edges relative to the center of the cantilever. Finally, the sedimentation causes the stress to rise and the solvent evaporation to slow, as shown at point II in Figure 3.3a and Figure 3.4a. The pinned contact line causes flow towards the edges, which further increases the stress and slowing of the evaporation after point II. At sufficiently high mobility, due to low particle loading and weak inter-particle interactions, flow and compressive stresses carry particles toward the edges (Figure 3.7a.III), leaving a trench (Figure 3.7a.IV). This particle movement, i.e stress release, is superimposed with the overall compressive stress rise, and leads to crack free films on the cantilever in this study. Trench formation was more pronounced at a temperature of 40 °C compared to 30 °C (Figure 3.8b) along with steeper superelevations. We attribute this phenomenon to the lower viscosity of the bulk phase at a raised temperature, which increases the particle mobility and a larger capillary pressure near the edges caused by deepening of pinned menisci between particles (see Equation 3.1) in an otherwise unchanged suspension. When drying continues beyond full compaction, air invades the pores of the film (Figure 3.7a.V), decreasing the number of menisci and thus the exerted stress on the film. Once the film is virtually dry (Figure 3.7a.VI), only the smallest pores in the film are saturated because of their large capillary pressure. These few, small menisci can still create extensive stresses in the film, as observed in Figure 3.3a and Figure 3.4a.

Capillary suspensions, on the other hand, dry very differently, as depicted in Figure 3.7b. Previous studies of pendular state capillary suspensions using confocal microscopy have shown that the secondary fluid creates bridges between two particles or, if the amount of liquid is higher, funicular clusters [34–36, 39]. In a consolidated coating, this corresponds to the secondary fluid being located at the throats of porous media. The connected particles form flocs, which are linked to each other, forming the backbone of a sample-spanning percolating network with a gel-like structure [37]. These particle clusters are illustrated in Figure 3.7b.i and are evident in the sample images as the initial film roughness observed in Figure 3.3d.i. Laser profile measurements during drying of capillary suspensions

(Figure 3.6c) revealed that lateral drying is only observed in the initial drying stage compared to the samples without added secondary fluid, as sketched in the second image in Figure 3.7b. The laser profile (Figure 3.6c) clearly showed that lateral drying ceases in the early stages of drying, subsequently leading to a consolidated upper layer and drying top down. That is, the top layer consolidates while the particle clusters in the lower area of the cross section are still well-distributed (Figure 3.7b.ii). We attribute this behavior to an increased yield stress due to increased particle-cluster interactions due to the higher particle loading where the film has consolidated. This compaction results in a locally more rigid gel network (higher compressive yield stress [101]) that counters further shrinkage of the film near the edges of the cantilever. Furthermore, the more compact upper particle layer near the edges results in smaller pores with smaller throats. These smaller throats probably act as capillaries, predominantly draining liquid from the larger pores in the supersaturated center region by capillary flow towards the edges, thus countering lateral evaporation [28, 61, 102].

A homogeneous consolidated layer forms at the surface across the entire cantilever, as shown in Figure 3.7b.ii, when the surface supersaturation is diminished. Usually, one would expect the drying front to recede into the pores at this stage, accompanied by a decrease in drying rate caused by larger diffusional mass transport resistances [96]. However, the constant rate period for capillary suspensions persists well after point ii, actually lasting beyond the peak stress (Figure 3.3c, Figure 3.4c, and Figure 3.5a). While this would normally be associated with a liquid surface, the directly illuminated capillary suspension sample illustrated in Figure 3.3d does not show any light reflection from point ii onward. This is quite unexpected since the regular suspension, which shows an earlier departure from the constant rate period, still shows supersaturated regions until point IV. One likely explanation is the superficially consolidated layer with menisci between the particles, which scatters the light in the capillary suspension [15]. This surface layer comprises a narrow pore and neck size distribution, furthering the capillary flow from the bulk to the evaporation surface. As the bulk liquid that is transported to the surface evaporates, the compressive stresses increase within the film. Once they exceed the compressive yield stress, the film starts to homogeneously shrink in height across the coating until a fully consolidated packing is reached (Figure 3.7b.iv). This point should coincide with the peak stress in the measurements and a fully saturated film [55].

After the fully consolidated porous body has formed, the surface must be kept sufficiently wet by means of liquid transport from within the body, as inferred from the constant rate period. Scherer [15] theorized the existence of a funicular state in a pore, where the pore walls are covered with liquid capable of transporting fluid. Later, Laurindo and Prat

[103] describe this phenomenon in more detail. Our observations for a prolonged constant rate period match their theory. For preferentially wetting systems, as in this study, the critical contact angles necessary for film effects to occur can be calculated [104]. Once the coating has consolidated, the liquid-particle contact angle decreases, allowing air to invade the body until the first critical contact angle is obtained. Once the angle reaches this first critical angle, liquid fingers are formed that transport liquid to the surface, keeping the drying rate constant. The liquid flows towards the surface, generating dry pores at the substrate (Figure 3.7b.v). The film stress begins to decrease in this period due to a decreasing number of filled pores exerting stress on the coating and substrate. Finally, when the second critical contact angle is reached at time v , flow ceases and the liquid starts depinning from the pore surface and air invades the pores, marking the beginning of the falling rate period [105, 106]. During this period, the film stress continues to decrease, albeit at a slightly slower rate than between point i and v , presumably due to slower drying, and thus, slower reduction of filled pores caused by vapor diffusion resistances.

The partially dry coating bottom, formed between point iv and v in the capillary suspension, is the effect of a constant drying rate beyond the close packed coating. However, we must question why we observe transport from the substrate as well as a prolonged constant drying rate. The capillary pressure over a curved surface, described by Equation 3.1, is the difference between the pressure of the invading fluid (air) and the pressure of the displaced fluid (1-heptanol). For invasion to take place, a critical threshold pressure has to be exceeded [107]. Invasion percolation (IP) rules for hydrophilically modeled media [105, 108], as is the case for the heptanol/water system investigated herein, dictates that invasion of a pore and throat has to be considered as two different mechanisms. Traditionally, once a throat is penetrated by air, it directly leads to the emptying of the adjacent pore and the start of porous body invasion halts the liquid flow. Thus, the obvious difference for capillary suspensions is the water bridge within the throats. These bridges must possess a higher invasion potential, and therefore, require higher air pressures before invasion occurs. Such an increase in pressure would result in a maintained corner flow and, thereby, also in a longer constant rate period for the capillary suspension. IP models for three phase flow in porous media [109], show that during gas invasion, oil filled pores empty first by pore size in decreasing order, followed by water filled pores in the same order. In three phase flow, oil can cover water bridges that are sandwiched between the invading air [110]. This phenomenon maintains the connection of the oil cluster, potentially resulting in better oil recovery in porous rocks. Micro-computed tomography (CT) measurements for drainage experiments with brine, oil and gas in porous carbonate rock support the theory that invading gas predominantly drains oil, while water occupies smaller pores

[111]. Translating these findings to drying of capillary suspensions, heptanol continues to cover the water bridges after consolidation and establishment of corner flow, leading to a connected oil cluster that persists longer than for the regular suspension, resulting in better drying.

In the previous study by Schneider et al. [8] using similar samples, capillary suspensions appeared to dry significantly faster than samples without added secondary liquid. However, our current experiments seemingly contradict these observations. The discrepancy can be explained by the different methods used in each experiment. Here, we use a gravimetric technique, whereas Schneider et al. [8] used Fourier-transform infrared spectroscopy (FTIR) coupled with an attenuated total reflectance (ATR) crystal, onto which the sample was coated. The sample composition is then determined at a location no more than a few micrometers above the crystal substrate. Therefore, the previous study only measured the interface between coating and substrate. In light of the present study, we have evidence for a partially dry coating near the substrate during drying of capillary suspensions as illustrated in Figure 3.7b.v, caused by corner flow and delayed air invasion into the porous body.

A study by Jin et al. [97] showed very similar behavior with a significantly decreased air invasion speed as capillary suspensions. Sterically stabilized colloidal spheres were suspended in an oil phase with surfactant stabilized aqueous glycerol emulsion droplets. Using confocal microscopy, they showed that the large emulsion droplets burst during drying and the aqueous glycerol subsequently occupied the space between particles. The collapsed droplets likely occupy the throats between particles. As we described earlier, water in small pores and throats surrounded and sandwiched by oil during drying inhibit air invasion as in the drying of capillary suspensions. The result was decreased, or even absent, cracking after drying in their sample dispersion. However, the incorporation of the droplets in their suspension caused the viscous modulus (G'') to be larger than the elastic modulus (G'), transitioning the formulation from a gel state towards viscous behavior. Such a viscous dominated response is undesirable for many applications such as screen printing. Upon stress build up during drying, the particles are able to release the stresses by simple migration. In lateral drying of circular droplets, this leads to a particle depleted zone or pinholes.

While lateral drying is suppressed and $G' > G''$ in the present capillary suspension system, the superelevations near the edges of the cantilever, as seen in Figure 3.6, remain a problem for various applications. The superelevations occur for both investigated suspensions, however they are more pronounced for capillary suspensions. These defects pose the risk of coating damage, for example during the calendaring step in the production

of Li-ion batteries [92]. Calendaring adjusts coating porosity, and superelevations lead to a denser percolated network, negatively influencing optimal current distribution. In this study, the coating was applied on a narrow and confined cantilever, which increases edge effects from the substrate. In most applications, films are usually printed on a flat surface, such as a copper foil, avoiding the substrate edges. Previous research on printing capillary suspension slurries for Li-ion batteries showed a clear improvement of contour sharpness as well as diminished superelevations [93]. The otherwise very even coating dried uniformly with only little lateral drying. Such uniform drying on a cantilever has only been observed with a modified substrate. Price et al. [77] added walls to their cantilever, which led to a more uniform drying of the coating, forming a packed surface layer across the entire substrate similar to the current results for capillary suspensions. The walled cantilever, however, caused some particle migration, resulting in concavely shaped edges, due to the pinned contact line at the wall.

3.6 Conclusions

On the basis of the capillary suspension concept [9, 34], we studied the drying of alumina suspensions in 1-heptanol enhanced with a small amount of immiscible water. Compared to the regular suspension, we only observe minimal, initial lateral drying and thus no particle accumulation near the edges of a flat substrate in the capillary suspension. The initial lateral drying locally increases the yield stress, preventing particle migration and leading to a packed surface layer, while the lower regions are still suspended. Surprisingly, we found that capillary suspensions exhibit a constant drying rate period that extended beyond the fully compacted state, in contrast to typical results expected for hard sphere suspensions film drying of particulate coatings, even with binders [83].

The differences between the drying of the capillary suspension and pure suspension without added water is studied using simultaneous stress and weight measurements, enhanced with imaging of the cantilever during the drying process. Such simultaneous measurements, presented for the first time in this paper, allow us to monitor the drying process at higher temperatures without making assumptions about the drying conditions [67, 76, 79–81]. These measurements are combined with additional profiling of the film surface to further elucidate the changes between the formulations. Using these combined measurements, we were able to determine that the extended constant drying rate period can be attributed to corner flow in pores near the surface. This phenomenon explains the seemingly contradictory observations of a non-reflective (i.e. partially dry) surface with the constant drying period. The capillary bridges formed by the added water (with

higher capillary pressure) prevent air invasion, extending the duration of the corner flow. Additionally, this flux leads to pore emptying near the substrate prior to the air substantially invading the top layers of a capillary suspension coating. In summary, capillary suspensions yield uniform coatings devoid of defects such as pinholes and trenches without the need for additives.

The absence of polymeric additives reduces subsequent processing steps, such as binder burn out [62, 65], and adds value to capillary suspensions with previously unrealized specifications on flat, narrow substrates [21, 54, 55, 64, 72, 96, 100]. The corner flow allows capillary suspensions to be efficiently dried under convective flow in industrial applications [112]. Furthermore, this capillary suspension method is capable of forming bridges with wide particle size distributions, and thus should reduce segregation of small particles during drying [8, 10, 36, 49, 113]. Segregation between large and small particles is a particular problem for formulations with binders; different drying conditions can cause binder to settle or be transported to the surface, leading to inhomogeneous films (demixing) [17, 114]. In capillary suspensions, the capillary bridges do not accumulate at a particular spot and small (binder) particles can even be isolated in the bridges [115].

In the present work, we examined the difference between a capillary suspension and pure suspension without added water. These experiments should be expanded to include differing secondary fluid fractions to investigate the link between the particle network structuring and drying behavior in more detail, as well as extended to different drying conditions. By varying the environmental conditions as well as the vapor pressure of the secondary liquid, we could potentially change the rate at which the bridges evaporate in comparison with the bulk liquid. This could be used to potentially control both the drying rate and the final film morphology. Finally, the present apparatus, which allows simultaneous measurements of the drying stress with the film weight and surface visualization, can be used to study other formulations. Edged cantilevers, made with photolithography, can be used to inhibit lateral drying allowing us to make a better link between the drying and formulation [77].

Acknowledgements

The authors would like to thank Almatix GmbH for the donation of alumina particles. We greatly appreciate Jana Kumberg and the entire Thin Film Technology group (TFT) of Prof. Schabel at the Karlsruhe Institute of Technology (KIT), Germany for help and access to the laser profiler. Dr. Frederik Ceysens, from the ESAT-MICAS department at KU Leuven, Belgium is thanked for access and an introduction to the stylus surface profilometer. Finally,

we acknowledge financial support from the German Research Foundation, DFG under project number KO 4805/2-1 and the Research Foundation Flanders (FWO) Odysseus Program (grant agreement no. G0H9518N).

3.7 Supplementary material

The video recordings (*Video 1* and *Video 2*) are available online at <https://doi.org/10.1016/j.jcis.2020.08.055>.

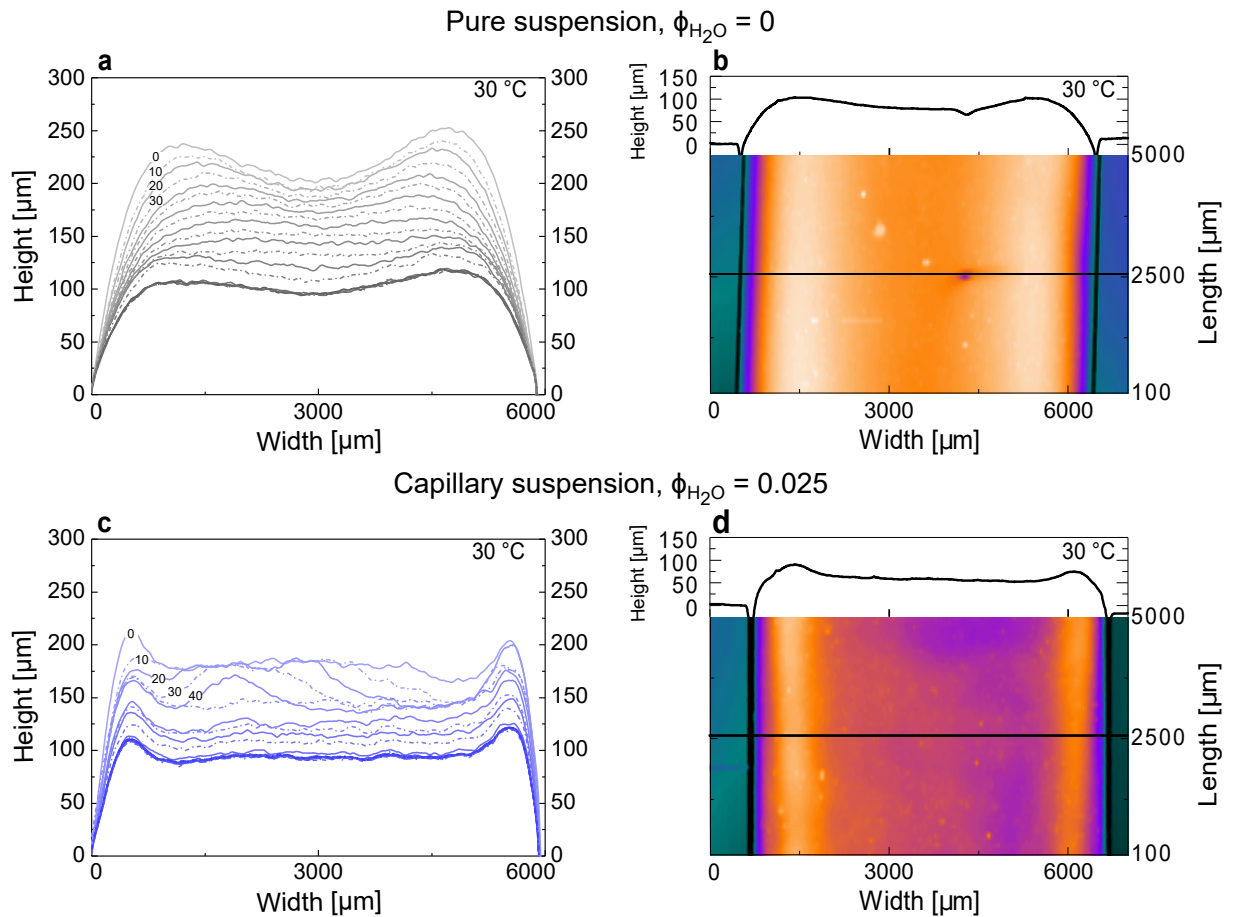


Figure 3.8: Film profile measurements of (a, b) pure suspension and (c, d) capillary suspension. The laser profiles during drying,² shown in (a) and (c) were taken every ten minutes during contact drying at 30 °C and are displayed with solid and dashed lines in an alternating fashion. Increasing opacity of the curves indicate later stages of drying. The profiles in (b) and (d) capture a five millimeter surface section of the dried films. The horizontal black line shows the cross sectional cut for the height profile in the upper panel.

² Performed at Prof. Schabel's lab. See [subsection 3.3.4](#)

Dry film comparison

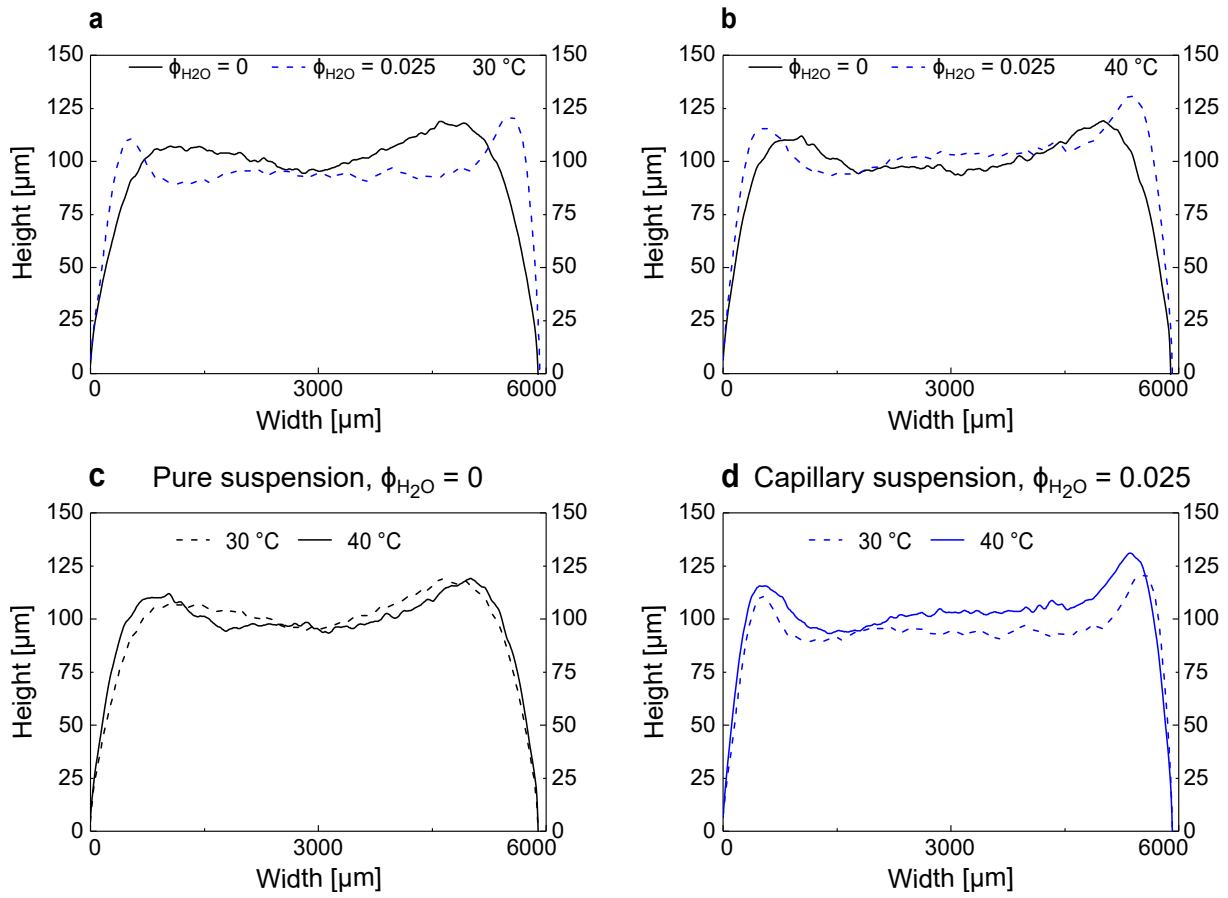


Figure 3.9: Dry film profilometry comparison. (a) Dry film of pure suspension, and regular suspension at 30 °C and (b) at 40 °C. (c) compares the dry film at 30 °C and 40 °C for the pure suspension, and (d) for the capillary suspension.³

³ Performed at Prof. Schabel's lab. See [subsection 3.3.4](#)

4 Influence of drying conditions on the stress and weight development of capillary suspensions

Full title: Influence of drying conditions on the stress and weight development of capillary suspensions [85].

Authors: Steffen B. Fischer, Erin Koos

Status: published

Bibliographic data: *J Am Ceram Soc.* 104(3):1255-1270, 2021.
doi: <https://doi.org/10.1111/jace.17553>

The Article is reproduced with permission from John Wiley and Sons. The article has been adapted in this thesis to reflect consistency and the numbering of references and citations in accordance with the manuscript.

4.1 Abstract

Cracking of suspensions during drying is a common problem. While additives, e.g. binders and surfactants, can mitigate this problem, some applications, such as printing conductive pastes or sintering green bodies, do not lend themselves to the use of additives. Capillary suspensions provide an alternative formulation without additives. In this work, we use simultaneous stress and weight measurements to investigate the influence of formulation and drying conditions. Capillary suspensions dry more homogeneously and with lower peak stresses, leading to an increased robustness against cracking compared. An increase in dry film porosity is not the key driver for the stress reduction. Instead, the capillary bridges, which create strong particle networks, resist the stress. Increasing the relative humidity enhances this effect, even for pure suspensions. While lower boiling point secondary liquids, e.g. water, persist for very long times during drying, higher boiling point liquids offer further potential to tune the the drying process.

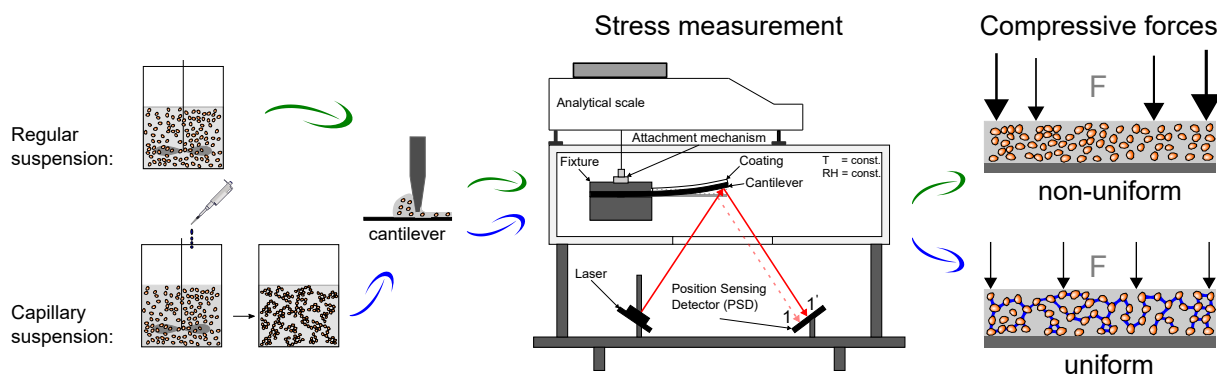


Figure 4.1: Graphical abstract. Simultaneous stress and weight measurement of the drying of capillary suspensions at different temperatures and relative humidities show that the bridges, which persist even after the evaporation of the bulk liquid, reduce the peak stress.

4.2 Introduction

Stress growth during drying of paints, inks and coatings is an important measure for developing defect free coatings. Stress is a direct measure of a film's proneness to cracking. In nature, we find crack patterns in things like mud cracks [91]. Examples of technical importance include drying of ceramic tape cast films [63], as well as subsequent green body binder burn out, where internal stresses can build up and lead to cracking [62, 65, 66]. Another example is represented by screen printing of conductive inks [5]. With increasing demand for low-cost solar cells and electronic gadgets, such as RFID tags, high throughput production is required [3]. The functional material is printed on flexible polymeric substrates with low glass transition temperatures. If drying of these electrically conducting circuits lead to cracks, their function would be destroyed. In order to print the circuits, or apply pigments, the functional particles have to be suspended in a liquid, forming a suspension. Upon application, drying sets in. Initially, the suspension dries continuously as if there were no particles present for as long as the surface is covered with liquid. This drying behavior is termed the constant rate period (CRP) [15]. Due to the evaporation of the liquid, the film shrinks and the solids density (particle volume fraction) increases. Generally, drying does not occur uniformly across the coating on narrow substrates or in droplet evaporation. In dilute systems, such as drying of a coffee droplet, this leads to the coffee-ring effect in which particles are transported towards the edges. The cause for this phenomenon, capillary flows, was identified by Deegan et al. [28]. As the droplet starts shrinking, the three phase contact line remains pinned at the substrate. Since the droplet perimeter stays constant and evaporation continues, there must be flow carrying particles towards the edges forming stains. The same phenomenon occurs during the drying of more concentrated suspensions. As the film dries laterally, transporting particles to the edges, particle depleted areas, or film defects, such as pinholes or trenches are left

behind [21, 54, 55, 72, 90, 94–96]. When drying proceeds and a compact film forms, the CRP decreases due to imposed mass transport resistances. The liquid filled voids in the saturated and consolidated particle coating represent pores and necks. Further evaporation pins the surface liquid to the pore mouths, such that concave menisci start to develop. This menisci formation causes pressure differences across the interface, which is described by the Young-Laplace equation for the capillary pressure p_c :

$$p_c = \frac{2\gamma_{lv} \cos \theta}{r} \quad (4.1)$$

Where the capillary pressure p_c , depends on the liquid-vapor interfacial tension γ_{lv} , the contact angle θ , and the radius of a capillary tube inscribing the neck between particles r . Continued evaporation and pinning of the liquid causes the contact angle to decrease, which leads to a larger capillary pressure. This, in turn, compacts the surrounding particles. If the coating is free to shrink in all directions, no stresses are observed. However, if the coating adheres to the substrate, which locally restricts the shrinkage, the strain mismatch can lead to severe cracking in hard particles or film formation for soft particles [58, 80, 116]. In order to prevent film fracture, there are different possibilities to modify the suspension. Avoiding the formation of small pores and particle mobility is achieved by addition of binders, which store the stresses and prevent delamination between the film and substrate.

Additionally, the flow properties of the suspension need to be adjusted for the application method. In many coatings, carboxymethyl cellulose (CMC) is used as thickening agent. However, a study by Wedin et al. showed a dramatic increase in peak stress during drying of a coating when CMC was added [67]. Furthermore, Equation 4.1 shows the direct relationship between the capillary pressure and liquid-vapor interfacial tension, which can be lowered through the addition of surfactants. In order to obtain an electrically conductive circuit, these additives have to be removed, which is usually done by heat treatment. However, on flexible, polymeric substrates with low glass transition temperatures, the treatment is restricted in terms of temperature. An alternative to solid additives that need additional treatment is provided by capillary suspensions. In capillary suspensions, the “binder” is a second liquid, immiscible with the bulk phase [9]. Upon the addition of a very small volume percent of this immiscible liquid, a dramatic change in rheological properties is observed [34]. The obtained capillary suspension exhibits an increase in the yield stress by several orders of magnitude, while showing shear-thinning behavior averting the need for potentially stress-inducing CMC, making these suspensions ideally suited for various printing applications [11, 50, 117] or ceramic bodies [51]. This change in properties is caused by the sample spanning particle network induced by capillary bridges of the secondary liquid. In our previous work, we found these novel suspensions reduce cracking

without addition of further additives [8]. More recently, we found capillary suspensions form a uniform final coating after drying, devoid of pinholes and trenches despite initially present lateral drying [90].

Since cracking is driven by stress build-up, stress measurements indicate the resilience of a coating. Many previous studies have tracked the stress formation of coatings using the cantilever deflection method due to its simple concept [21, 61, 78–81]. Moreover, this method allows the cantilever to be placed in a controlled environmental chamber. Besides the temporal stress measurement, the change in mass over time, i.e. drying rate, is another important factor in the coating’s drying behavior. However, this largely complicates the experimental setup. In several studies, the drying rate was obtained by coating another substrate, which was then weighed inside the same chamber, while the stress was tracked on the other substrate [59, 67, 76]. This approach works well, as long as the drying conditions in the chamber are spatially homogeneous and, most importantly, the coatings are identical. For capillary suspensions with their high yield stress, the sample application on the cantilever has proven to be challenging without introducing misinterpretations. Ideally, the stress development and weight loss are measured simultaneously. Studies by Kiennemann et al. [84] and Fu et al. [83] overcame these limitations by placing the clamped cantilever directly on an analytical balance. However, since the balance cannot be placed inside a small chamber with uniform drying conditions, their experiments were carried out under ambient conditions that are difficult to control. Our apparatus design, allows the simultaneous tracking of weight loss and stress development in the same coating inside a drying chamber under controlled conditions. This paper examines the differences in these quantities between a pure suspension and a capillary suspension with different types and amounts of secondary liquid under various drying conditions.

4.3 Materials and Methods

4.3.1 Sample preparation

Alumina suspensions were prepared at different particle volume fractions and with a variation of secondary liquid to obtain different rheological properties. Alumina particles (α -Al₂O₃, CT3000SG, Almatix GmbH, Germany) with an average particle size of $d_{50,3} = 0.5 \mu\text{m}$ according to the supplier were dried in an oven at 100 °C overnight and dispersed in 1-heptanol (> 99%, Alfa Aesar). Mixing of particles was performed in multiple steps (at least twice for two minutes at 3500 rpm) with a Speedmixer DAC 150.1 FV (Hauschild & Co. KG, Germany) and in 25 ml polypropylene cups ($\varnothing = 35 \text{ mm}$) to obtain

Table 4.1: Composition and coating parameters for each sample tested.

ϕ_{solid}	sec. fluid	$\phi_{\text{sec}}/\phi_{\text{solid}}$	Gap height [μm]	Coating speed [m/s]
0.20	–	0	250	0.07
0.20	water	0.075	250	0.09
0.20	water	0.125	230	0.29
0.20	glycerol	0.125	330	0.17
0.25	–	0	320	0.07
0.25	water	0.124	170	0.29
0.25	glycerol	0.125	170	0.17

smooth samples with particle volume fractions of $\phi_{\text{solid}} = 0.2$ and $\phi_{\text{solid}} = 0.25$. In order to create capillary suspensions, ultra-pure water (atrium 611 DI, Sartorius AG, Germany) was added with a micropipette to achieve the desired water volume fractions of $\phi_{\text{H}_2\text{O}}$. These fractions were chosen to keep the ratio of the volume of the secondary liquid bridges (ϕ_{sec}) to the particle volume fraction (ϕ_{solid}) constant, as shown in [Table 4.1](#). For spectrometry measurements, we used heavy water (D_2O , 99.9 atom% deuterium, Sigma-Aldrich). Additionally, we prepared samples with glycerol (> 99.0%, GC grade, Sigma-Aldrich), at the same volume fractions. After the addition of the secondary liquid, the samples were again mixed at 3500 rpm in the Speedmixer. The duration depended on the smoothness of the samples after one mixing step of two minutes. If agglomerates were still present, another two minute mixing step was applied until agglomerates were no longer visible. The reason for stepwise mixing is to prevent the sample from heating. The samples were stored in the polypropylene Speedmixer cups wrapped in parafilm and remixed before use.

4.3.2 Coating process

In order to repeatably and uniformly coat the cantilever, we manufactured the small coating rig shown in [Figure 4.2a](#). At first, the stainless steel cantilever was clamped perpendicularly in the fixture between two sanded steel slabs such that the available area for the coating measures 6 mm wide and 40 mm long. The cantilever’s thickness is 200 μm . After clamping, the fixture was then placed in the recess of the coating rig, where the cantilever was supported to prevent bending while coating. This bending can lead to an inhomogeneous wet film thickness along the cantilever. Before use, the samples were remixed at 3500 rpm for one minute, in order to have a well-mixed suspension before application. The pastes were deposited onto the cantilever and spread with a coating

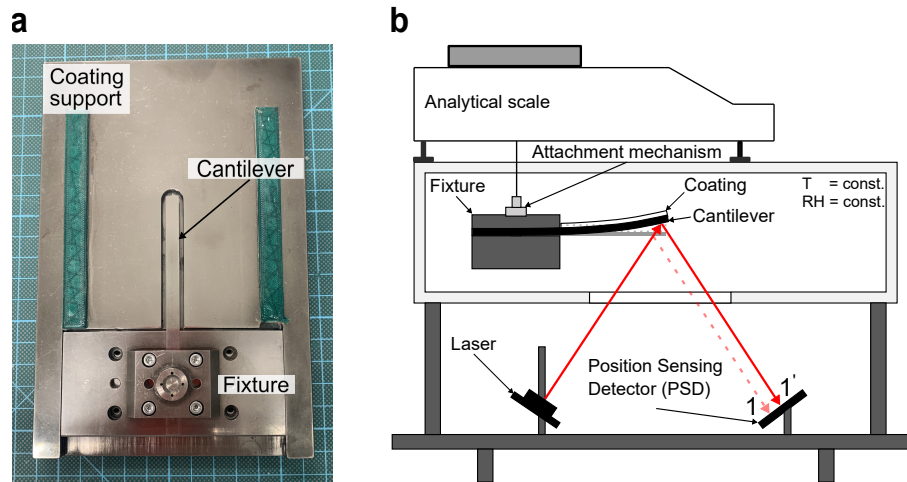


Figure 4.2: (a) The steel coating rig with the clamped cantilever fixture placed in the recess of the rig. To maintain the cantilever's position, it is supported from below. Upon sample deposition, a coating blade with preset gap height is moved between the green rails along the cantilever with a constant coating velocity. (b) Schematic of the humidity and temperature controlled drying chamber. After coating, the fixture is inserted into the chamber, and attached to the analytical balance. During the measurement, the weight loss and cantilever deflection, tracked by the position sensing detector, are recorded.

knife (ZUA 2000, Zehntner GmbH, Sissach, Switzerland) by means of dragging the blade between the green rails along the cantilever, driven by a voltage regulated motor. The high yield stress capillary suspension sample with ($\phi_{\text{H}_2\text{O}} = 0.025$) required a pre-coating step with a spatula to spread the sample. Besides the high network strength (yield stress) and shear thinning behavior, capillary suspensions also tend to exhibit wall-slip [41]. These properties make it necessary to adapt the respective coating settings. For example, the pure and lower magnitude capillary suspension ($\phi_{\text{H}_2\text{O}} = 0.015$) were coated at the same gap height of 250 μm but different drying speeds. Both quantities are summarized in Table 4.1 for each formulation. The dry film thickness was kept constant at $75 \pm 5 \mu\text{m}$.

4.3.3 Stress measurement in the environmentally controlled drying chamber

Our design of the stress measurement apparatus is shown in Figure 4.2b. The desired drying temperature is set on the controller and allowed to equilibrate for at least one hour. The desired relative humidity is obtained by manually mixing water saturated air, which was passed through a bubbler, with dry air at a total air flow rate of ≤ 8 liters per minute. After coating the cantilever according to the method described in subsection 4.3.2, the fixture with the clamped cantilever is quickly inserted into the drying chamber. This is done by means of a specially developed sliding and lifting device. The fixture is placed on the device, pushed inside the chamber and lifted so that it is connected to the attachment mechanism suspended from the analytical balance (Sartorius Cubis MSA 224S, Sartorius Lab Instruments GmbH & Co.KG, Göttingen, Germany) as shown in Figure 4.2b. The

attachment mechanism was designed to ensure the correct alignment of the clamped cantilever and is maintained between measurements and throughout the entire drying process. The mechanism, lifter, and door also allow the measurement to be started quickly (~ 30 seconds) after coating. After closing the chamber door, data acquisition is started. Laser light is directed to the polished bottom surface two mm from the free cantilever end where it is reflected and subsequently captured by the position sensing detector (PSD).

As drying proceeds, film shrinkage confined by good adhesion of the film to the substrate causes stresses, which are captured as bending in the cantilever. This bent cantilever causes the deflected laser beam to travel on the PSD from point 1 to 1'. Before the actual measurement, the setup was calibrated to correlate the movement of the laser on the PSD with the deflection of the cantilever. This was done by deliberately deflecting the cantilever a known distance with a micrometer screw while the entire fixture is in the measurement position. The stress in the deformed substrate was derived by Stoney in 1909 [73] for an uniaxial film stress, which was later corrected to a biaxial in plane stress due to an influence of the cantilever width, which is larger than the coating height [86]. Corcoran [87] later developed a correlation that takes the effect of substrate bending on the developed coating stress into account and is now widely used for determining stresses in drying coatings. The stress σ within the coating is given by

$$\sigma = \frac{d \cdot E_s t_s^3}{3t_c L^2 \cdot (t_s + t_c)(1 - \nu_s)} + \frac{d \cdot E_c (t_s + t_c)}{L^2 \cdot (1 - \nu_c)} \quad (4.2)$$

where subscripts s and c represent substrate and coating, respectively. The substrate (cantilever) thickness $t_s = 0.196$ mm, the Young's modulus $E_s = 210$ GPa, Poisson's ratio $\nu_s = 0.3$, and the cantilever's free length $L = 40$ mm.

However, the correlation contains quantities that are difficult to obtain. The coating thickness at the moment of drying t_c is unknown and instead the dry film thickness is used. Another unknown parameter is the coating's Young's modulus E_c , which is difficult to obtain in general and especially at different drying times. This drawback can be overcome if the experimental design is chosen such that the second term in Equation 4.2 can be neglected. In a similar study using alumina particles with added binders, the measured maximum Young's modulus after drying was 8.5 GPa [83]. The stainless steel cantilever in our study has a Young's modulus of 210 GPa, which leads to the first requirement for neglecting the second term: $E_s \gg E_c$. With a dry coating thickness $t_c < 80$ μm , the induced error by neglecting the second term is expected to be below 10% [83]. Moreover, several assumptions underlay Corcoran's equation, such as ideal adhesion of the coating on the substrate, isotropic elastic properties of coating and substrate, a uniform biaxial stress

in the coating, and small deflection, amongst others [87]. We did not observe an effect of coating weight loss on the deflection, but experiments at 40 °C and 50% RH required that the fixture be pre-heated before coating to avoid condensation when inserted into the chamber. Given all of the assumptions, the result of the measurements will be in the correct order of magnitude, but should be considered qualitatively and in a comparative manner within this study. Error in peak stress measurements are calculated from the standard deviation of at least five measurements.

The dry film thickness (t_c) was measured with a digital stylus micrometer indicator (ID-H530, Mitutoyo, Japan) with a precision of $\pm 1.5 \mu\text{m}$. Since the dry films are very delicate, special care had to be taken in carefully lowering the measuring stylus on the coating to prevent excessive compression of the coating. The film thickness was measured at more than 15 locations distributed along the length and off center of the film.

4.3.4 Shear yield stress measurements

Yield stress measurements, which provide a measure for a sample's network strength, were performed with a vane geometry (FL100/6W/Q1, 6 vanes, 22 mm diameter, 16 mm height) on a MCR 702 rheometer (Anton Paar GmbH, Germany). In order to investigate the temperature dependence on the yield stress, the prepared and sealed samples were placed in a lab oven at a constant temperature of 30 °C and 40 °C, respectively, and allowed to equilibrate. Before measurement, the samples were quickly remixed for one minute in the Speedmixer to account for any particle settling that may have occurred during temperature equilibration. Subsequently, the sample still in the mixing cup is placed in a modified temperature controlled cup holder. Upon lowering the vane into the cup, the sample was allowed to rest for five minutes to relax any induced stresses. Afterwards, a stepwise stress ramp was applied until yield occurred. The resulting strain vs. stress curve was then analyzed with the tangent method to obtain the apparent yield stress of the sample. Reported errors are from the standard deviation of triplicate measurements.

4.3.5 Thermogravimetric analysis with mass spectrometry (TGA-MS)

The coating is assumed to be dry, once a weight change is no longer detected. However, depending of the medium to be dried, there is an isothermal sorption equilibrium between the liquid in the coating and the ambient air. This equilibration depends on the relative humidity (in case of water evaporation), but also mass transport resistances in the film. Depending on the liquid, it is often undesirable to have residual fluid left in a coating.

Table 4.2: TGA profile for measuring the residual fluid content.

ϕ_{solid}	Stage 1		Stage 2	Stage 3	
	Temperature	Duration	Ramp	Temperature	Duration
0.20	30 °C	500 min	50 °C/min	500 °C	60 min
0.20	40 °C	430 min	50 °C/min	500 °C	60 min
0.25	30 °C	220 min	50 °C/min	500 °C	60 min
0.25	40 °C	160 min	50 °C/min	500 °C	60 min

In this work, we used two different instruments to determine the amount of liquid left in the film prepared by different formulations. At first, we used a thermogravimetric analyzer (TGA Q500, TA Instruments, USA). Less than 9 mg of the paste was weighed into a crucible. The amount was chosen such that the film height within the crucible was comparable to the film thickness on the cantilever. After placing the sample in the crucible, it was gently tapped on the table with tweezers to achieve equal spreading. Afterwards, it was placed in a suspended weighing pan attached to the TGA. The furnace was closed and the measurement started. The furnace and balance were always flushed with nitrogen gas at flow rates of 60 ml/min and 40 ml/min, respectively. The sequential stages followed the same principle. At first, the furnace was heated to the desired drying temperature where it was held until the sample was dry. Subsequently, the temperature was increased with a ramp of 50 °C/min to a temperature of 500 °C, where it was once again held constant. Afterwards, the residual fluid loading was calculated as the difference in weight before the temperature ramp and the weight at the end of the high temperature hold time divided by the weight at the end. The conditions varied for different sample particle volume fractions and are shown in Table 4.2.

Later, we analyzed the headspace composition during drying of the capillary suspension samples at drying temperatures of 30 °C and 40 °C. In this experiment, we are interested in the sequence in which the components evaporate. In order to save equipment time, we reduced the sample weight, i.e. film thickness. As before, the samples were deposited in the crucible and gently tapped on the table for spreading. Afterwards, they were analyzed in a TGA coupled with mass spectrometry (MS). Compared to the previous instrument, this TGA (STA 449 F3 Jupiter, NETZSCH-Gerätebau GmbH, Selb, Germany) differed in the measuring system, where the crucible was placed on a carrier system rather than being suspended. The drying gas was a mixture of 80 ml/min nitrogen and 20 ml/min oxygen to mimic air. In this measurement, only the samples with $\phi_{\text{solid}} = 0.2$ and $\phi_{\text{H}_2\text{O}}/\phi_{\text{solid}} = 0.125$

were analyzed. The stage 1 profile used a shorter holding time of 100 minutes and 180 minutes for 30 °C and 40 °C, respectively. The temperature ramp in stage 2 was also lowered to 20 °C/min.

Following evaporation, the gas passes through the mass spectrometer (HPR-20 QIC, Hi-den Analytical Ltd., UK) by means of the carrier gas mixture. The ionized and accelerated molecules are detected by a multiple ion detection (MID) scan. The characteristic mass to charge (m/z) ratios were detected at 20 m/z for D₂O and 56 m/z for 1-heptanol. We chose heavy water because 1-heptanol has a fragment peak overlapping with normal water at 18 m/z . After closing the furnace, the instrument was purged for several minutes. The measurement was subsequently started and sampling on both instruments were triggered. The MS has a delay of a few minutes compared to the weight change in the balance.

4.4 Results and Discussion

4.4.1 Stress development differences in capillary suspensions

In [Figure 4.3](#), the stress and weight development comparison during drying at 40 °C and a relative humidity of 1% is shown for two representative samples. The pure suspension of alumina dispersed in 1-heptanol is depicted in the upper row ([Figure 4.3\(a-e\)](#)), while [Figure 4.3\(f-j\)](#) shows the $\phi_{\text{solid}} = 0.2$ capillary suspension sample with 2.5 vol% water added ($\phi_{\text{H}_2\text{O}}/\phi_{\text{solid}} = 0.125$). The stress value is shown on the right y-axis and the solvent loading is shown on the left y-axis. The solvent loading is defined as

$$\text{solvent loading} = \frac{m(t) - m_{\text{final}}}{m_{\text{final}}} = \frac{m_{\text{liquid}}(t)}{m_{\text{dry}}} \quad (4.3)$$

with $m(t)$, being the film mass measured at time t . The measured dry film thickness for the pure and the capillary suspension were $71 \pm 1 \mu\text{m}$ and $69 \pm 4 \mu\text{m}$, respectively. The leftmost panels (a and f) show the entire stress and loading curve with excerpts thereof shown in the other panels. While the x- and y-scales differ for each of the excerpts, they are identical between the two samples (columns). The inset in each panel represents the entire stress curve with a box marking the magnified area depicted in the main panel. We have identified six key points, marked in the stress graphs with capital roman numerals for the pure suspension and lower case numerals (i-vi) for the capillary suspensions according to the following observations:

I start of the measurement;

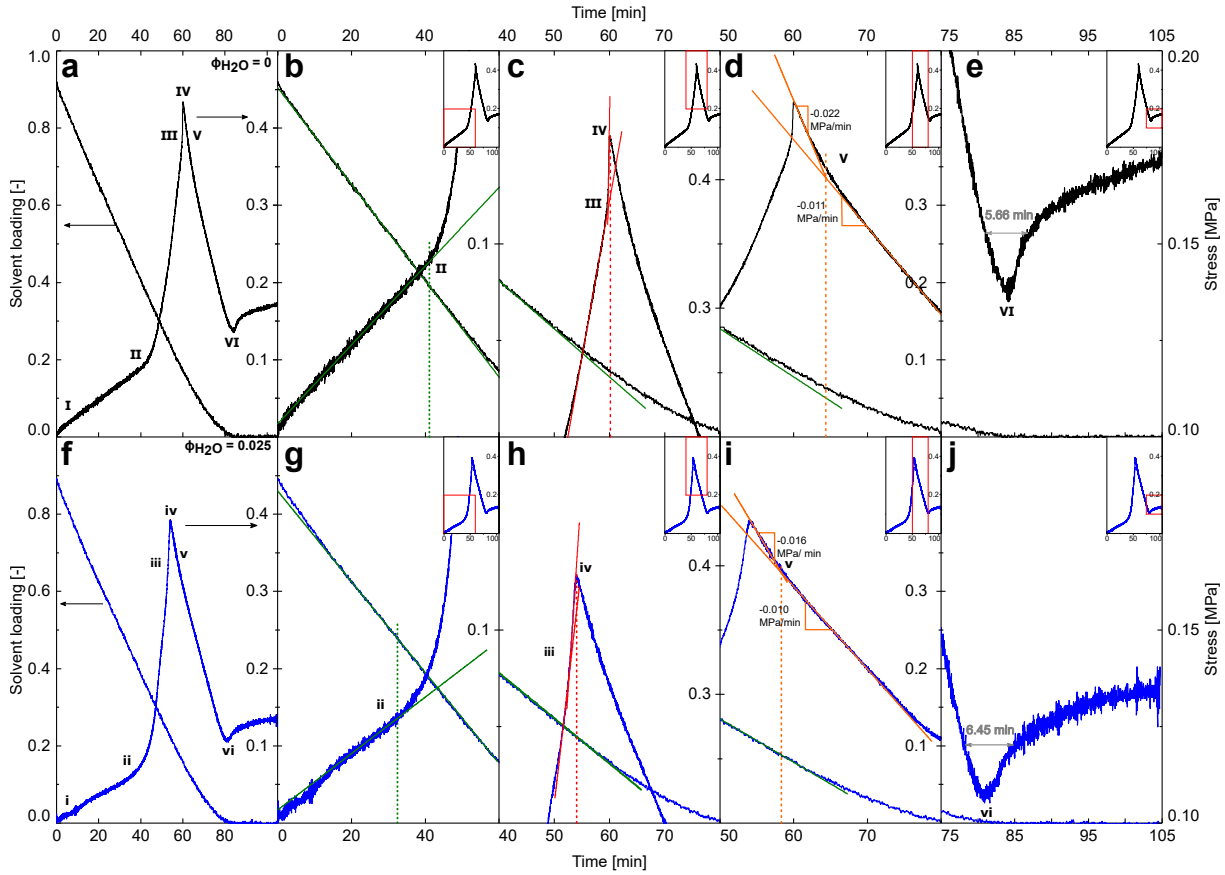


Figure 4.3: The results for simultaneous stress and weight measurement at a drying temperature of 40 °C and 1% RH for (a-e) a pure suspension sample and (f-j) a capillary suspension sample with 2.5 vol% added water, each at an initial solid volume fraction of 0.2. The left most panel (a,f) shows the entire stress and solvent loading evolution over time. The magnitude for the stress value can be found on the right y-axis and with its span being different in each column but the same for both panel rows. The magnitude of the solvent loading is shown on the left y-axis in each panel, where it is shifted relative to the stress curve in each column for better visibility of trends. The loading scale is the value shown on the left of each panel (the stress scaling from the previous panel). Special points of interest are marked in each panel with capitalized roman numerals for the pure suspension and lower case roman numerals for the capillary suspension.

II the point where the stress deviates from an initial linear trend;

III the rapid increase in stress preceding the stress peak;

IV peak stress;

V end of rapid stress decrease following the stress peak;

VI stress trough before the residual stress value is reached.

First, we will examine the findings of the pure suspension without added water ($\phi_{\text{H}_2\text{O}} = 0$) in conjunction with observations from a previous study [90]. Initially (I), there is a quick stress increase, quickly transitioning into a linear growth. In Figure 4.3b, the deviation of the stress from the linear growth (point II) coincides with increasing divergence of the

solvent loading from the constant rate period. Visual observation and profile measurements of the drying films reveal lateral drying [90]. Due to an increased drying rate near the edges and pinning of the contact line between the coating and substrate, the film starts consolidating near the edges first, while the remainder of the coating is still supersaturated [54, 55, 72, 90, 94–96]. This gradual increase in stress changes when a critical amount of menisci have formed, which leads to a more rapid increase in stress as the drying front propagates from the edges inward. When reaching point III (Figure 4.3c), a very rapid stress increase towards the peak stress (IV) occurs. Images of the film show that in this period, the final supersaturated patch or region vanishes until a fully compacted film forms at the peak stress, leaving a pinhole or trench [90]. Moreover, experiments with dyed heptanol suggest that the film is still completely saturated at that time [90]. Following the peak stress, a two-step stress relaxation takes place (Figure 4.3d). Stress release can have various superimposed causes. These causes range from the deformation and coalescence of soft particles [116], to undesirable crack formation and plastic deformation, such as particle rearrangement [118] often leading to unusable coatings. Another reason for stress relaxation is the reduction of stress inducing factors, i.e. evaporation of the menisci. When air starts invading the coating after point IV, the amount of liquid filled pores and menisci are reduced, leading to a decrease in equivalent pore stresses [78, 119]. We can exclude the formation of cracks since all examined films in this work were crack free. The reason for the two-step relaxation is not clear. However, a quick air invasion, i.e. menisci removal, along the edges of the entire cantilever could explain the fast decrease. Once the fractal drying front moves inward from all sides, the overall measured stress release decelerates due to the decreased area, and in particular, the shorter length where the stress acts. Eventually, the stress reaches a local minimum at point VI, before increasing again and approaching a final residual stress value (Figure 4.3e). At the local minimum, the film is nearly dry, however, due to capillarity and blob formation, small amounts of the final residual fluid occupies the smallest pores [102]. When air starts invading the remaining small liquid filled pores, the capillary pressure once again increases and, thus, the measured stress rises.

The stress and solvent loading profile of a capillary suspension with $\phi_{\text{H}_2\text{O}}/\phi_{\text{solid}} = 0.125$ is shown in Figure 4.3f. After the start of the measurement (i), the stress increases with a transition to a linear growth (Figure 4.3g). This transition occurs for the capillary suspension in a similar fashion as the pure suspension due to their nearly identical bulk fluid volumes. Unlike the pure suspension, when the stress increase deviates from its linear trend in the capillary suspension, the loading still remains in the constant rate period. Despite the similar stress increase between point i and point ii, profile analysis shows

significant differences between the two films. Initially, the capillary suspension also exhibits lateral drying, but to a lesser extent [90]. The edges constantly dry but only partially consolidate while retaining this critical height. We attribute this phenomenon to a locally increased yield strength that is larger than the compressive forces, i.e. capillary pressure. Capillary suspensions have a large yield stress immediately after formulation, due to the presence of a sample spanning network [34]. In this type of pendular state suspension, the particles are connected by water bridges, forming flocs. Connections between these percolated flocs form a path (backbone) throughout the sample (sample spanning network) [37]. As drying begins, the larger pores between the flocs compact (yield) and store some stresses. At the edges of the cantilever, where compaction has already occurred, the particle flocs form more percolating paths, which locally increases the yield stress and prevents the film from shrinking further, until the now higher intermediate yield strength is exceeded. While lateral evaporation persists, the denser packing near the edges wicks liquid from the surface supersaturated center of the cantilever until the yield strength of the film in the surface layers is equal across the cantilever. It is important to note that while the surface layers across the cantilever have compacted, the region below is still supersaturated. At point ii, this surface consolidation has finished and no supersaturated surface region is visible anymore [90]. As drying proceeds, the capillary pressure increases beyond the intermediate yield strength, causing the film stress to grow much faster than its previously linear trend during further compaction. This rapid increase occurs much earlier for the capillary suspension than for the pure suspension ($t_{ii} < t_{II}$). Qualitatively comparing the slope of the stress increase, we see a faster increase in the stress for the capillary suspension sample. A study by Price et al. [78], where they used a walled cantilever to suppress edge drying, showed the effect of lateral drying on the stress evolution. While lateral drying causes a generally slower stress increase towards the peak, the absence thereof results in a very rapid stress growth. That is, the capillary suspension with its faster stress increase dries more uniformly across the cantilever without using artificial walls. Shrinkage profile measurements support this observation of top-down drying after point ii [90]. While capillary suspension coatings exhibit larger superelevations near the edges of the cantilever compared to the regular suspension, this is due to coating application effects and are present already before drying. However, they retain their shape during the evaporation process in contrast to the regular suspension where particle accumulation (coffee-ring effect) is observed. The reason is the connected particle network and larger cluster structures compared to individually dispersed particles in the regular suspension. This also explains the almost uniform stress increase between point iii towards the peak stress (point iv), as depicted in Figure 4.3h, which is further substantiated by the lack of drying defects such as pinholes or trench formation in the capillary suspension film.

The point of maximum peak stress (iv) and, thus, the state of full film compaction displays several differences compared to the pure suspension. First, the peak is reached at an earlier time ($t_{iv} < t_{IV}$). Second, the peak stress for the capillary suspension sample is lower ($\sigma_{iv} < \sigma_{IV}$), which will be explored in more detail later on. Moreover, while the constant drying rate for the pure suspension has already ceased at point II, the constant rate period for the capillary suspension persists even beyond full compaction. This implies that despite the early development of a consolidated surface, which usually decreases the drying rate, the drying continues unabated such that the surface must be kept sufficiently wet. We ascribe this phenomenon to corner flow [103, 105], as described previously [90]. After the peak stress (point iv), the capillary suspension also shows a two-step stress relaxation (Figure 4.3i). In the capillary suspension, however, the first slope is clearly smaller in magnitude, i.e. displays a slower stress decay in the first step after the peak (-0.016 MPa/min) compared to the pure suspension (-0.022 MPa/min). Linking this first stress release to the drying rate and the fully compacted film, this implies capillary flow from inside the coating to the surface. This pore emptying through flow (decrease in equivalent pore pressure) must therefore be a slower process than pore emptying through Haines jumps. Additionally, we have shown in our previous work with dyed samples that point v corresponds to the appearance of the first dry areas transitioning to pore emptying by air invasion [90]. The second stress release step is only marginally, but consistently slower for capillary suspensions (-0.010 MPa/min versus -0.011 MPa/min). This may be caused by the capillary water bridges, which require a larger air invasion pressure than the bulk fluid. Heptanol covers these bridges, which protects them, and prevents sudden stress releases by air invasion into pores through Haines jumps, as is the case for the pure suspension [110, 111]. As a result, the heptanol cluster in the coating remains connected and should dry more gradually. Finally, the stress reaches its local minimum at point vi (Figure 4.3j), before once again increasing towards the final residual stress. The width of the trough (full width at half maximum) is wider for capillary suspensions (6.45 min) than for the pure suspension (5.66 min), which could be explained by larger pores, formed by the initial network structure, filled with remaining fluid. This should theoretically also lead to a lower residual stress. This residual stress is very sensitive to film variations in terms of film height and lateral drying, which made it difficult to identify a clear trend of residual stress dependencies.

Capillary suspensions exhibit distinctly different stress development features compared to the pure suspension. For capillary suspensions, the stress increase is more rapid, indicating reduced lateral drying, whereas the stress decrease is more gradual. Moreover, the peak stress, which is an indicator for a film's proneness to cracking, is reduced in the capillary

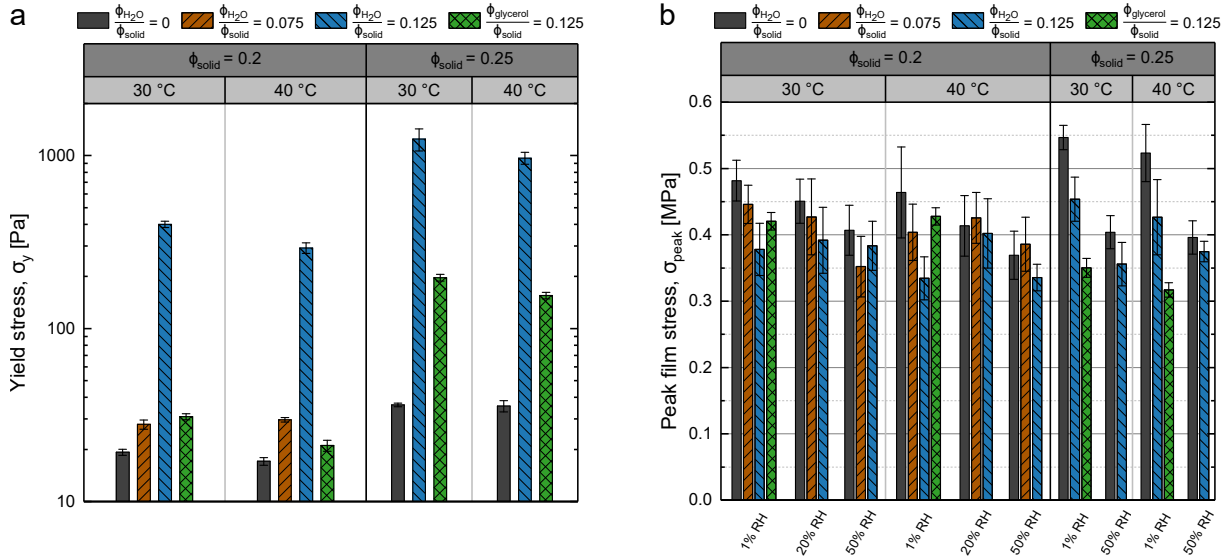


Figure 4.4: (a) Yield stress measurements of samples with a variation in secondary fluid contents and initial particle volume fraction, as measured at 30 °C and 40 °C. (b) The comparison in peak film stress for drying experiments with a variation in secondary fluid content and initial particle volume fraction performed at 30 °C and 40 °C as well as different relative humidities.

suspension. The differences and dependencies on drying conditions are examined more detailed in the following section.

4.4.2 Peak stress comparison

As observed in Figure 4.3, the measured peak stress is lower for the capillary suspension with $\phi_{H_2O}/\phi_{solid} = 0.125$ at $\phi_{solid} = 0.2$ and $\phi_{solid} = 0.25$ compared to the pure suspension. Generally, a sample without particle yielding exhibits larger stresses with increasing elastic strain acting on the sample network. The yield strength is, therefore, a measure of the coating's resistance to stresses. Because the yield stress of capillary suspensions can be modified through addition of water, the yield stress for the different formulations at the two temperatures is measured. The effect of a variation in secondary liquid volume on the yield stress, σ_y is marked with different colors (blue for the largest water addition) and patterns, as shown in Figure 4.4a. At a particle volume fraction of $\phi_{solid} = 0.2$, a relative volume fraction $\phi_{H_2O}/\phi_{solid} = 0.075$, only results in a small increase in yield stress. Further addition of water ($\phi_{H_2O}/\phi_{solid} = 0.125$) causes a dramatic increase in the yield stress by more than one order of magnitude. At larger particle volume fraction ($\phi_{solid} = 0.25$), the thickening effect is even stronger. The addition of the same relative volume fraction of glycerol ($\phi_{glycerol}/\phi_{solid} = 0.125$), on the other hand, barely increases the yield stress compared to the pure suspension sample for the lower particle loading. In contrast, the

yield stress significantly increases by half an order of magnitude at $\phi_{\text{solid}} = 0.25$. An increase in temperature only has a small decreasing effect on the yield stress.

Naturally, the drying conditions will also influence the peak stress, as shown in [Figure 4.4b](#). First, the drying temperature will influence the drying rate. At higher drying rates, one expects a larger peak stress due to smaller contact angles of the pinned menisci, leading to larger capillary pressures. A temperature induced decrease of the interfacial tension is not expected to balance the change in contact angle. Second, the relative humidity influences the drying of water while leaving the heptanol unchanged. The intention is to suppress drying of the capillary water bridges, such that the yield strength is maintained once the bridges are exposed to air. Exchanging water with the higher boiling point glycerol should further that effect. The influence of the discussed formulation changes and drying parameters on the maximum drying stress (σ_{peak}) is shown in [Figure 4.4b](#). To understand these results, we will first only consider water as the secondary liquid and a particle volume fraction of $\phi_{\text{solid}} = 0.2$. The black column (most left in each RH segment) represents the pure suspension. When evaporating into dry air (1% RH), an increase in water fraction results in a lower peak stress, both at 30 °C and 40 °C. While an increase in humidity decreases the peak stress for no and low amounts of added water, it has no effect on the sample with the highest water addition (blue, $\phi_{\text{H}_2\text{O}}/\phi_{\text{solid}} = 0.125$), which is in contrast to our expectation. This could be explained by the fact that the water capillary bridges remain until the stress inducing meniscus has receded further into the coating. Interestingly, the highest relative humidity (50% RH) significantly reduces the peak stress of all water fractions to a level comparable with the high yield strength capillary suspension ($\phi_{\text{H}_2\text{O}}/\phi_{\text{solid}} = 0.125$) at both examined temperatures. At elevated temperatures, one would expect larger peak stresses due to a reduction in the heptanol contact angle caused by the pinned menisci. Instead, there is no influence of temperature on the peak stress for the pure suspension. For the $\phi_{\text{H}_2\text{O}}/\phi_{\text{solid}} = 0.125$ and $\phi_{\text{solid}} = 0.2$ capillary suspension sample, the peak stress tends to decrease at higher temperature and 1% RH ($p \leq 0.07$, i.e. the means are different with a probability of more than 93 percent). From the small yield stress decrease ([Figure 4.4a](#)), one would have expected a larger peak stress in the absence of particle migration. However, the bulk viscosity of heptanol is also temperature dependent. It decreases from 5.090 mPa · s at 30 °C to 3.740 mPa · s at 40 °C [[120](#)]. This reduction may allow particle clusters that are not part of the sample spanning network, or have yielded already, to rearrange more easily resulting in a partial stress release. This rearrangement would most likely occur in the lower layers, which are still uncompacted before the stress peak.

The pure samples show more pronounced lateral drying at higher temperatures [90]. This more pronounced lateral drying leads to trench formation and causes more particles to migrate, thus releasing the evolving stresses. Therefore, the maximum stress, which is expected to be larger compared to a lower temperature cannot be independently measured since the stress accumulation and stress relaxation through yielding and particle migration are superimposed. Increasing the initial solid load to $\phi_{\text{solid}} = 0.25$ leads to smaller liquid volume between the particles. In non-stabilized suspensions, this leads to more particle-particle interactions upon lateral drying, with the result of restricted particle migration (reduced trench formation and pinholes) and, consequently, a larger stress formation due to the absence of stress relaxation through particle migration [55]. Indeed, as shown in Figure 4.4b, the pure suspension at 1% RH displays a larger peak stress than at lower volume fraction. This trend holds for both drying temperatures. Interestingly, the capillary suspension ($\phi_{\text{H}_2\text{O}}/\phi_{\text{solid}} = 0.125$) peak stress at 1% RH is also larger for the larger particle load. Increasing the temperature does not significantly affect the peak stress. Due to the larger particle-particle interactions at $\phi_{\text{solid}} = 0.25$ than at the lower solid load, the sample-spanning network is reinforced and particle rearrangements are inhibited. Increasing the relative humidity at higher particle loads again significantly lowers the peak stress of the pure suspensions. Even for the capillary suspension, there is an additional decrease in the peak stress with increasing humidity that is not observed in the lower particle volume fraction.

Exchanging the secondary fluid for glycerol has two immediate effects. First, the yield stress for a capillary suspension with the same volume of secondary fluid $\phi_{\text{glycerol}}/\phi_{\text{solid}} = 0.125$ is much lower than when using water, especially at $\phi_{\text{solid}} = 0.2$ (Figure 4.4a). This change is due to the lower interfacial tension of glycerol. Secondly, glycerol evaporates at 290 °C, which means it essentially does not evaporate under the examined conditions and should remain completely in the film. As expected due to the only slightly larger yield stress for the glycerol capillary suspension at lower particle load, the reduction in peak stress compared to the pure suspension is small (Figure 4.4b). In contrast, the larger σ_y at higher initial solid content causes an immense reduction in peak stress of approximately 40%. This exceeds the reduction measured for the water sample at 1% RH despite the higher yield stress. This observation, along with the decrease in peak stress at 50% RH, suggests that water lowers the coating's resilience against shrinking stresses.

We have shown that the peak stress can be reduced by using capillary suspensions in drying coatings. Changing the drying temperature did not generally lead to a change in the peak stress. Interestingly, we found that an increase in humidity can lower the peak stress of the pure suspension and capillary suspension at high particle load (whereas no

change is observed at $\phi_{\text{solid}} = 0.2$). Capillary suspensions change the microstructure of the final film. Since larger pores should reduce the capillary pressure and thus the peak stress during drying, we further examine these effects in the following section.

4.4.3 Film morphology at the peak: Residual fluid

In the previous section, we observed the addition of a secondary fluid, which changes their yield strength, decreases the peak stress. While non-stabilized suspensions can flocculate due to van der Waals forces, a capillary suspension represents a highly flocculated system where the capillary force (originating from the secondary fluid bridges), is much stronger [9, 34], leading to the yield stress increase as displayed in Figure 4.4a. However, this network formation may also result in a different microstructure of the coating. The film density, that is the final packing volume of a coating, is a measure of its porosity. The simultaneous stress and weight measurement used in this study allows us to directly estimate the final packing volume fraction in a reliable way based on a few simple assumptions:

1. For the systems with added glycerol, the glycerol is treated as inert and remaining completely in the film.
2. For the systems with added water, the water volume in the capillary bridges is treated as heptanol (the densities are approximately equal and there is no difference in their distribution within the film).
3. When the stress has approached its residual value, the film was considered dry (devoid of any volatile components). Due to small noise in the weight signal, the final dry mass m_{final} is the averaged value over the last 100 recorded data points (50 seconds).
4. The volatile liquid content of the dry film (isothermal sorption equilibrium) is negligible ($V_{\text{final}} = V_{\text{Al}_2\text{O}_3}$ or $V_{\text{final}} = V_{\text{Al}_2\text{O}_3} + V_{\text{glycerol}}$).
5. The coating is fully saturated and the maximum final packing volume fraction is obtained when the peak stress σ_{peak} is reached [55].

The experiments were carried out until the residual stress approached its final value (assumption 3). This is sufficient since the weight change was already below the small fluctuations of the balance a few minutes after point VI/vi. Glycerol with a boiling point of 290 °C will not evaporate in measurable amounts at 40 °C (assumption 1). For the cases with added water, small amounts of water may remain in the final film. The error induced by assumption 2 is below 0.6% due to the low secondary fluid volume fractions used in

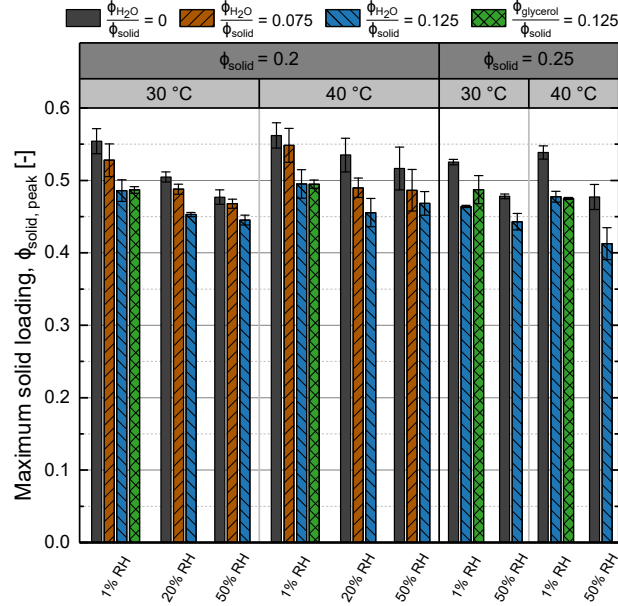


Figure 4.5: The average dry film particle volume fraction of the experiments obtained from the particle volume fraction at the peaks for the aforementioned formulations and drying conditions.

capillary suspensions. In a previous study with dyed 1-heptanol, we found that the film is saturated until the peak stress had occurred (assumption 5) [90]. These assumptions allow to calculate the final packing volume fraction $\phi_{\text{solid,peak}}$ as follows:

$$\text{Water : } \phi_{\text{solid,peak}} = \frac{V_{\text{Al}_2\text{O}_3}}{V_{\text{Al}_2\text{O}_3} + V_{\text{heptanol}}} \quad (4.4)$$

$$= \frac{\frac{m_{\text{final}}}{\rho_{\text{Al}_2\text{O}_3}}}{\frac{m_{\text{final}}}{\rho_{\text{Al}_2\text{O}_3}} + \frac{m(\sigma_{\text{peak}}) - m_{\text{final}}}{\rho_{\text{heptanol}}}} \quad (4.5)$$

$$\text{Glycerol : } \phi_{\text{solid,peak}} = \frac{V_{\text{Al}_2\text{O}_3}}{V_{\text{Al}_2\text{O}_3} + V_{\text{glycerol}} + V_{\text{heptanol}}} \quad (4.6)$$

$$= \frac{\frac{m_{\text{final}}}{\rho_{\text{Al}_2\text{O}_3} + 0.125\rho_{\text{glycerol}}}}{\frac{m_{\text{final}}}{\rho_{\text{Al}_2\text{O}_3} + 0.125\rho_{\text{glycerol}}} (1 + 0.125) + \frac{m(\sigma_{\text{peak}}) - m_{\text{final}}}{\rho_{\text{heptanol}}}} \quad (4.7)$$

with $m(\sigma_{\text{peak}})$ indicating the mass at the stress peak and $\phi_{\text{solid,peak}}$ denoting the final volume packing. Equation 4.5 is used for the samples with water, and Equation 4.7 shows the equation for the samples with glycerol. The factor of 0.125 arises from the initial volume fraction $\phi_{\text{glycerol}}/\phi_{\text{Al}_2\text{O}_3} = 0.125$ in these samples. The calculated particle volume fraction at the stress peak, $\phi_{\text{solid,peak}}$ of our experiments is shown in Figure 4.5. In general, we see a decrease in particle volume fraction at the stress peak $\phi_{\text{solid,peak}}$ with increasing water content. That is, inducing a flocculated particle network increases the porosity of the sample. As can be seen in Equation 4.1, an increase in pore size results in lower capillary stresses, which in turn leads to a lower peak stress for the same film height, or in other

words, a higher critical cracking thickness. This observation is in accordance with the findings of Guo and Lewis [55], and Singh et al. [121]. Singh et al. found that for a constant particle loading for alumina suspensions dispersed in water, the final packing volume of the coating decreased with increasing degree of flocculation, i.e. the film contained more pores [121]. Similarly, Guo and Lewis found the same decrease in dry film volume fraction for flocculation induced by salt addition to stabilized silica particles [55]. Additionally, their experiments indicated that an increase in initial particle volume fraction led to a larger dry film volume fraction, i.e. a more compact coating.

Increasing the relative humidity tends to slightly decrease the dry film particle volume fraction in the capillary suspensions. Interestingly, an increase in relative humidity also increases the dry film porosity (decreases $\phi_{\text{solid,peak}}$) of coatings prepared from the pure suspension, coatings that were not intentionally flocculated. This effect appears to be more evident at lower drying temperature. A temperature increase at the initial particle volume fraction of 0.2 results in a denser film at each ϕ_{sec} and relative humidity. This finding supports our hypothesis of larger particle and cluster mobility at 40 °C, which allows some stress relaxation through particle migration. Increasing the initial particle load to 0.25 causes a less dense film for both temperatures compared to the lower initial load, a result that is in accordance with the larger measured yield stress (higher degree of flocculation). The particle interactions suppress the particle mobility resulting in more porous films. This result is in contrast to the results of Guo and Lewis [55]. The discrepancy may arise from the use of partially stabilized silica particles versus unstabilized alumina, as well as the use here of irregularly shaped alumina particles.

The link between the film porosity and stress peak should be established for capillary suspensions in order to elucidate the stress reduction potential caused by the secondary capillary bridges rather than through a porosity increase. The samples with added water both show a decrease in σ_{peak} and $\phi_{\text{solid,peak}}$, as predicted. Recall that at lower initial solid load, there was no difference in peak stress with the capillary suspension ($\phi_{\text{H}_2\text{O}}/\phi_{\text{solid}} = 0.125$) and increasing relative humidity at either temperature (Figure 4.4b). Yet, when dried at 50% RH, the dry capillary suspension films are more porous (Figure 4.5). This is a first indication that a porosity increase does not significantly contribute to a peak stress reduction in capillary suspensions. The glycerol capillary suspension samples at 1% RH and both temperatures provide a clear answer. Both capillary suspensions with $\phi_{\text{sec}}/\phi_{\text{solid}} = 0.125$ show almost identical porosities, while they differ in peak stress. This clearly demonstrates that particle-particle interactions can dominate the influence on the peak stress as opposed to the porosity of the coating.

In this section, we have shown that capillary suspensions lead to more porous dry films than the pure suspension due to flocculation. However, increasing the relative humidity can also increase the porosity, in particular for the pure suspension. Moreover, we have demonstrated that the porosity increase in capillary suspensions are not responsible for the reduction in peak stress. Instead, the particle interactions caused by the secondary liquid capillary bridge determine the influence on the peak stress. This suggests that by choosing a secondary liquid with a higher boiling point than water and stronger interfacial tension than glycerol can further improve the formulation.

4.4.4 Residual saturation

The observed temperature dependence of the secondary liquid on the dry film porosity raises the question whether the capillary water bridges persist until after drying or if they evaporate earlier, as would be predicted by the higher vapor pressure. If the water bridges partially remain in the film, one would expect a larger residual fluid content and longer influence of the bridges on the drying dynamics. In order to detect these relatively low residual contents, a thermogravimetric analyzer with a resolution of 0.1 μg was used. The samples were dried into a dry nitrogen atmosphere and a similar wet film thickness in the crucible as on the cantilever, as described in [subsection 4.3.5](#). [Figure 4.6](#) shows the residual liquid in terms of the coating's liquid loading $m_{\text{liquid}}/m_{\text{dry}}$ ([Equation 4.3](#)) for films prepared with increasing water content at different initial solids load for both 30 °C and 40 °C. All experiments show a residual solvent loading lower than the initial water loading when formulating the samples (3.2 % for $\phi_{\text{H}_2\text{O}}/\phi_{\text{solid}} = 0.125$ at $\phi_{\text{solid}} = 0.2$), demonstrating that at least 80% of the water has evaporated. At an initial solid fraction of $\phi_{\text{solid}} = 0.2$, there is no difference in residual liquid loading for capillary suspensions when dried at 30 °C. At the higher temperature, both the pure suspension and weak capillary suspension show an increase in the residual fluid fraction, while the capillary suspension exhibits a lower saturation compared to 30 °C. At higher initial solid fraction, the results contrast to the lower particle fraction; while the residual liquid content for the pure suspension is at a lower level as for $\phi_{\text{solid}} = 0.2$, the capillary suspension displays a clear increase. This means that more residual fluid, presumably water, remains in the capillary suspension at $\phi_{\text{solid}} = 0.25$.

Comparing the residual liquid content ([Figure 4.6](#)) to measurements of the film porosity at 1% RH ([Figure 4.5](#)), we see that the film porosity increases with increasing water content, i.e. a stronger gel-network and thus more flocculated suspension. This in turn could lower diffusional resistances for vapor transport from within the coating to the outer surface,

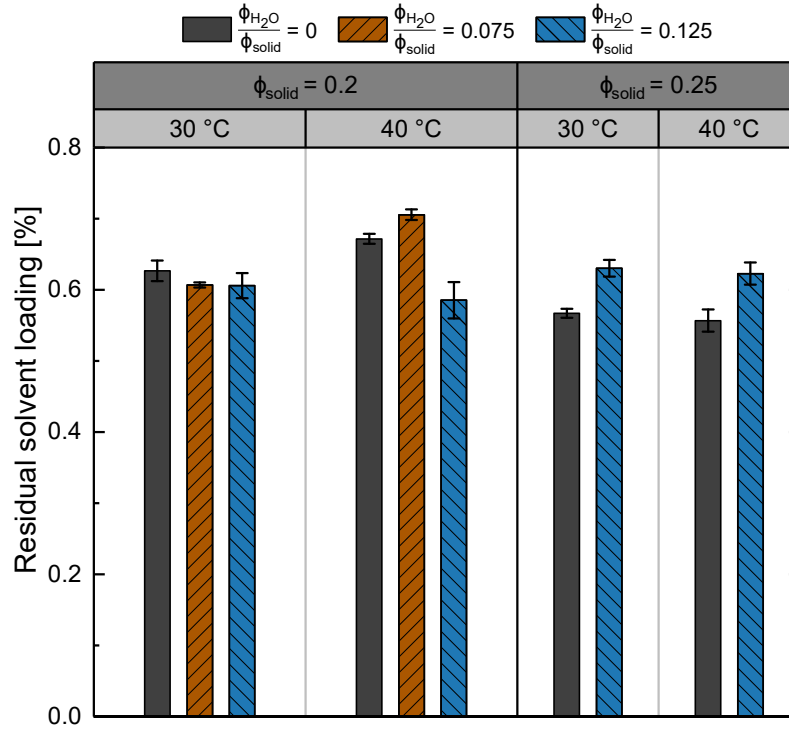


Figure 4.6: Residual solvent loading for differently formulated suspensions with increasing water content and initial particle load. The samples were dried at a constant temperature of 30 °C and 40 °C. Subsequent mass loss caused by heating was recorded with a thermogravimetric analyzer. The residual solvent loading is normalized against the dry particle weight.

leading to a lower film saturation. The residual fluid loading of the pure suspension closely correlates with the film porosity. An increase in temperature increases the diffusivity, which further enhances mass transport to the surface. However, the results for $\phi_{\text{solid}} = 0.25$ are in contrast to this theory. While the porosity of the capillary suspension films at higher initial solid fraction are somewhat higher, the retained amount of liquid also increased. Further insight can be provided by research using porous media, especially in oil recovery, where three phase flow phenomena are more common. When modeling the drying of a porous system, the rules of invasion percolation (IP) and drainage flow can be applied [103, 122]. Drying of the pure suspensions leads to phenomenon such as Haines jumps or meniscus snap-off (more dominant at imbibition conditions) [122, 123]. These incidents lead to isolated blobs of heptanol that are disconnected from the bulk. These droplets can remain trapped in the film as residual fluid. As mentioned in subsection 4.4.1 and shown in Figure 4.3, the water bridges, with a higher capillary pressure than heptanol, allows the capillary suspension film to dry at a constant rate even beyond close packing. The capillary bridges formed by the secondary liquid obstruct the bulk fluid pathways so that snap-off events are reduced or even prevented. Furthermore, heptanol covers the water bridges, even in the presence of air [110]. Thus, the bulk heptanol remains connected to a larger degree, leading to piston-like flow [123]. Continued drainage (drying) can even lead

to reconnections between previously disconnected oil clusters [124]. In a recent micro-CT study by Scanziani et al., drainage experiments with brine, oil, and gas showed that water is retained in the smallest necks and pores upon gas invasion in a porous carbonate rock [111]. Oil occupies the medium sized pores and gas preferentially invades the larger pores. In porous media filled with oil and water, an increase in temperature additionally favors water retention leading to preferential oil drainage [125, 126].

With this more complex behavior in mind, we can revisit the potential difference in structural particle arrangements for the capillary suspension at $\phi_{\text{solid}} = 0.25$ compared to $\phi_{\text{solid}} = 0.2$. For granular materials, the coordination number z should be related to the particle volume fraction by $z = \pi/(1 - \phi_{\text{solid}})$ [43]. Since the number and volume of capillary bridges are related through $\phi_{\text{sec}}/\phi_{\text{solid}} = z/2 \cdot V_{\text{bridge}}/V_{\text{particle}}$ the bridge volume must be similar for the higher particle fraction sample since the $\phi_{\text{sec}}/\phi_{\text{solid}}$ ratio remains constant [34, 127]. Of course, capillary suspensions are composed of dense flocs connected by a sparse backbone [37] where the porosity of these networks is only weakly related to the particle fraction [45]. In accordance with the porous rock/ particle bed findings, this would lead to more residual liquid stemming from the similar capillary water bridges. The increase in the number of connections would explain the observed increase in yield stress, smaller peak stresses, similar porosity, and larger residual fluid content compared to the respective capillary suspension sample at lower initial particle load.

We conclude that the residual fluid content for the pure suspension is mainly dependent on the porosity of the final dry film. For the capillary suspension on the other hand, it appears to be an interplay of porosity and number of capillary water bridges. Blockage of pathways for air invasion leads to better drying of heptanol even fortified at elevated temperatures. This suggests that residual liquid in capillary suspensions is predominantly water. The extent should be controlled by the total amount of water bridges present in the sample. The following section will therefore examine if capillary water bridges despite its higher vapor pressure persist longer than heptanol.

4.4.5 Capillary bridge evaporation

In the previous section, we put forward a hypothesis that the water capillary bridges persist through the late stages of drying. In order to directly elucidate the evaporation behavior of the capillary water bridges, we coupled a mass spectrometer (MS) with thermogravimetric analysis (TGA), as shown in Figure 4.7. This combination allows us to set an accurate temperature, while obtaining the drying rate and analyzing the headspace composition. The temperature for these measurements followed the profile shown in Table 4.2 where

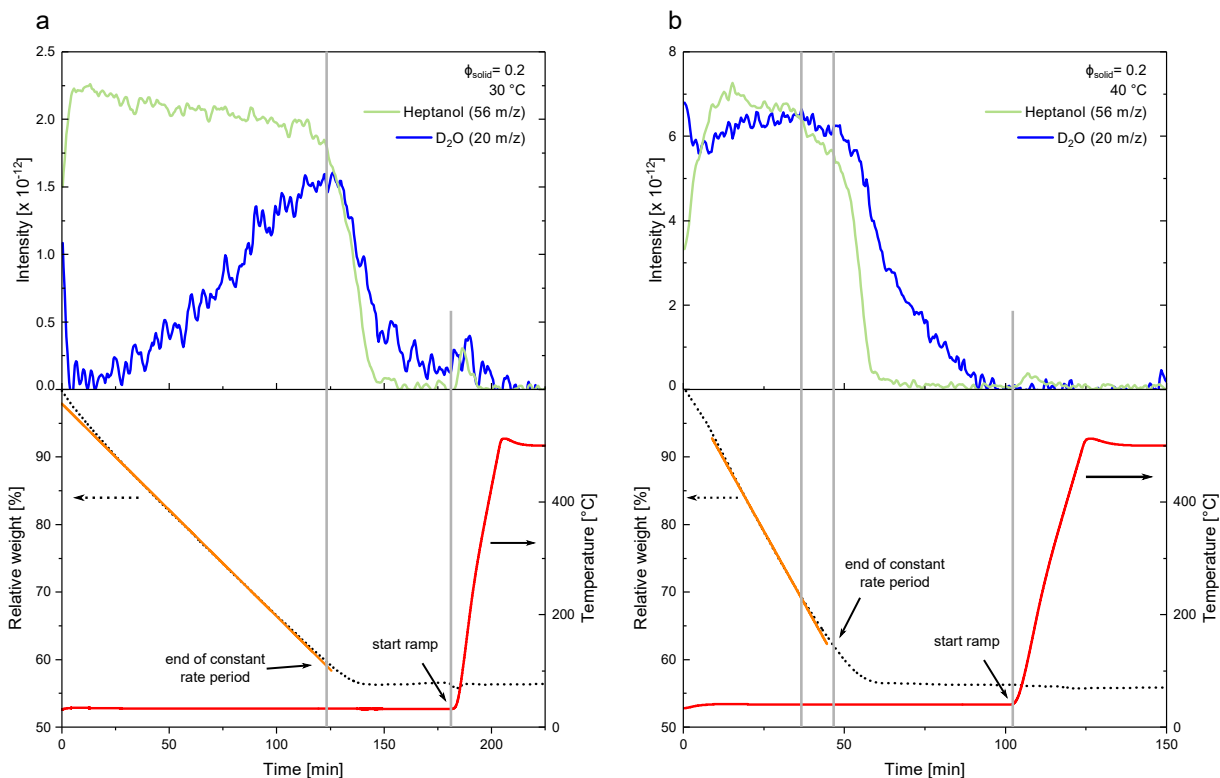


Figure 4.7: Results for thermogravimetical analysis coupled with mass spectrometry over time for drying of capillary suspensions with initial volumetric particle load of 0.2 and dried at (a) 30 °C and (b) 40 °C. The upper panel illustrates the intensity of the heptanol measured at a specific mass to charge ratio of 56 m/z (green line) and the intensity of the heavy water mass at 20 m/z (blue line). The lower panel shows the temperature profile (red line) and the relative weight change of the coating (dotted black line).

the sample was first dried at either 30 °C (Figure 4.7a) or 40 °C (Figure 4.7b) then, once the sample mass remained constant, increased to 500 °C. Since 1-heptanol (56 m/z) also has a fractional mass peak overlapping with water, we replaced water with D₂O (20 m/z). Despite flushing, we observed a constant decrease for the 20 m/z signal, the indicator for heavy water, even during the temperature increase to 500 °C. As this is highly unlikely to be D₂O, we hypothesize that the argon, which is also present in trace amounts and also possesses a fractional peak at 20 m/z, could be the reason for the constant decline in that signal. Therefore, we used the linear decrease after attaining a temperature of 500 °C as a baseline for correction in the D₂O signal. Subsequently, the MS signals were smoothed. Figure 4.7 shows the results for capillary suspensions at an initial solid load of 0.2 and $\phi_{\text{H}_2\text{O}}/\phi_{\text{solid}} = 0.125$ at the two temperatures. The green solid line represents the 56 m/z intensity over time for heptanol and the blue solid line shows the intensity of the 20 m/z signal detected for heavy water. After the start of the experiment for drying of the capillary suspension at 30 °C (Figure 4.7a), 1-heptanol constantly evaporates until the end of the constant rate period denoting the transition to the second drying period in which the headspace concentration drastically drops. When the film appears gravimetrically dry,

the heptanol in the gas phase swiftly decreases. Once the temperature is rapidly increased, the small amount of residual heptanol evaporates.

The evaporation of heavy water from the film is quite different. Over the course of the constant rate period, the gas phase concentration of D₂O continually increases. In fact, it is still increasing at the end of the constant rate period when the heptanol concentration starts to decrease. Once the heavy water concentration starts to decline, the rate of decrease is smaller than for the heptanol. Furthermore, water is still found in the gas phase well after the film appears to be dry (mass reaches a constant value) and the temperature increase evaporates the leftover water. This clearly shows that at 30 °C, the capillary bridges dry much slower than heptanol despite the higher bulk vapor pressure. More importantly, the capillary bridges persist and are still drying when heptanol has already reached its equilibrium.

The drying of the capillary suspension at 40 °C is shown in [Figure 4.7b](#). As with the drying at 30 °C, heptanol dries with a fairly constant rate, although there is more gradual decrease before the end of the constant rate period. Due to the high sensitivity of the MS, the reason for this earlier drop could be inhomogeneities in coating thickness. This is also reflected in the [TGA](#) measurement where a rate change is observed in the film weight. Nevertheless, a sharp decrease is observed after entering the second drying period. Again, the water concentration drop is delayed by several minutes, once again occurring when the film has nearly reached its dry state. Surprisingly, this delay is longer at the higher temperature, supporting the results obtained from drainage experiments [[125](#), [126](#)]. When the heptanol concentration in the gas phase is approximately zero, the water still has a high concentration in the gas phase. This concentration decays slowly, only reaching zero just before the temperature increase. Upon heating, the trapped heptanol evaporates, but water is not detected. This suggests that while persisting longer at elevated temperature, the water has completely evaporated before the temperature rise.

These results show that the capillary bridges, despite being formed of water with a much lower boiling point than 1-heptanol, persist for long times during drying. While the cause for this delay should be determined, it does prove that even secondary fluids with a higher vapor pressure can persist in capillary suspension networks. The full potential will only be realized by replacing water with higher boiling point wetting liquids, such as glycerol, to delay or even prevent bridge evaporation. The lower interfacial tension of glycerol, however, tempers this potential. Thus, liquid combinations with high interfacial tension in addition to the desired high boiling point must be sought. One way of tailoring the heptanol-water system used in this study is by adding salt to the water. This decreases the vapor pressure and even increases the interfacial tension at the same time [[128](#)].

The present research also points to a few unanswered questions. First, why a difference between the evaporation dynamics is observed in the D_2O between 30 °C and 40 °C (Figure 4.7)? While the rate of the evaporation for the heptanol remains unchanged, the evaporation rate for the D_2O appears to be constant in time at the higher temperature whereas it increases with time at the lowest temperature. We hypothesize that the difference may arise due to the small, but finite solubility of the D_2O in the heptanol. Thus, the change may be due to a varying miscibility of D_2O in heptanol. While the air-liquid interface at the surface may be depleted of D_2O at 30 °C, the D_2O at the air-liquid interface is being constantly and more rapidly replenished from the bulk liquid at 40 °C. This is caused by the larger solubility and thus concentration close to the capillary bridges, leading to a larger gradient. Additionally, mass transport is increased due the higher temperature. The influence of particle size on the present results is also of interest. Previous research has shown that the yield stress depends on the reciprocal radius [10]. The structure of these systems, however, will differ networks created with larger particles having a higher fractal dimension [37]. This also changes the average size of the flocs (relative to the particle size) and the strength of the inter-floc links. The particle size also has clear implication to the drying of these suspensions. The particle size will change the capillary pressure (again, with a reciprocal dependence). Would this change be balanced by the change in the yield stress? There is also a change in the particle (or floc) mobility. Thus, the dependence of the particle size on the stress and structure of these drying capillary suspensions may be very interesting for further research.

4.5 Conclusions

In this paper, we investigated effects accompanying the drying of suspensions with and without capillary interactions. Enhancing a pure, oil-based suspension with only a few drops of water induces a network, transforming the suspension into an elastic paste. During drying, stresses caused by the capillary pressure within pores arise that are opposed by the water bridges in the capillary suspensions. Therefore, we simultaneously measured the evolving stresses and compared them with the drying rate. The capillary suspensions exhibit a faster stress rise, an indication of more uniform drying, and have lower peak and residual stresses. The peak stress decreases with increasing amounts of water, such that films formed from capillary suspensions are less prone to cracking. Additionally, we found that drying into more humid air enhances the stress reduction, even for the pure suspension. An increased film porosity, caused by capillary suspension networks, are only minor contributions to the observed stress reduction. Moreover, with reduced particle

migration during drying, for example at higher initial solid loads, capillary suspensions show a greater potential. Lastly, we have shown that the capillary water bridges, despite having a lower bulk boiling point, persist into late stages of drying, after the heptanol has mostly evaporated. The partial evaporation of capillary bridges during drying is different at the two temperatures examined, which should be investigated further as well as the reason for the persistence of the bridges. Tuning the suspension with a higher boiling point secondary liquid can further this potential. In summary, the drying of capillary suspensions is a complex interplay between three phase flow, interfacial tension, capillary pressure dependencies, vapor pressure and the resulting yield strength. Understanding this interplay will help us tune the drying behavior for the desired applications.

Acknowledgements

The authors would like to thank Almatris GmbH for the donation of alumina particles. Additionally, we thank Prof. Rob Ameloot and Dr. Min Tu for access and help with the mass spectrometry measurements at the KU Leuven Centre for Membrane Separations, Adsorption, Catalysis, and Spectroscopy for Sustainable Solutions (cMACS), Belgium. Finally, we acknowledge financial support from the German Research Foundation, DFG under project number KO 4805/2-1 and the Research Foundation Flanders (FWO) Odysseus Program (grant agreement no. G0H9518N).

Conflicts of interest

The authors declare no conflicts of interests

5 Capillary bridge formation at room temperature in binary liquids with small miscibility

Full title: Capillary bridge formation at room temperature in binary liquids with small miscibility [129].

Authors: Steffen B. Fischer, Erin Koos

Status: published

Bibliographic data: *Colloid Interface Sci. Commun.* 41:100373, 2021.
doi: <https://doi.org/10.1016/j.colcom.2021.100373>

Authors can use their articles, in full or in part, for a wide range of scholarly, non-commercial purposes: Inclusion in a thesis or dissertation (provided that this is not to be published commercially).

www.elsevier.com/about/policies/copyright.

The article has been adapted in this thesis to reflect the numbering of references and citations in accordance with the manuscript.

5.1 Abstract

Capillary suspensions, solid-liquid-liquid systems, are conventionally formulated by dispersing the particles in the bulk phase and then adding a small amount of secondary liquid (< 5 vol%), leading to increased yield stress. Previous work has shown that partially miscible liquids form capillary bridges between particles upon temperature induced phase separation. In this work, we show that capillary suspensions can be formed by mixing particles with partially saturated 1-alkanol (6-8 carbon atoms)/water solutions, without the need for a temperature induced phase separation. Moreover, we show this effect works with different particle sizes and geometries. In addition, we illustrate that a pure suspension formed with 1-alkanols can create capillary suspensions when stored in humid conditions. This paper also demonstrates how partially miscible oil suspensions form

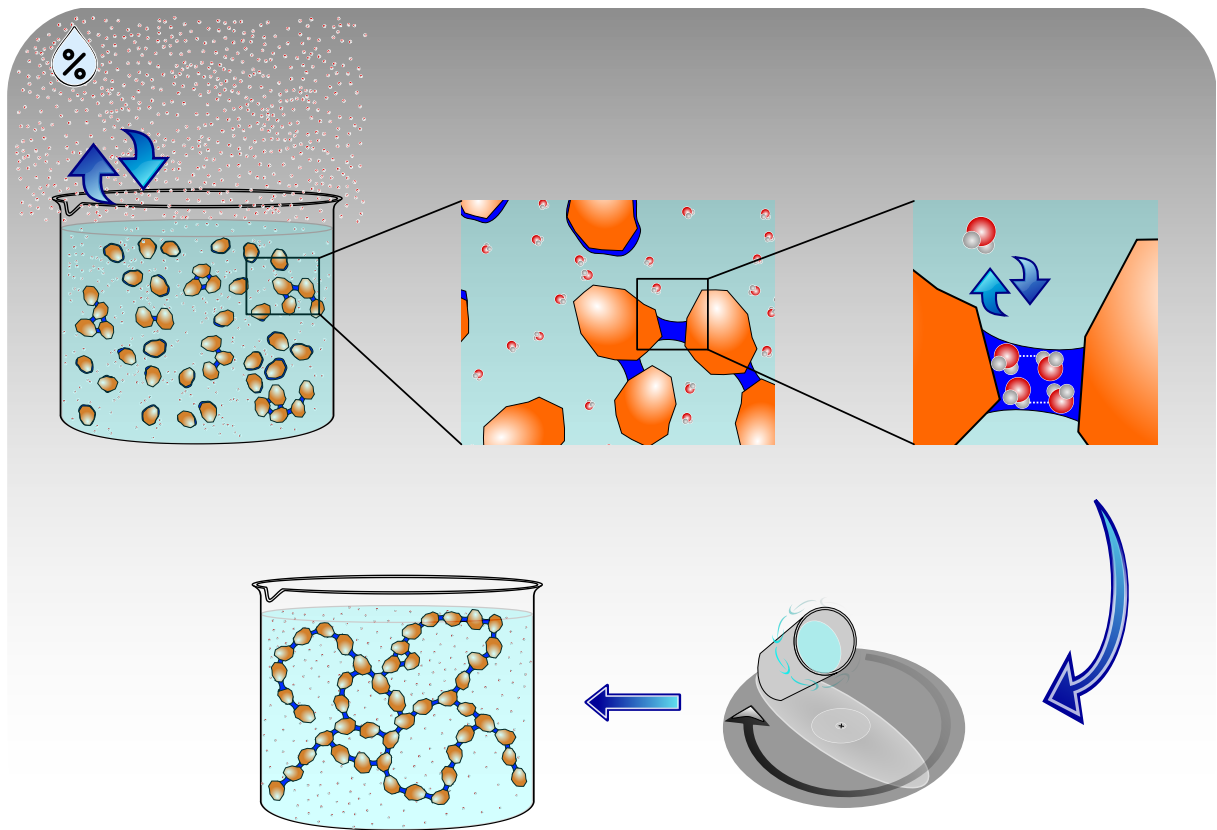


Figure 5.1: Graphical abstract to “capillary bridge formation at room temperature in binary liquids with small miscibility”.

capillary bridges even during the drying process when exposed to high humidity. This can lead to a significant decrease in drying stresses but also a change in structure.

5.2 Introduction

Capillary bridge formation is a generally well-known phenomenon in wet granular matter [43, 130–132]. The most prominent example of the capillary bridging effect can be observed when building sand castles [44]. Water forms pendular rings between the sand particles leading to meniscus formation with a lower pressure in the liquid. This negative pressure acts on the particles with the attractive capillary force, which is much stronger than van der Waals interactions [133]. This allows sturdy structures, such as sand castles, to be constructed simply by wetting the particles. Industrially relevant examples are agglomeration and granulation of powdered materials to form pharmaceutical tablets or prevent dust inhalation [130, 134]. Besides these methods for deliberately forming capillary bridges, there is also another effect called capillary condensation. It describes the self-induced formation of a liquid meniscus in humid air. When the particles are

sufficiently close, water vapor condenses and forms capillary bridges as described by the Kelvin equation [42]. The network formed thereby can lead to undesired agglomeration and clumping of the otherwise freely flowing powder, especially in hygroscopic materials.

Similarly, Bloomquist and Shutt found that the sedimentation volume in dilute suspensions increased upon addition of water to organic liquids, which was attributed to flocculation [135]. More recently, Koos and Willenbacher showed that the addition of a small amount of liquid immiscible with the bulk liquid in a suspension, can cause a dramatic change of rheological properties from a liquid like to a gel-like state at particle volume fractions of only 10% [9]. This behavior was observed for systems where the added liquid did wet the particles (pendular state), as well as when it did not preferentially wet the particles (capillary state). The strength (yield stress and shear modulus) of the resulting sample spanning network (Equation 5.1) is dependent on the capillary force and can be described as a function of the particle volume fraction $f(\phi_{\text{solid}})$, a function $g(V_{\text{sec}}, s)$ with the volume of the bridge V_{sec} , the distance between the particles s , as well as the contact angle θ , the particle radius r , and the interfacial tension γ [34, 47, 127, 136]:

$$\sigma_y = f(\phi_{\text{solid}})g(V_{\text{sec}}, s)\frac{\gamma \cos \theta}{r} \quad (5.1)$$

Therefore, the yield stress of capillary suspensions is altered by the material properties (particle size, interfacial tension and wetting angle) as well as the the factors influencing the bridge sizes and network structure. Since there is a feedback between the droplet breakup and coalescence with the local flow field, V_{sec} depends on the ratio of the secondary liquid volume fraction ϕ_{sec} to the solid volume fraction ϕ_{solid} as well as the mixing conditions and network structure [36, 53, 127, 137]. Typically, capillary suspensions in the pendular state exhibit a peak in the yield stress with increasing amounts of added secondary fluid [37]. At low secondary volume fractions, the network is formed through pendular bridges that coalesce into trimers and larger flocs as the amount of secondary liquid is increased [127, 138]. This transition is accompanied by a decreasing dependence of the network strength on the added liquid fractions. Adding sufficient liquid results in the formation of dense flocs with few connections reducing the yield stress [53, 136, 139]. Since these suspensions form sample-spanning networks and the bridges rupture with external shear [140], capillary suspensions exhibit shear-thinning behavior, which allows easy spreading under shear [10, 138]. These unique properties make the capillary suspension concept a versatile tool for application in: low fat foods [47, 48, 141], lithium-ion battery electrode material [93], macroporous ceramics [45, 51, 113], printed electronics [11, 50], and smart-tunable materials [142, 143]. It was also found to reduce stresses and cracking during

drying [8, 85], as well as reduce drying defects such as pinholes and trench formation caused by lateral drying [90].

All the previously mentioned applications used the same principle steps to create the capillary suspension in the pendular state. At first, the particles are suspended in the bulk liquid, then the small amount of the bulk immiscible fluid is added and thoroughly mixed. Typically, these two fluids are immiscible or, if there is a small partial miscibility, it is assumed to have no influence on the resulting structure. However, another method of inducing capillary bridge formation was shown by Gogelein et al. [12]. They made use of the temperature dependence of the miscibility gap in partially miscible fluids. Their investigated model system was special in that they chose a water-2,6 lutidine mixture that undergoes phase separation upon heating, while most systems exhibit better miscibility at elevated temperature. When they increased the temperature, a suspension of glass spheres dispersed in a water lutidine mixture displayed capillary bridge formation in a monolayer. The application of this concept to capillary suspensions was hypothesized by Koos [34]. In this paper, we investigate the implications of partially miscible liquids on the capillary suspension phenomenon for the pendular state. We compare the yield stress of suspensions formulated with different particle sizes and shapes in partially miscible 1-alkanol/water mixtures. The conventional way of creating a capillary suspension by addition of water to 1-alkanol suspensions is compared with adding particles to 1-alkanol/water solution as well as a pure suspension stored under high humidity conditions.

5.3 Materials and Methods

5.3.1 Materials

Suspensions were prepared with three different particle types as listed in [Table 5.1](#).

Table 5.1: Capillary suspension formulation parameters for directly added water (conventional formulation) and water content measured in solution (solution formulation). The water content in the solution formulation method also includes any dissolved water from the 1-alkanol solvents.

Particle	$d_{50,3}$ [μm]	Shape	ϕ_{solid} [vol%]	Conventional	$\phi_{\text{Solution H}_2\text{O}}$ [vol%]		
				$\phi_{\text{H}_2\text{O}}$ [vol%]	1-hexanol	1-heptanol	1-octanol
Al_2O_3	0.5	irregular	20	0	0.89 ± 0.01	0.06 ± 0.01	0.14 ± 0.01
Al_2O_3	0.5	irregular	20	3	2.40 ± 0.01	2.39 ± 0.02	2.55 ± 0.02
Glass	3.0	spherical	20	0	0.89 ± 0.01	0.06 ± 0.01	0.14 ± 0.01
Glass	3.0	spherical	20	3	2.40 ± 0.01	2.39 ± 0.02	2.55 ± 0.02
TiO_2	0.39	nano-aggregate	4	0	1.07 ± 0.01	0.07 ± 0.01	0.17 ± 0.01
TiO_2	0.39	nano-aggregate	4	5	4.76 ± 0.05	4.25 ± 0.15	3.76 ± 0.03

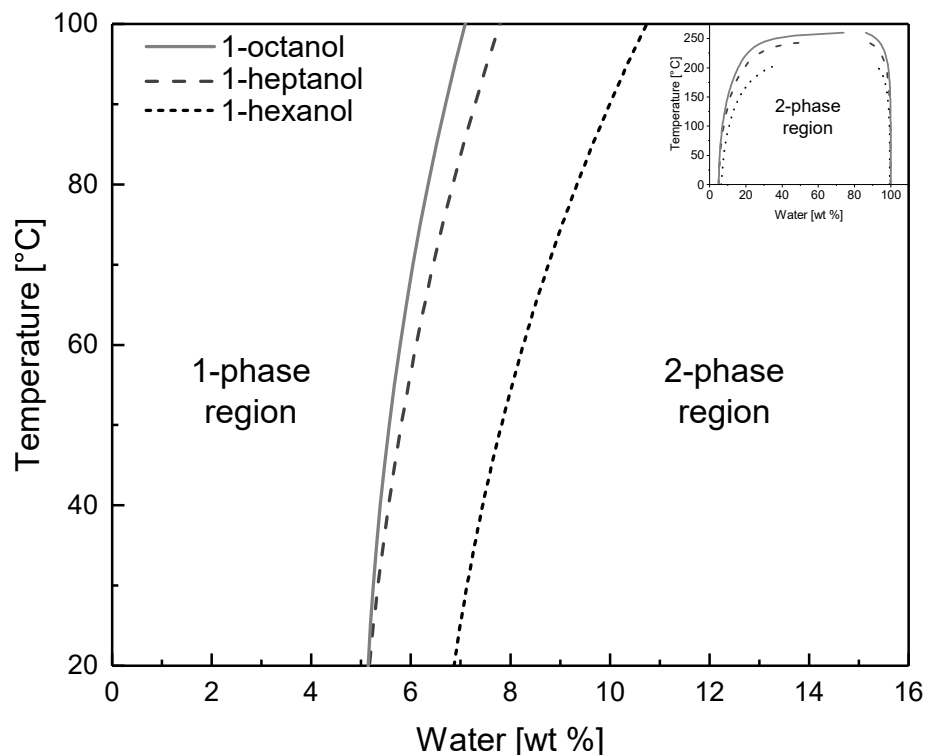


Figure 5.2: Approximated temperature dependence of mutual solubilities of 1-alkanols and water in terms of wt%. The inset shows the two phase region up to temperatures approaching the critical point. (Due to insufficient availability of experimental data at higher temperatures, the correlations used from the references do not allow the calculation of a closed 2-phase region.) While 1-alkanols are barely miscible in water, water miscibility in 1-alkanols increases with decreasing chain length. Data calculated from Maczynski et al. [144, 145, 146]

Alumina particles (α -Al₂O₃, CT3000SG, Almatis GmbH, Germany) possess an irregular shape and average particle size of $d_{50,3} = 0.5 \mu\text{m}$ according to the supplier. Spherical glass beads (OMicron NP3-P0) with a smooth surface and particle diameter of $d_{50,3} = 3 \mu\text{m}$ were provided by Sovitec in Belgium. Fumed titanium dioxide (Aeroxid P25) comprises irregular aggregates with a size of $d_{50,3} = 0.39 \mu\text{m}$ (primary particle size of $d_{50,3} = 0.021 \mu\text{m}$) and was produced by Evonik, Germany. The particles were suspended in 1-hexanol (> 98%, Acros Organics, Belgium), 1-heptanol (> 99%, Alfa Aesar), and 1-octanol (> 99%, Emplura, Merck Millipore, Germany). These liquids form slightly miscible solutions with water depending on the temperature. Their temperature dependent miscibility gap, illustrated as a function of the water content expressed in weight percent is shown in Figure 5.2. The miscibility gap is a mutual property, that is, 1-alkanol can dissolve in water and water is also dissolved in 1-alkanol. While these 1-alkanols barely dissolve in water at higher temperature (Figure 5.2 inset), several weight percent of water can dissolve into 1-alkanols, even at room temperature. The two-phase region calculated by a fitted function, taken from Maczynski et al. [144, 145, 146], is not closed since no experimental data was available to verify the fitted function. The amount of water in the “pure” solvents, as well as the

1-alkanol samples with dissolved water, was measured using Karl Fischer titration by means of a weight fraction and subsequently converted to volume fraction assuming an ideal mixture. This is justified due to the small amounts of dissolved water investigated in this work.

5.3.2 Sample preparation

To remove residual moisture, all particles were oven dried overnight at 100 °C and subsequently cooled and stored in a desiccator. Pure suspensions were formed by adding the particles to each of the liquid such that a particle volume fraction of $\phi_{\text{solid}} = 0.2$ was obtained for Al₂O₃ and NP3, and a solids load of $\phi_{\text{solid}} = 0.04$ for TiO₂. Subsequently, the suspension was mixed using two periods of two minutes at 3500 rpm in a Speedmixer DAC 150.1 FV (Hauschild & Co. KG, Germany) and designated 25 ml polypropylene cups ($\varnothing = 35$ mm).

In order to obtain conventionally formulated capillary suspensions, as shown in [Figure 5.3a](#), ultra-pure water (atrium 611 DI, Sartorius AG, Germany) was added with a micropipette to achieve water volume fractions of $\phi_{\text{H}_2\text{O}} = 0.03$ for Al₂O₃ and NP3, while adding $\phi_{\text{H}_2\text{O}} = 0.05$ to the TiO₂ samples. Afterwards, the suspensions were mixed for three more periods of two minutes to obtain smooth samples. [Table 5.1](#) summarizes the formulation parameters for conventionally formulated capillary suspensions. For another suspension preparation technique depicted in [Figure 5.3b](#), 1-alkanol/ water stock solutions were prepared (water dissolution formulation). Ultra-pure water was pipetted to achieve stock solutions with 3 vol% and 5 vol% water. The bottles were closed and sealed with Parafilm and mixed with a magnetic stirrer overnight. Afterwards the solution was given 24 hours to equilibrate without stirring at 20 °C. The water content of the equilibrated 1-alkanol solutions was then determined by coulometric Karl-Fischer titration, as shown in [Table 5.1](#).

Subsequently, the desired volume of 1-alkanol/water solution was pipetted into a cup and the respective amount of particles added. Consecutively, the suspensions were mixed according to the previously described multi-step Speedmixer method to limit heating of the sample. The third preparation technique used storage in a humid environment for various periods of time ([Figure 5.3c](#)). After the yield stress measurement of the pure ($\phi_{\text{H}_2\text{O}} = 0$) suspension samples, the cups were left open and stored in a sealed chamber with approximately 18 liter gas volume and nearly 100% relative humidity. The small gas volume along with the high boiling point (≤ 150 °C) of the 1-alkanols used ensures

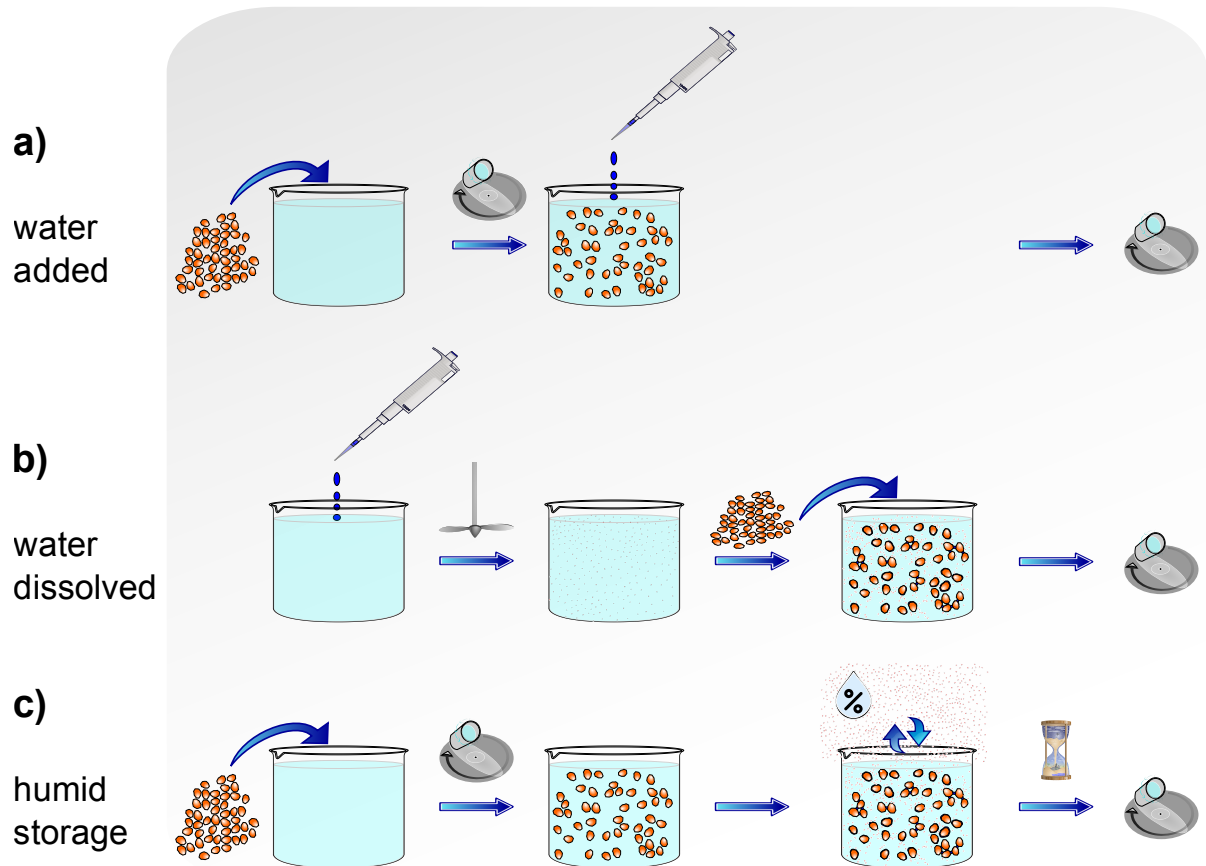


Figure 5.3: Overview of the capillary suspension preparation techniques used here. **(a)** In the conventional technique, particles are dispersed in the bulk liquid. Subsequently, water, the secondary liquid, is added via pipetting, followed by mixing the sample. **(b)** In the second capillary suspension preparation method, water is first dissolved in the bulk liquid and particles are added afterwards. **(c)** In the third preparation method, particles suspended in the bulk liquid are stored in a humid environment for a various period of time, followed by thorough mixing.

minimum evaporation of the bulk fluid during storage in the sealed chamber. These samples were measured again after 10 hours and 150 hours.

5.3.3 Yield stress measurements

A typical feature of capillary suspensions is a drastically increased yield stress compared to the pure suspension. This property is easily accessible by rheological measurements using a cup and vane setup. All samples were mixed in the Speedmixer at 3500 rpm in two minute increments until a smooth sample was obtained. The samples were remixed to allow a comparison of the yield stress unbiased by settling, aging and other temporal effects, especially for samples that were stored for 150 hours. Subsequently, the entire mixing cup filled with the sample is placed in a modified cup holder of a MCR 702 rheometer (Anton Paar GmbH, Germany). After lowering the vane into the cup, the sample was allowed to

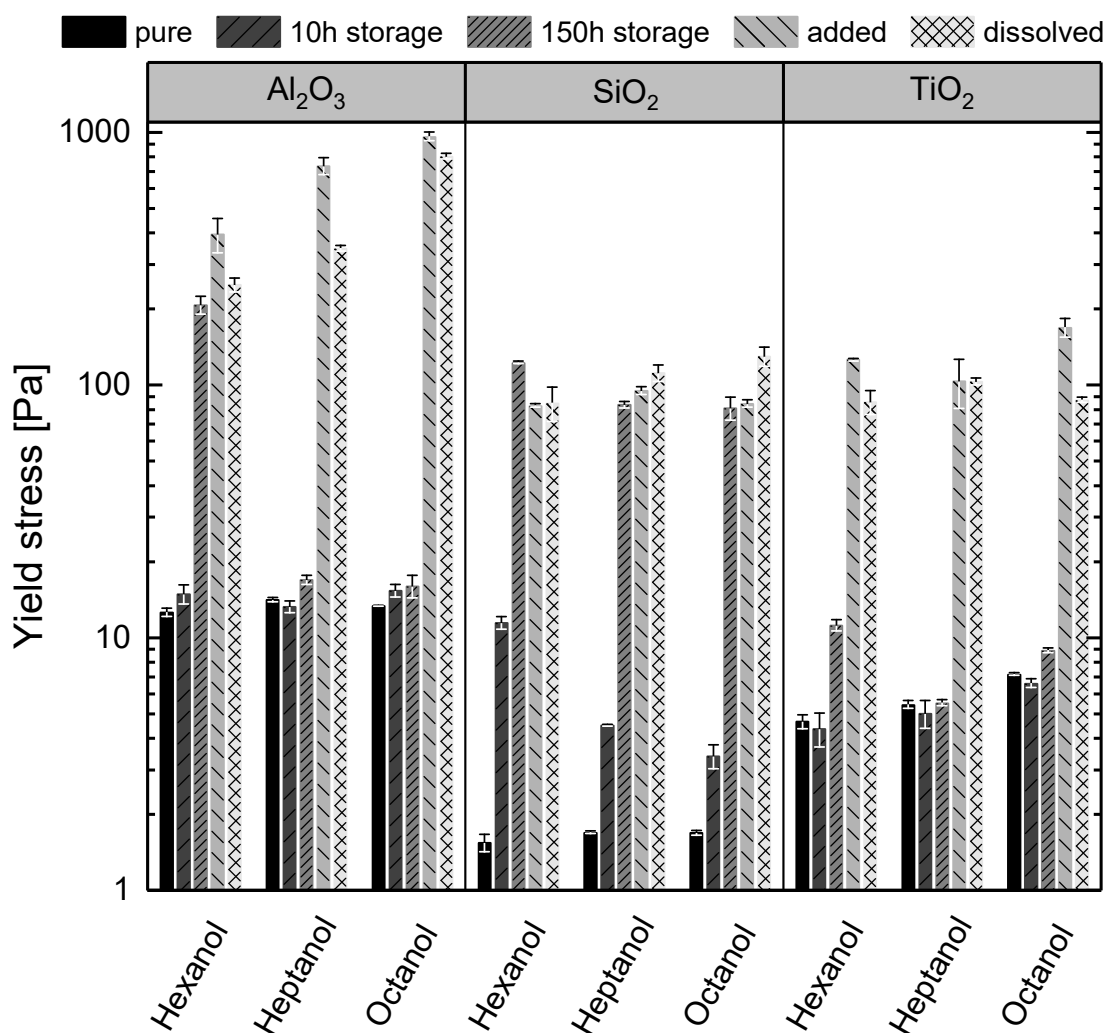


Figure 5.4: Yield stress of samples prepared from different particle materials. The left segment shows results for irregular shaped Al_2O_3 , the middle segment depicts spherical glass beads ($\text{SiO}_2/\text{NP3}$), and the segment on the right displays aggregated nanoparticle structure. Each particle system was dispersed in the major phase of 1-hexanol, 1-heptanol, and 1-octanol. Different methods of water addition was employed as described in the legend on top of the graph.

rest for five minutes to relax any induced stresses. Afterwards, a stress ramp was applied until large strains occurred. The resulting strain vs. stress curve was then analyzed with the tangent method to obtain the apparent yield stress of the sample.

5.4 Results and discussion

5.4.1 Yield stress comparison with different formulation routes

An overview of yield stress measurements from differently prepared solutions is presented in [Figure 5.4](#). The graph is divided in three segments corresponding to the particles used for suspension formation. Within each segment, there are subgroups for the three bulk fluids

Table 5.2: Calculated Hamaker constants according to Equation 5.2 [147] with required values taken from Butt and Kappl, Franz and Butt [147, 148].

Substance	A_{131} [J]		
	1-hexanol	1-heptanol	1-octanol
Al_2O_3	$2.68 \cdot 10^{-20}$	$2.56 \cdot 10^{-20}$	$2.48 \cdot 10^{-20}$
SiO_2 (amorph)	$1.38 \cdot 10^{-21}$	$1.12 \cdot 10^{-21}$	$8.83 \cdot 10^{-22}$
TiO_2	$1.37 \cdot 10^{-19}$	$1.35 \cdot 10^{-19}$	$1.34 \cdot 10^{-19}$

(1-hexanol, 1-heptanol, and 1-octanol). Each subgroup consists of a column representing the different formulation techniques. The solid black column represents a pure suspension with dried particles suspended in 1-alkanol. Recall that the particle volume fraction of Al_2O_3 and NP3 is $\phi_{\text{solid}} = 0.2$, while TiO_2 was prepared with $\phi_{\text{solid}} = 0.04$. We can see that for the Al_2O_3 suspension, there is basically no difference in yield stress when changing the bulk fluid. The measured yield stress likely results from van der Waals forces in these systems. Spherical glass beads (NP3) exhibit a much weaker network formation that is readily overcome by the particle weight, with no dependence on the fluid. The interaction potential between two identical particles (material 1) in a fluid (material 3) is proportional to the Hamaker constant A_{131} and can be calculated according to the following equation taken from Franz and Butt [147].

$$A_{131} = \frac{3}{4}k_B T \left(\frac{\epsilon_1 - \epsilon_2}{\epsilon_1 + \epsilon_3} \right)^2 + \frac{3h\bar{\nu}_e}{8\sqrt{2}} \frac{(n_1^2 - n_3^2)^2}{2(n_1^2 + n_3^2)^{\frac{3}{2}}} \quad (5.2)$$

with the Boltzmann constant k_B , the absolute temperature T in Kelvin, the substance's dielectric constant ϵ , the Planck constant h , the mean main electronic adsorption frequency $\bar{\nu}_e$, as well as the refractive index n of the material. The data and the Hamaker constant calculated according Equation 5.2 are listed in Table 5.2.

The lower yield stress for the glass systems without added fluid is likely due to the, at least, one order of magnitude lower Hamaker constant ($A \approx 1 \cdot 10^{-21}$ J) as shown in Table 5.2, as well as the larger particle size (see Table 5.1). TiO_2 shows a slightly stronger particle network compared to the glass (NP3) samples with the tendency to increase towards 1-octanol. This trend is possibly due to variation in the van der Waals forces (mostly the London dispersion forces), but the calculated Hamaker constant only varies by a few percent. This discrepancy may be caused by the induced change in dispersibility modifying the effective volume fraction for the small TiO_2 primary particles (20 nm).

Table 5.3: Mutual solubilities [vol%] of 1-alkanol ($C_nH_{2n+1}OH$) and water (H_2O) mixtures at 20 °C. Approximated, assuming ideal mixtures, from Maczynski et al. [144, 145, 146].

1-alkanol ($C_nH_{2n+1}OH$)	($C_nH_{2n+1}OH$) in (H_2O)	(H_2O) in ($C_nH_{2n+1}OH$)
1-hexanol (n = 6)	0.759	5.653
1-heptanol (n = 7)	0.207	4.263
1-octanol (n = 8)	0.057	3.843

With the addition of water (medium gray with lines from upper left to bottom right) to the Al_2O_3 system, one can see the typical dramatic increase in yield stress of nearly two orders of magnitude from the pure 1-octanol suspension to the capillary suspension. However, the yield stress decreases with decreasing carbon chain despite the same water volume fraction of $\phi_{H_2O} = 0.03$. Since the pure suspensions had nearly the same yield stress, the same amount of water was added, and the mixing conditions were the same, it is likely that some water is not contributing to the network formation, i.e. is not located in the capillary bridge. When scrutinizing the mutual solubilities of the 1-alkanol/water mixtures, Table 5.3, we clearly see a decrease in water solubility ((H_2O) in (1-alkanol)) from 1-hexanol to 1-octanol. In fact, all water added to form a capillary suspension could be dissolved in the 1-alkanols at 20 °C. Since the oil phase is the bulk phase and barely miscible in water, no significant effect is expected from the solubility of (1-alkanol) in (H_2O). The change of the interfacial tension, caused by dissolved water or a change in temperature, is expected to be marginal. In fact, Tian et al. measured the liquid-liquid interfacial tension of mutually saturated 1-alkanols and water at various temperatures, finding that the interfacial tension for hexanol, heptanol and octanol, measured at 298.2 K, increases with chain length from 6.44, 7.49 and 8.19 mN/m, respectively [149]. The largest change in interfacial tension over a range of 50 K was approximately 0.25 mN/m for hexanol, 0.53 mN/m for heptanol, and 1 mN/m for octanol. Thus, since the yield stress is proportional to the interfacial tension (Equation 5.1), the resulting change in yield stress is also expected to be marginal.

5.4.2 Residual water content

As described previously, the partial miscibility can be utilized to induce phase separation by changing the temperature of the two phase system. When we added particles to a solution of water dissolved in the 1-alkanol and stirred with a spatula, a large, coherent

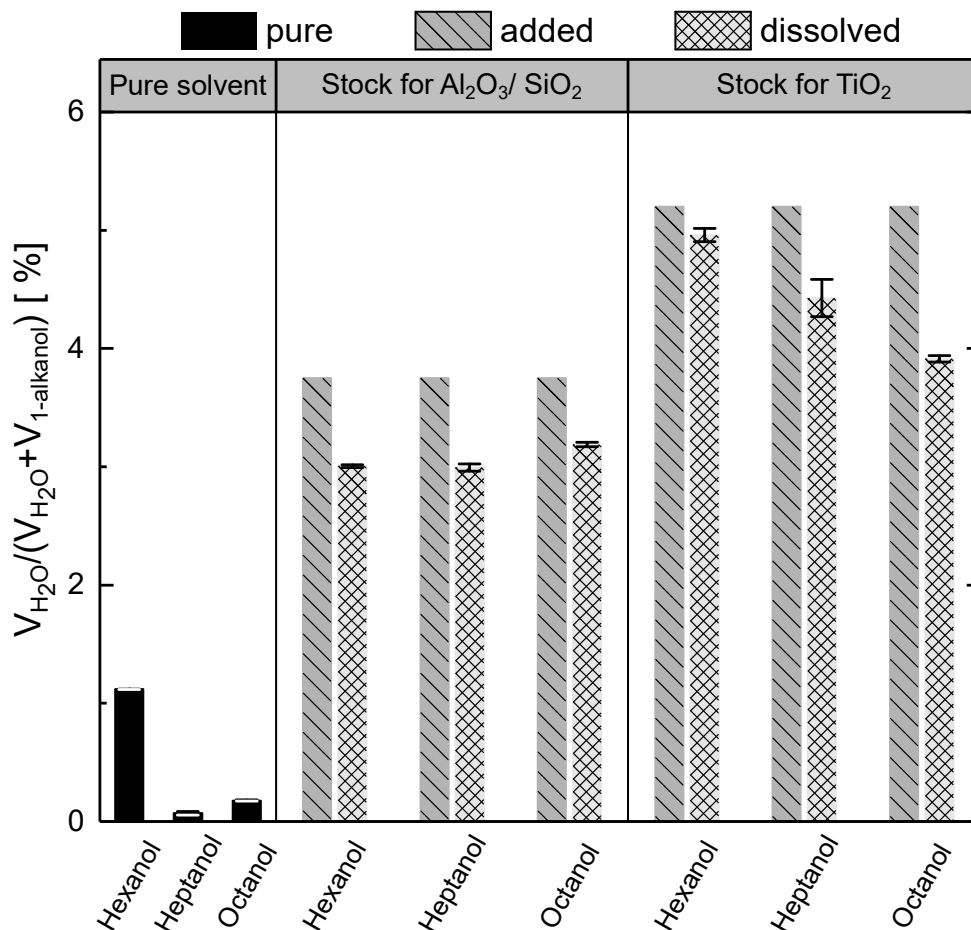


Figure 5.5: Water content ($V_{\text{H}_2\text{O}}/(V_{\text{H}_2\text{O}} + V_{1\text{-alkanol}})$) of the 1-alkanol stock solutions as determined by coulometric Karl Fischer titration (assuming ideal mixtures), used to prepare the suspensions. For Al₂O₃ and glass particles, the same stock solution was used. For TiO₂ larger amounts of water were added. The medium gray bar is shown for comparison with a fixed amount of water added to the suspension and therefore does not have error bars.

particle agglomerate formed. The true water content dissolved in each solvent, measured using Karl Fischer titration, is shown in [Figure 5.5](#).

This is homogenized using high shear mixing to form a high yield stress paste without the need for changing the temperature. Results are shown in light gray with a hatched pattern in [Figure 5.4](#). The yield stress for all pastes with alumina and 1-alkanol/water solutions show a significantly increased network strength compared to the suspensions prepared with pure bulk liquid (black bars). Again, we see a decrease in yield stress from octanol to hexanol, a result that follows the increasing water solubility. This observation strongly suggests that some of the water remains dissolved in 1-alkanol, proportional to its capability to dissolve more water. Put another way, while some of the dissolved water separates into capillary bridges upon the addition of the particles, an amount dependent on the relative solubility remains in solution.

The formation of water menisci between hydrophilic particles in a partially miscible system dominated by the 1-alkanol is governed by the generalized Kelvin equation [42]:

$$RT \cdot \ln \frac{c_{\text{H}_2\text{O}}}{c_{\text{H}_2\text{O}}^0} = \gamma V_m^{\text{H}_2\text{O}} \left(\frac{1}{r_1} + \frac{1}{r_2} \right) \quad (5.3)$$

where the gas constant and temperature are given by R and T , respectively. The concentration of water in 1-alkanol is given by $c_{\text{H}_2\text{O}}$, and $c_{\text{H}_2\text{O}}^0$ is the saturation concentration at standard conditions. The molar volume $V_m^{\text{H}_2\text{O}}$ for water at standard pressure and 20 °C is $1.8 \cdot 10^{-5} \text{ m}^3/\text{mol}$. The capillary bridge will have principal radii r_1 and r_2 , and an interfacial tension $\gamma_{1\text{-hexanol/water}} = 6.44 \text{ mN/m}$, $\gamma_{1\text{-heptanol/water}} = 7.49 \text{ mN/m}$, and $\gamma_{1\text{-octanol/water}} = 8.19 \text{ mN/m}$ at 298.2 K between the water-rich and 1-alkanol-rich phases [149]. For a single pendular bridge between two equally sized spherical particles in contact, the principle radii will be related to the bridge volume and wetting angle. Since the capillary force is proportional to the Laplace pressure $\gamma \cdot \left(\frac{1}{r_1} + \frac{1}{r_2} \right)$ (plus the direct action of the surface tension, which is usually small) and $c_{\text{H}_2\text{O}}^0$ is lower in octanol, we would expect the yield stress to be higher, for the same $c_{\text{H}_2\text{O}}$, in octanol than heptanol or hexanol.

The discrepancy between the measured yield stress for added water and dissolved water can be explained by two things. First, there is a discrepancy in total water content. While $(V_{\text{H}_2\text{O}})/(V_{1\text{-alkanol}} + V_{\text{H}_2\text{O}}) = 3 \text{ vol}\%$ was dissolved in the 1-alkanols, upon particle addition and the assumption of complete phase separation, this yields a secondary fluid content in the capillary suspensions of $(V_{\text{H}_2\text{O}})/(V_{1\text{-alkanol}} + V_{\text{H}_2\text{O}} + V_{\text{solid}}) = 0.024$ compared to $(V_{\text{H}_2\text{O}})/(V_{1\text{-alkanol}} + V_{\text{H}_2\text{O}} + V_{\text{solid}}) = 0.03$ for the samples with water directly added. This small difference of 0.6% between the directly added liquid sample and the water content of the dissolved water sample can induce a big difference in yield stress in some capillary suspensions [34]. However, studies of a similar system with alumina suspensions in paraffin oil and sucrose enhanced water show that a yield stress plateau is reached between 2.5 vol% and 5 vol% water addition [37]. Upon further water addition, the yield stress decreases again, eventually leading to spherical agglomeration and phase separation [137, 139, 150, 151]. That means a large difference in yield stress between 2.4 vol% and 3 vol% of fully phase separated Al_2O_3 capillary suspension is not expected. A more plausible explanation is given by the kinetics of water dissolution in the conventionally formulated capillary suspension. After preparing the samples with added water, they were immediately measured. It is certainly possible that this time span is not long enough to dissolve significant amounts of water from the capillary bridge (being close to the three phase liquid-liquid-solid equilibrium state), while samples prepared from solution quickly phase separate (initially being far from equilibrium). Thus, the volume of the

bridges are perhaps smaller for the solution samples, possibly less than in the plateau volume. Qualitative observations in the lab support this theory. When sealed cups of directly prepared heptanol capillary suspensions were re-mixed after weeks, the consistency appeared to have weakened. This also explains the much smaller difference in yield stress for the added versus dissolved water for octanol. Due to the lower water solubility in octanol, only little water remains dissolved in the solution sample. Since this is more likely to place both samples in the yield stress plateau, the discrepancy is smaller for alumina in octanol sample. An effect on the yield stress caused by the thermodynamic excess volume of real mixtures is unlikely. A small change in bulk liquid volume through an interaction with small amounts of dissolved water molecules has a negligible effect on the yield stress of a sample spanning network. Likewise, 1-alkanols are practically immiscible in water (see [Figure 5.2](#)), such that a volume change of the capillary water bridge with traces of 1-alkanol has no considerable effect on the bridge volume. Therefore, if considering the samples in this work as thermodynamic real mixtures will have no measurable effect on the yield stress.

The phenomenon of temperature induced phase separation and spontaneous capillary bridge formation has been simulated by Cheng and Wang for closely packed colloidal particles [152]. They employed a diffuse-interface field model (DIFA) to describe capillary forces at liquid-liquid interfaces for suspended meso-scale particles [33]. The model describes the total free energy of a three phase liquid-liquid-solid system and accounts for diffusion between the liquid components. These calculations, which show the transient bridge size following a temperature jump, can be used as a model for the spontaneous formation of capillary bridges, leading to the formation of pendular state capillary suspensions from partially miscible liquids. Moreover, Cheng and Wang describe a self-stabilization mechanism of the capillary bridges [152]. That is, the capillary bridges are in equilibrium with one another and communicate through diffusion of the bridging liquid through the main solvent. Upon phase separation from the solution, and in contrast to conventional Ostwald ripening (coarsening), larger bridges feed smaller ones until, in a uniform structure, all bridges are of a uniform size. This effect hereby stabilizes the three-phase system to equalize the Laplace pressures in the bridges, regardless of their geometry. In pendular state capillary suspensions, the curvature of the meniscus is negative (i.e. negative Laplace pressure). By growing in size, the (negative) capillary pressure increases, leading to lower absolute pressure [152]. For capillary suspensions in the capillary state, with positively curved menisci, spontaneous phase separation is not expected to take place. In fact, this is expected to lead to aging caused by Ostwald ripening in a partially miscible system.

The demonstrated formation of capillary suspensions without an induced temperature change along with diffusion-induced stabilization proposed by Cheng and Wang [152], raises the question if capillary suspensions can also be formed when a suspension of particles in 1-alkanol is stored in an environment with high relative humidity. One can imagine that according to Henry's law, water vapor is dissolved in 1-alkanol and subsequently undergoes phase separation according to the generalized Kelvin equation. Suspensions of Al_2O_3 in pure 1-alkanol were placed in a humid environment and then re-mixed before the measurement. The yield stress results for these suspensions after 10h and 150h of exposure to moisture are shown in Figure 5.4 in dark and medium dark gray with sparse and denser lines from bottom left to top right, respectively. After 10h of exposure, there is no significant change in any of the prepared alumina suspensions. However, after 150h of storage in humid air, the 1-hexanol sample, with the largest water solubility, shows an increase in strength of one order of magnitude. On the other hand, the samples prepared from heptanol and octanol do not show an appreciative change. The reason is likely the lower water solubility along with a small free surface ($\varnothing = 48$ mm) compared to the container volume ($h \approx 50$ mm), which limited mass transport through the free surface and over the height of the container. The diffusion of water molecules from the top to the bottom of the sample volume occurs on the scale of days, which means there may be some gradient in the dissolved water concentration at 10h of exposure, but this gradient should be equilibrated by 150h. (Note that the samples were all re-mixed prior to rheological measurements so that the results are not dependent on the location within the container.) Nonetheless, this proves that capillary bridge formation in partially miscible fluids is possible when stored in a humid environment.

The formation of menisci between particles in partially miscible systems is sensitive to the surface properties of the particles. In particular, increased surface roughness will reduce the critical length scale in the Kelvin pressure, providing nucleation points for the formation for the formation of water menisci. Therefore, we investigate the influence of particles with different size and shape. For smooth, spherical glass particles, conventional water addition to a suspension illustrates a similar increase in yield-stress by two orders of magnitude. Here, it appears that water solubility in 1-alkanol plays a smaller role in this system than for irregularly shaped Al_2O_3 particles; the measured yield stress for each of the three liquids are nearly identical. The capillary suspension formed from solution (dissolved), in this glass system, exhibits an equal yield stress for hexanol, increasing for heptanol and is even larger for octanol. This trend follows the trend of increasing yield stress with decreasing water solubility. Again, a capillary suspension can be formed from solution, this time for spherical particles with much larger particle size and smoother

surface compared to the alumina system. The fact that the sample made using dissolved water has the largest yield stress, despite lower total amount of water (2.4 vol%) compared to water addition (3 vol%) as shown in [Figure 5.5](#), likely indicates that the yield stress plateau for the added water samples was exceeded and the yield stress should decrease with increasing water fraction beyond the fraction that separated from solution. Interestingly, the samples stored in a humid environment show an increase in yield stress over the pure samples, with the yield stress increasing towards hexanol with higher water solubility after 10h of storage. Interestingly, even the octanol sample, with a solubility of only 3.843 vol% water at 20 °C ([Table 5.3](#)), shows an increase in σ_y by a factor two after only 10h. After 150h, the measured yield stresses greatly increased to values nearby the conventionally formulated capillary suspensions. The hexanol sample has even surpassed the yield stress of both the conventionally prepared sample and dissolved formulation route. The difference between the yield stresses at 10 h and 150 h points to a transient process wherein the spheres promote phase separation by larger water affinity to the glass spheres, which in turn causes more water from the vapor phase to dissolve. While the rate of this process is certainly affected by the water solubility, the fact that all of the samples have the same yield stress, a yield stress value closely matching the values for both the direct and dissolved methods, implies that the final volume of water in the bridges after long times is unaffected by the mutual solubility. Of course, this equivalent yield stress obtained for the glass samples is not observed in the Al_2O_3 samples. Since the Al_2O_3 -hexanol sample stored at 150 h is much higher than the other alumina samples, and almost equivalent to the directly prepared samples, we can conclude that the rate of water transfer, and maybe even the equilibrium bridge volume, is influenced by the used particles.

For the samples prepared with TiO_2 , the particle volume fraction was drastically reduced to $\phi_{\text{solid}} = 0.04$. The aggregated particle structure causes more particle-particle interactions rendering handling difficult at high solids loading. However, in the conventional preparation technique, the water content had to be increased to $\phi_{\text{H}_2\text{O}} = 0.05$ in order to obtain a clear increase in the yield stress from the capillary suspension network. This increase in the required amount of secondary fluid required before the formation of a strong capillary suspension is likely due to the aggregated particle structure. Capillary bridges will form between the primary particles in this aggregate, decreasing the effective secondary fluid available for bridging between aggregates, which is responsible for the increase in yield stress [53]. However, determination of the water content illustrated in [Figure 5.5](#) shows that 5 vol% water could only be dissolved in hexanol, while the amount decreases towards heptanol. Indeed, comparing these values to literature values for water saturation, summarized in [Table 5.3](#), shows good agreement. Despite this discrepancy in

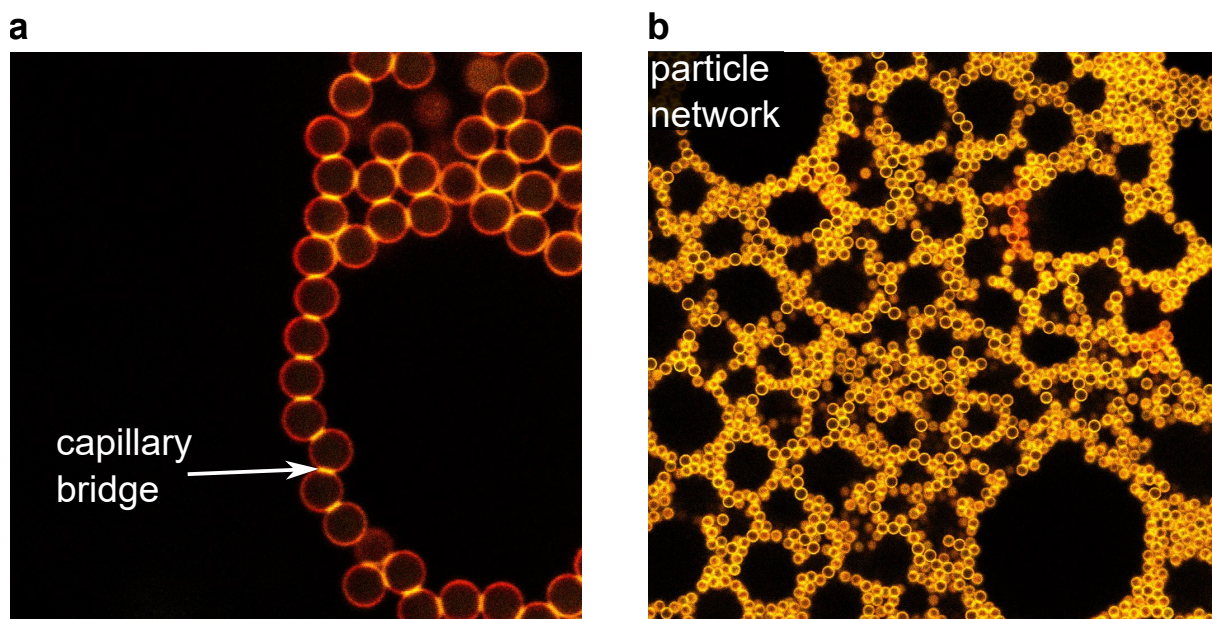


Figure 5.6: Confocal microscopy image of glass beads dispersed in a mixture of ethanol in dodecane (originally completely dissolved). Upon particle addition and mixing, the ethanol phase separates from the mixture. The fluorescent dye is soluble in ethanol and appears yellow in the composite images. The glass particles are also fluorescently labelled (red rings) and the unlabelled dodecane appears black. **(a)** The magnified image shows yellow ethanol bridges between the red glass beads, which was also observed in previous works of conventionally prepared capillary suspensions [35]. **(b)** The specimen exhibits a sample-spanning network, causing the macroscopic yield stress.

the available water, a yield stress increase was also observed for the dissolution processing route (humid storage, Figure 5.3c), with only slightly lower yield stress values as the conventional suspensions with higher water content, which likely indicates they are being in the stress plateau. Due to the larger amounts of water needed for bridge formation (and slow kinetics), storage in humid air only caused a small increase in strength in the hexanol sample and slight increase for octanol and no change from the pure suspension for heptanol. The fractal-like structure of these particles, with high internal surface area, may also promote internal bridging, which is not effective for network formation. However, this should also affect the strength of the dissolved formulation technique, which is not observed.

To further prove the concept of phase separation upon particle addition of particles to a partially miscible binary liquid, a 70 mol% ethanol in dodecane mixture was prepared at room temperature. Above ≈ 14 °C, the components are completely miscible [153]. Considering an ideal mixture, this equals to a ≈ 37 vol% ethanol in dodecane solution. Additionally, the mixture was spiked with an ethanol soluble fluorescent dye (Promofluor 488). Afterwards, 3 μm sized hydrophilic glass beads were added, amounting to a sample with a particle volume fraction of 5%. The outer surface of these particles are dyed using rhodamine B isothiocyanate [35], shown in red in Figure 5.6a. The specimen,

homogenized with a vortex mixer, was then examined with a confocal microscope. Ethanol-rich capillary bridges (yellow) are observed connecting individual particles (Figure 5.6a). These bridges are the key identifiers for capillary suspensions (pendular state) and have been observed before, however obtained with the conventional preparation technique of adding the immiscible bridging liquid to a suspension. The particles and associated bridges are arranged into a sample-spanning network (gel-structure), which causes the observed yield stress, as shown in Figure 5.6b. The structure of this sample-spanning network here, with large open structures, differs from previous observations using samples with added liquid, where an aggregated floc structure is observed [37], likely due to the difference in mixing conditions. Even with the simplified procedure here, this finding shows that capillary suspensions can form in partially miscible liquids without temperature induced phase separation. The particle roughness and their close proximity are sufficient to shift the liquid-liquid phase equilibrium.

5.4.3 Effect on drying applications

In the previous section we showed that a capillary suspension is formed when water can be partially dissolved in the bulk phase either before or after particles are added. Besides the formation of capillary suspensions, this phenomenon has implications on the drying behavior of these suspensions. In previous studies [85, 90], we investigated the drying behavior of capillary suspensions and have shown that these suspensions can reduce stresses during drying and, therefore, inhibit crack formation. However, the present results would imply that even when the solubility of the water (bridging fluid) in the bulk phase is small, water diffusion to the suspension/ air interface can dry the bridging liquid. The decreased amount of dissolved water in the solvent is continually replenished from the capillary water bridge, thus weakening the network strength that is otherwise responsible for reduced film stresses. Depending on the overall drying rate in comparison to the dissolution rate, this behavior can have a significantly negative effect. On the other hand, the formation of capillary bridges from humid air, as described here, may explain the observed peak stress reduction when capillary suspension films were dried in humid air. The larger water vapor pressure in the atmosphere prevents dissolved water from evaporating from the air-bulk liquid interface of the coating and consequently preserves the capillary water bridges for a longer time, leading to reduced peak stresses.

To investigate the discussed *in situ* formation of capillary bridges, we performed a drying experiment with a pure Al_2O_3 in 1-heptanol suspension, prepared as described above and coated onto a cantilever with a coating blade gap height of 280 μm . The coating was dried

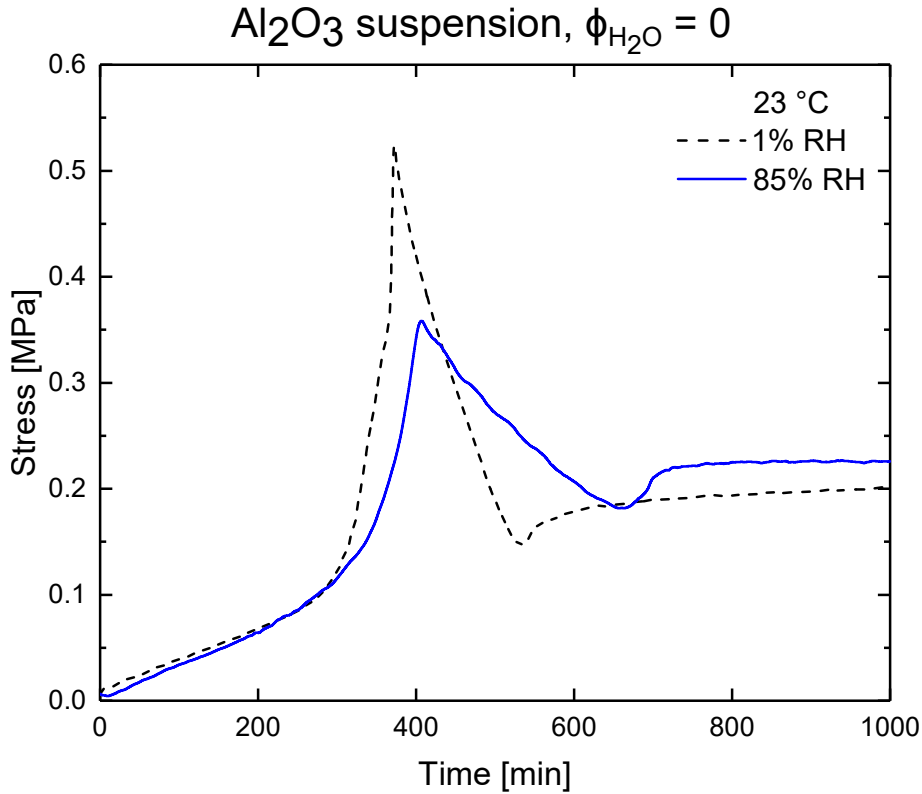


Figure 5.7: Stress development of pure Al_2O_3 in 1-heptanol suspension during drying. The employed technique is further described in [85]. Drying is carried out at low temperature without convective drying at 1 % (black dashed line) and 85 % relative humidity (blue solid line). The pure suspension dried under high humidity exhibits significant differences with stress features resembling capillary suspensions, such as pronounced reduction of peak stress, slower stress decrease and wider trough width before the final stress increase.

at very slow drying rates in the absence of forced convection (23 °C), at low and high relative humidity. The result of the stress development is shown in Figure 5.7. Details of the employed cantilever deflection technique are described elsewhere [90]. The dashed black curve shows the stress development of the pure suspension at 1 % RH and the solid blue line denotes the suspension dried at 85 % relative humidity. At the higher humidity, the peak stress is reduced, the stress release after the peak is slower, and the trough formed before the stress increases to its final residual stress value is wider. Moreover, the particle volume fraction at the peak, i.e. at full film consolidation, determined from weight measurements shifted from 0.52 to 0.48 when dried at higher humidity. This means that the porosity of the coating increased, which is another indication for water capillary bridge formation [85]. Again, these results are for a pure suspension without added water where the humidity should not play a role. This remarkable change with humidity can only be explained if water solubility in the bulk is considered. Due to the slow evaporation rate, there appears to be sufficient time for water vapor to dissolve in heptanol and subsequently *in situ* form uniformly distributed capillary bridges. While the sample stored in a vessel

only showed a modest yield stress increase after 10 h, the large area to volume ratio of coatings can facilitate this rate, promoting bridge formation. This finding strongly suggests that capillary suspensions can form *in situ* and positively influence their drying behavior.

5.5 Conclusions

In this paper, we investigated a new route to form capillary suspensions by using partially miscible liquids, even those with a low mutual solubility. We have shown, that dissolving small amounts of water (secondary phase) in 1-alkanols can lead to capillary suspension formation upon mixing, without forcing phase separation through a temperature change. Different particle sizes and shapes were shown to influence the amount and rate of nucleation. In general, octanol, with smaller partial miscibility, lead to larger yield stress samples in the dissolution preparation technique, presumably due to a more pronounced phase separation due to the fact that the thermodynamic equilibrium is the phase separated state. Moreover, we have shown the possibility to form capillary suspensions by storing the pure suspension in humid air. Spherical NP3 particles were very susceptible to forming capillary suspensions from water vapor regardless of the water solubility in the investigated 1-alkanols. Hexanol formed higher transient yield stress in the glass and the Al_2O_3 suspension only showed considerable bridge formation after 150 h in better water soluble hexanol. The TiO_2 system behaved similarly albeit at an even lower level.

An application of the described concept was presented by means of drying of pure suspensions. When dried in humid air and given sufficient time, the drying stress curve of the pure suspension exhibited a main feature of capillary suspension drying, a reduced peak stress, which leads to defect free coatings. This has clear implications for the drying of oil-based suspensions. First, the concept can be used to dry coatings in high humidity to reduce the probability of crack formation by decreasing peak stresses during drying. Secondly, it can have a negative impact on oil based coatings during storage or drying in a humid environment even though water may only be slightly soluble in the employed oils. The phase separation of dissolved water can lead to significant amounts needed for capillary bridge formation and thus particle agglomeration, which can lead to undesired alterations in the paint's rheological behavior.

Here, we demonstrated this new route for three different 1-alkanols and several particle types. To investigate the influence of the particle parameters, especially particle volume fraction and size, subsequent experiments using a single model system should be conducted. This research can also be extended to other solvents or solvent mixtures. Such mixtures

certainly modify the liquid-liquid equilibrium and resulting interfacial tension [154], but as long as there is the formation of a water-rich phase and an oil-rich phase in the presence of the particles, we should still observe phase separation and an associated increase in the yield stress. Differences in the mass transfer across the interfaces and interfacial tensions, particularly with the complication of an added solid phase, make such solvent mixtures interesting to explore in a future publication.

Conflicts of interest

There are no conflicts to declare.

Acknowledgements

The authors would like to thank Almatris GmbH for the donation of alumina particles and Sovitec for providing the OMicron NP3-P0 glass beads. Additionally, we thank the Molecular Design and Synthesis group of KU Leuven and Dr. Clio Deferm for introduction and use of the Karl Fischer titration. Jens Allard is thanked for his efforts producing the confocal image. Finally, we acknowledge financial support from the German Research Foundation (DFG) under project number KO 4805/2-1 and the Research Foundation Flanders (FWO) Odysseus Program (grant agreement no. G0H9518N).

5.6 Supplementary material

Values for Hamaker constant calculation

Table 5.4: Substance coefficients to calculate their individual Hamaker constants according to [Equation 5.2](#) from Butt and Kappl,[\[147\]](#) Values taken from literature.[\[147, 148\]](#)

Substance	ϵ [-]	n [-]	ν_e [Hz]
Al ₂ O ₃	10.4	1.75	$3.2 \cdot 10^{15}$
SiO ₂ (amorph)	3.82	1.46	$3.2 \cdot 10^{15}$
TiO ₂	114	2.46	$1.2 \cdot 10^{15}$
1-hexanol	13.0	1.418	$3.1 \cdot 10^{15}$
1-heptanol	11.8	1.425	$3.1 \cdot 10^{15}$
1-octanol	10.3	1.430	$3.1 \cdot 10^{15}$

6 Summary and Outlook

In this dissertation, I have investigated the drying behavior of pendular state capillary suspensions. In [chapter 2](#), the simultaneous stress and weight measurement apparatus is presented. This novel design, developed by me, allows the previously unaccomplished simultaneous stress and weight measurement of a coating during drying in an environmental chamber based on the cantilever deflection method. The elaborate setup can be used to set different temperatures and relative humidity, while visually tracking changes in a coating during the drying process with a camera. The major advantage of this setup is the fact that it excludes any uncertainties that arise from common practice of treating the separately obtained measures of stress and weight loss of two different coatings as if they were identical.

This new setup is then used to investigate and compare the drying behavior of a pure suspension with its respective capillary suspension in [chapter 3](#). Here, I find that the added liquid in capillary suspensions suppresses drying defects in coatings arising from lateral drying. The network structure of these pastes prevents particle migration and leads to more homogeneous shrinking. Furthermore, the employment of the newly designed setup proves a prolonged constant drying rate beyond full film compaction for the capillary suspension, which is in contrast to the pure suspension. The simultaneous measurement accompanied by the visual observations verifies that the reason for the extended overall constant rate period is attributed to liquid corner flow in the film as opposed to diffusional mass transport.

In [chapter 4](#), it is discussed how the stress measurement reveals decreased peak stresses during drying of capillary suspensions. The lower stresses in capillary suspensions imply a greater robustness of these films against cracking during drying. The examination of capillary suspensions with different network strengths at various drying conditions revealed a stress decreasing effect of the relative humidity. Additionally, exchanging the capillary suspension's secondary liquid with one possessing a higher boiling point but lower yield strength, demonstrates the complex interplay between drying stress, coating strength, and composition. Moreover, I found that even bridges from lower boiling point secondary fluids

persist for long times during drying and even beyond when the higher boiling point bulk phase has evaporated.

The previously described effect of the humidity on drying stresses led to a closer investigation of the capillary suspension system in [chapter 5](#). Conventionally, capillary suspensions are prepared by first suspending particles in the bulk liquid and subsequently adding the immiscible secondary liquid, followed by thorough mixing. However, the employed 1-alkanol–water system without particles is fully miscible at the low percentages of water that were added to induce network formation in the sample. And yet, a high yield stress paste is obtained. In [chapter 5](#), I have shown that capillary suspensions also form when the secondary liquid is dissolved first in the bulk phase and then the particles are added afterwards. Additionally, network formation is also induced when pure suspension samples are stored under high humidity and later remixed. Water vapor dissolves in the bulk liquid and phase separates at the particles. Upon mixing, a sample spanning network is obtained. I have shown the existence of this phenomenon for different particle shapes and sizes. This finding explains the effect of the humidity on the lower peak stress of the pure suspension samples observed in [chapter 4](#) at sufficiently slow evaporation rates.

This dissertation described the detailed investigation of the drying behavior of capillary suspensions, a feat accomplished via the stress measurement apparatus with its capability of simultaneously recording the drying rate. However, our experiments focused on lower temperatures, up to 40 °C. As described in [chapter 2](#), while the heating elements are powerful enough to reach a chamber temperature of up to 90 °C in order to investigate faster drying rates, improved insulation is necessary to facilitate reaching and maintaining the higher desired temperatures. Furthermore, if implemented correctly, thermal bridges could be eliminated. This is important as it would prevent water condensation when measuring at an elevated humidity. Once thermal bridges are reduced, replacing the current tubing for saturated air from the bubbler with heated tubing, a much higher humidity can be set. From an operational point of view, preventing condensation is of highest priority since condensed water can cause short circuits and the risk of electrical shocks.

While we observed a decrease in stress for capillary suspensions, as shown in [chapter 4](#), the variation in the peak stress measurement between different repetitions shows that the stress development is very sensitive to lateral drying. Lateral drying often occurs from all sides, as sketched in [Figure 6.1a](#). The effective length of the supersaturated region, which affects the cantilever deflection at the tip where the laser is positioned, may vary depending on flow conditions but also small differences in the wet coating profile. In order to minimize variations in cantilever deflection caused by differences in effective length

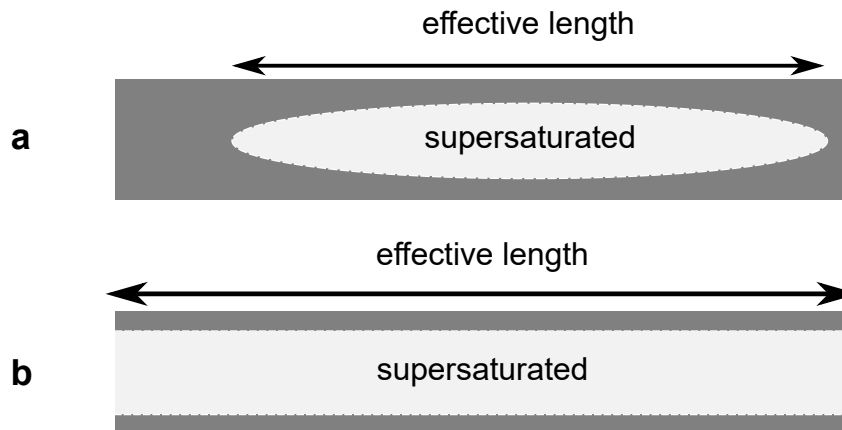


Figure 6.1: (a) Example of lateral drying of coatings from all sides on the cantilever. The supersaturated region shrinks asymmetrically, changing its effective length. (b) Lateral drying with consolidated edges but constant effective length.

rather than a mechanistically different stress development of a coating, one should try to obtain a supersaturated region with a constant effective length, as shown in [Figure 6.1b](#). Inhomogeneous natural convection on either side of the cantilever can cause distortions in the measurement. Therefore, an examination and visualization of the airflow at various drying conditions can build the basis for an optimized air flow design. By changing the amount and position of air inlets, as well as placement and orientation of the heating mats, the current design already allows for an adaptation.

In order to track lateral drying *in situ* and shrinkage in general (the *ex situ* result is shown in [Figure 3.6](#)), a laser profiler should be mounted in the recess of the chamber roof. Additionally, future work should visually confirm the proposed mechanisms of capillary flow to the surface, leaving the layers near the substrate free of liquid. For that, drying could be stopped shortly after the peak by quenching the coating in liquid nitrogen and subsequently using cryo-SEM imaging of a cross sectional cut.

Another method to reduce lateral drying is to use walled cantilevers. Price et al. [[77](#), [78](#)] developed a walled cantilever design, which causes prolonged pinning of the coating at the walls, leading to a more uniform shrinkage overall. In an endeavor to include this improvement, we already designed a first approach of the walled cantilever according to [Figure 6.2](#). In collaboration with Filip Oosterlink from DSM, we received a first etched steel substrate. While initial results showed reduced lateral drying, it was still present. Further improvements should focus on the shape of the walls from rectangular to more rounded. However, manufacturing of different edge shapes on a steel substrate via traditional manufacturing methods is challenging. Another option is available by producing PDMS walls through photolithography. However, it is important to note that such a mixture of materials, or even using something other than steel substrates, will likely lead to

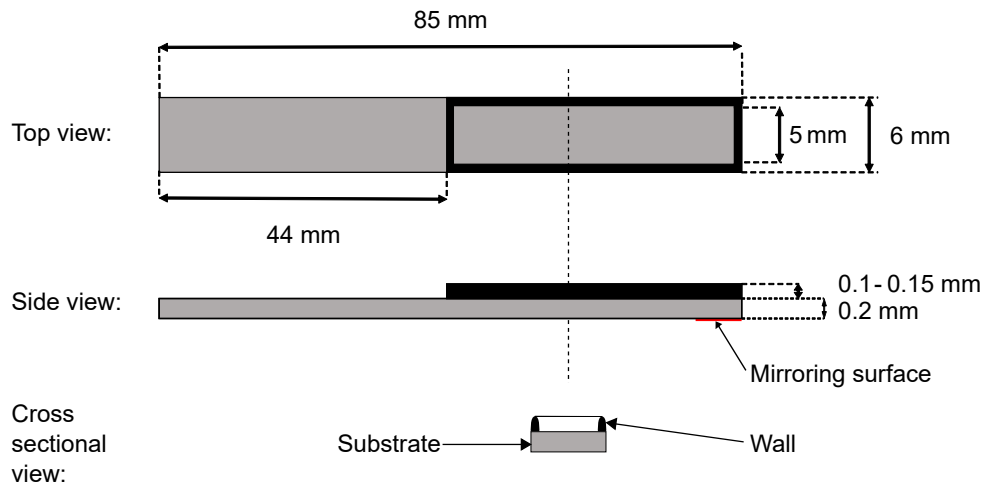


Figure 6.2: Drawing of a new cantilever design. The substrate (gray) is enhanced with walls (black) that aid in keeping the contact line pinned throughout the drying process. This design should lead to more homogeneous drying of the coatings by suppressing lateral drying.

a cantilever deflection at elevated temperatures caused by the different thermal expansion coefficients of substrate, clamp and bolts. Another advantage of an edged cantilever should be the reduction of the superelevations observed for the capillary suspension samples. This further contributes to a better comparison of formulations to be tested.

In [chapter 5](#), we have shown that capillary suspensions can be formulated in systems where the secondary water phase is only slightly soluble in the bulk phase, thus in systems experiencing a miscibility gap. We observed this phenomenon for different particle size and roughness. Phase separation occurred when water was dissolved in the bulk phase as well as when the sample was stored in humid air. We assume that water vapor dissolves in the bulk phase, diffuses through the sample, and then phase separates at the particles' surface. Upon mixing, a capillary suspension forms, as determined by a significant increase in yield stress. However, physical details remain to be investigated and evidence based on, for example, *in situ* confocal imaging of the formed capillary bridges, should be collected. Future work should map the applicability to other material systems.

In this work, the focus of the investigations was on pendular state capillary suspensions. The percolating particle network is capable of reducing drying stresses. The underlying drying mechanism in the pendular state resembles invasion percolation (IP) behavior and the pendular water bridge prevents air invasion. These findings should be extended by including capillary state capillary suspensions, which also exhibit a drastic change in yield stress and appear to reduce cracking [8]. It would be interesting to see if capillary suspensions in the capillary state obey imbibition laws and also prevent air invasion.

The investigations of the capillary suspension systems were also limited to a model system to obtain a more accessible and reliable time resolution of observed changes during

drying. In a next step, a screening should be conducted for industrially relevant and applicable capillary suspension formulations with a market orientation. Furthermore, these capillary suspensions should then be compared to commercial formulations of interest. While the ultimate goal is to completely avoid polymeric additives in order to reduce further processing steps, it should be investigated how much binder is needed in capillary suspensions to obtain ideal adhesion of these coatings to the various substrates.

List of Figures

1.1	Comparison of meniscus formation in a coating with the liquid level rise in a capillary tube.	3
1.2	Sessile droplet with a variation of the local drying rate, depending on the droplet's contact angle.	4
1.3	Yield stress of pendular and capillary state capillary suspensions depending on the volume fraction of the wetting liquid. Confocal images depicting visual confirmation of different contact angles.	6
1.4	Flow and yielding behavior of capillary suspensions visualized on a tilted plate with varying amounts of secondary liquid.	7
1.5	Sketched microstructure of a capillary suspension, showing connected particle flocs with a connecting backbone structure.	9
1.6	Exemplary shear stress vs. strain curve with added tangents. The apparent yield stress is obtained at the tangent intersection.	11
1.7	Comparison of freely shrinking hypothetical film layers versus a film adhering to a substrate [58, 59]. Adhesion to the substrate induces stress during drying.	12
1.8	Schematic illustrating occurring forces in a capillary suspension during drying.	14
2.1	Sketch of the cantilever deflection technique.	20
2.2	Photograph of the stress measurement apparatus on top of an optical table.	21
2.3	Cross sectional front view of the aluminum drying chamber covered with polycarbonate insulation sheets.	22
2.4	Drying air conditioning unit for temperature and humidity adjustments.	24
2.5	Custom made coating setup machined from a steel slab with recess for the fixture and cantilever along with a power supply for adjusting the coating speed through voltage.	24
2.6	Tool for lifting the cantilever fixture at a precise position and orientation in order to connect to the suspended weighing mechanism.	25
2.7	Attaching mechanism with lifting tool.	26
2.8	Digitally integrated and acquired data. Measures include chamber sensors as well as pre-processing (calibration) and post processing (film thickness).	27
2.9	Tool and working principle for the cantilever deflection calibration.	29
2.10	Simultaneous stress and weight measurement of 25 vol% alumina particles suspended in 1-heptanol with 3.1 vol% added glycerol, dried at 40 °C and 1% relative humidity over time.	30

3.1	Graphical abstract to “using an added liquid to suppress drying defects in hard particle coatings”.	34
3.2	Steel made coating rig with the clamped cantilever fixture; schematic of the humidity and temperature controlled drying chamber.	38
3.3	Film stress and intensity of the investigated film in comparison with the visually obtained images for the pure suspension and a capillary suspension.	41
3.4	Film stress and intensity of the investigated film in comparison with the visually obtained images for the pure suspension and a capillary suspension with bulk phase dyed in red.	44
3.5	Film stress and intensity of the investigated film in comparison with the visually obtained images for the pure suspension and a capillary suspension with its water phase dyed with a fluorescent tracer.	46
3.6	Film profile measurements during drying of a pure suspension and a capillary suspension at 40 °C. A map height scan of these suspensions dried in the drying chamber is shown on the right.	47
3.7	Schematic drawing comparing proposed drying mechanisms for a regular suspension and a capillary suspension.	50
3.8	Film profile measurements during drying of a pure suspension and a capillary suspension at 30 °C. A map height scan of these suspensions dried in the drying chamber is shown on the right.	58
3.9	Dry film profilometry comparison matrix for varied drying temperature and pure vs capillary suspension.	59
4.1	Graphical abstract to Influence of drying conditions on the stress and weight development of capillary suspensions.	62
4.2	Steel made coating rig with the clamped cantilever fixture; schematic of the humidity and temperature controlled drying chamber.	66
4.3	The results for simultaneous stress and weight measurement at a drying temperature of 40 °C and 1% RH for a regular suspension compared to a capillary suspension.	71
4.4	Yield stress measurements of samples with a variation in secondary fluid contents and initial particle volume fraction; comparison in peak film stress for drying experiments with a variation in secondary fluid content and initial particle volume fraction.	75
4.5	The average dry film particle volume fraction of the experiments obtained from the particle volume fraction at the peaks.	79
4.6	Residual solvent loading for differently formulated suspensions with increasing water content and initial particle load.	82
4.7	Results for thermogravimetical analysis coupled with mass spectrometry over time for drying of capillary suspensions.	84
5.1	Graphical abstract to “capillary bridge formation at room temperature in binary liquids with small miscibility”.	90

5.2	Approximated temperature dependence of mutual solubilities of 1-alkanols and water in terms of wt%.	94
5.3	Overview of the capillary suspension preparation techniques used: conventional-, dissolution-, and humid storage technique.	96
5.4	Yield stress of samples prepared from different particle materials.	97
5.5	Water content of the 1-alkanol stock solutions as determined by coulometric Karl Fischer titration, used to prepare the suspensions.	100
5.6	Confocal microscopy image of glass beads dispersed in a mixture of ethanol in dodecane (originally completely dissolved).	105
5.7	Stress development of pure Al_2O_3 in 1-heptanol suspension during drying at low and high relative humidity (RH).	107
6.1	Example of different lateral drying patterns affecting the deflection of the cantilever.	113
6.2	Drawing of a new cantilever design with added walls.	114

List of Tables

4.1	Composition and coating parameters for each sample tested.	65
4.2	TGA profile for measuring the residual fluid content.	69
5.1	Capillary suspension formulation parameters for directly added water (conventional formulation) and water content measured in solution (solution formulation).	93
5.2	Calculated Hamaker constants according to Equation 5.2 [147] with required values taken from Butt and Kappl, Franz and Butt [147, 148].	98
5.3	Mutual solubilities [vol%] of 1-alkanol ($C_nH_{2n+1}OH$) and water (H_2O) mixtures at 20 °C. Approximated, assuming ideal mixtures, from Maczynski et al. [144, 145, 146].	99
5.4	Substance coefficients to calculate their individual Hamaker constants according to Equation 5.2 from Butt and Kappl.[147] Values taken from literature.[147, 148]	110

List of Publications

Journal articles

- [Article1] Steffen B. Fischer and Erin Koos. Capillary bridge formation at room temperature in binary liquids with small miscibility. *Colloid and Interface Science Communications*, 41:100373, 2021. doi: 10.1016/j.colcom.2021.100373.
- [Article2] Steffen B. Fischer and Erin Koos. Apparatus for simultaneous stress and weight measurement during film drying in an environmentally controlled chamber. *Review of Scientific Instruments*, 91(12):123904, 2020. doi: 10.1063/5.0030739. *Selected as Editor's pick.*
- [Article3] Steffen B. Fischer and Erin Koos. Influence of drying conditions on the stress and weight development of capillary suspensions. *Journal of the American Ceramic Society*, 104(3):1255–1270, 2021. doi: 10.1111/jace.17553.
- [Article4] Steffen B. Fischer and Erin Koos. Using an added liquid to suppress drying defects in hard particle coatings. *Journal of Colloid and Interface Science*, 582(Part B):1231–1242, 2021. doi: 10.1016/j.jcis.2020.08.055.
- [Article5] Monica Schneider, Johannes Maurath, Steffen B. Fischer, Moritz Weiss, Norbert Willenbacher, and Erin Koos. Suppressing crack formation in particulate systems by utilizing capillary forces. *ACS Applied Materials & Interfaces*, 9(12):11095–11105, 2017. doi: 10.1021/acsami.6b13624.

Conference contributions

Oral presentations

- [Oral1] S. B. Fischer and E. Koos. Insights into the drying behavior of capillary suspensions. Jahrestreffen der ProcessNet-Fachgruppen Mischvorgänge, Trocknungstechnik und Wärme- und Stoffübertragung, Essen (Germany), 2019. *Plenary talk*.
- [Oral2] S. B. Fischer and E. Koos. Simultaneous stress and weight measurements for particulate films made from capillary suspensions. 19th International Society of Coating Science and Technology Symposium, Long Beach, CA (USA), 2018.
- [Oral3] S. B. Fischer and E. Koos. Insights into the drying behavior of capillary suspensions. 19th International Society of Coating Science and Technology Symposium, Long Beach, CA (USA), 2018.
- [Oral4] S. B. Fischer and E. Koos. Simultaneous stress and weight measurements during drying of particulate films made from capillary suspensions. Jahrestreffen der ProcessNet-Fachgruppen Mechanische Flüssigkeitsabtrennung, Trocknungstechnik und Grenzflächenbestimmte Systeme und Prozesse, Merseburg (Germany), 2018.
- [Oral5] F. Bossler, I. Natalia, M. Weiss, S. B. Fischer, and E. Koos. Structure of capillary suspensions and their applications. 2017 MRS Fall Meeting & Exhibit, Boston, MA (USA), 2017.
- [Oral6] S. B. Fischer and E. Koos. Simultaneous stress and weight measurements for particulate films made from capillary suspension. European Coating Symposium, Fribourg (Switzerland), 2017.
- [Oral7] S. B. Fischer and E. Koos. Simultaneous stress and weight measurements for particulate films made from capillary suspension. 31st Conference of The European Colloid and Interface Society, Madrid (Spain), 2017.

Poster presentations

- [Poster1] S. B. Fischer and E. Koos. Simultaneous stress and weight measurements for particulate films made from capillary suspensions. Joint Symposium of the Belgian Group of Rheology, German Rheological Society, Luxembourg City (Luxembourg), 2018.
- [Poster2] S. B. Fischer and E. Koos. Simultaneous stress and weight measurements for particulate films made from capillary suspensions. 2017 MRS Fall Meeting & Exhibit, Boston, MA (USA), 2017. *Best Poster Award Nominee*.
- [Poster3] S. B. Fischer and E. Koos. Stress development during drying of particulate films made from capillary suspensions. Functional Coatings Winter School, Hasselt (Belgium), 2016.
- [Poster4] S. B. Fischer and E. Koos. Stress development during drying of particulate films made from capillary suspensions. 30th Conference of The European Colloid and Interface Society, Rome (Italy), 2016.

Bibliography

- [1] Mirela Vlad Cristea, Bernard Riedl, and Pierre Blanchet. Enhancing the performance of exterior waterborne coatings for wood by inorganic nanosized uv absorbers. *Progress in Organic Coatings*, 69(4):432–441, 2010. ISSN 03009440. doi: 10.1016/j.porgcoat.2010.08.006.
- [2] L. D. Chambers, K. R. Stokes, F. C. Walsh, and R.J.K. Wood. Modern approaches to marine antifouling coatings. *Surface and Coatings Technology*, 201(6):3642–3652, 2006. ISSN 0257-8972. doi: 10.1016/j.surfcoat.2006.08.129. URL <http://www.sciencedirect.com/science/article/pii/S0257897206009364>.
- [3] Susan E. Habas, Heather A. S. Platt, Maikel F. A. M. van Hest, and David S. Ginley. Low-cost inorganic solar cells: from ink to printed device. *Chemical reviews*, 110(11):6571–6594, 2010. doi: 10.1021/cr100191d.
- [4] Liangbing Hu, Hui Wu, Fabio La Mantia, Yuan Yang, and Yi Cui. Thin, flexible secondary li-ion paper batteries. *ACS nano*, 4(10):5843–5848, 2010. doi: 10.1021/nn1018158.
- [5] Alexander Kamyshny and Shlomo Magdassi. Conductive nanomaterials for printed electronics. *Small*, 10(17):3515–3535, 2014. ISSN 16136810. doi: 10.1002/smll.201303000.
- [6] Mark A. M. Leenen, Volker Arning, Heiko Thiem, Jürgen Steiger, and Ralf Anselmann. Printable electronics: Flexibility for the future. *physica status solidi (a)*, 206(4):588–597, 2009. ISSN 18626300. doi: 10.1002/pssa.200824428.
- [7] Jayavardhana Gubbi, Rajkumar Buyya, Slaven Marusic, and Marimuthu Palaniswami. Internet of things (iot): A vision, architectural elements, and future directions. *Future Generation Computer Systems*, 29(7):1645–1660, 2013. ISSN 0167739X. doi: 10.1016/j.future.2013.01.010.
- [8] Monica Schneider, Johannes Maurath, Steffen B. Fischer, Moritz Weiss, Norbert Willenbacher, and Erin Koos. Suppressing crack formation in particulate systems by

- utilizing capillary forces. *ACS Applied Materials & Interfaces*, 9(12):11095–11105, 2017. ISSN 1944-8244. doi: 10.1021/acsami.6b13624.
- [9] Erin Koos and Norbert Willenbacher. Capillary forces in suspension rheology. *Science*, 331(6019):897–900, 2011. doi: 10.1126/science.1199243. URL <http://science.sciencemag.org/content/sci/331/6019/897.full.pdf>.
- [10] Erin Koos, Julia Johannsmeier, Linda Schwebler, and Norbert Willenbacher. Tuning suspension rheology using capillary forces. *Soft Matter*, 8(24):6620, 2012. ISSN 1744-683X. doi: 10.1039/C2SM25681A.
- [11] Ceren Yüce, Markus König, and Norbert Willenbacher. Rheology and screen-printing performance of model silver pastes for metallization of si-solar cells. *Coatings*, 8(11):406, 2018. doi: 10.3390/coatings8110406.
- [12] Christoph Gogelein, Martin Brinkmann, Matthias Schroter, and Stephan Herminghaus. Controlling the formation of capillary bridges in binary liquid mixtures. *Langmuir*, 26(22):17184–17189, 2010. ISSN 0743-7463. doi: 10.1021/la103062s.
- [13] By Jolke Perelaer, Antonius W. M. de Laat, Chris E. Hendriks, and Ulrich S. Schubert. Inkjet-printed silver tracks: Low temperature curing and thermal stability investigation. *Journal of Materials Chemistry*, 18(27):3209, 2008. ISSN 0959-9428. doi: 10.1039/b720032c.
- [14] Jolke Perelaer, Patrick J. Smith, Dario Mager, Daniel Soltman, Steven K. Volkman, Vivek Subramanian, Jan G. Korvink, and Ulrich S. Schubert. Printed electronics: The challenges involved in printing devices, interconnects, and contacts based on inorganic materials. *Journal of Materials Chemistry*, 20(39):8446, 2010. ISSN 0959-9428. doi: 10.1039/c0jm00264j.
- [15] George W. Scherer. Theory of drying. *Journal of the American Ceramic Society*, 73(1):3–14, 1990. ISSN 1551-2916. doi: 10.1111/j.1151-2916.1990.tb05082.x.
- [16] Christine M. Cardinal, Yoon Dong Jung, Kyung Hyun Ahn, and L. F. Francis. Drying regime maps for particulate coatings. *AIChE Journal*, 56(11):2769–2780, 2010. ISSN 00011541. doi: 10.1002/aic.12190.
- [17] Jau-Ho Jean and Hong-Ren Wang. Organic distributions in dried alumina green tape. *Journal of the American Ceramic Society*, 84(2):267–272, 2001. ISSN 1551-2916. doi: 10.1111/j.1151-2916.2001.tb00648.x.

- [18] Tohru Okuzono, Kin'ya Ozawa, and Masao Doi. Simple model of skin formation caused by solvent evaporation in polymer solutions. *Physical Review Letters*, 97(13):136103, 2006. doi: 10.1103/PhysRevLett.97.136103. URL <http://link.aps.org/pdf/10.1103/PhysRevLett.97.136103>.
- [19] Stefan Jaiser, Marcus Müller, Michael Baunach, Werner Bauer, Philip Scharfer, and Wilhelm Schabel. Investigation of film solidification and binder migration during drying of li-ion battery anodes. *Journal of Power Sources*, 318:210–219, 2016. ISSN 03787753. doi: 10.1016/j.jpowsour.2016.04.018. URL <http://www.sciencedirect.com/science/article/pii/S0378775316303561>.
- [20] Stefan Jaiser, Jana Kumberg, Jop Klaver, Janos L. Urai, Wilhelm Schabel, Joyce Schmatz, and Philip Scharfer. Microstructure formation of lithium-ion battery electrodes during drying – an ex-situ study using cryogenic broad ion beam slope-cutting and scanning electron microscopy (cryo-bib-sem). *Journal of Power Sources*, 345:97–107, 2017. ISSN 03787753. doi: 10.1016/j.jpowsour.2017.01.117. URL <http://www.sciencedirect.com/science/article/pii/S0378775317301374>.
- [21] Mahesh S. Tirumkudulu and William B. Russel. Role of capillary stresses in film formation. *Langmuir*, 20(7):2947–2961, 2004. ISSN 0743-7463. doi: 10.1021/la0356250.
- [22] Christine C. Roberts and Lorraine F. Francis. Drying and cracking of soft latex coatings. *Journal of Coatings Technology and Research*, 10(4):441–451, 2013. ISSN 1547-0091. doi: 10.1007/s11998-012-9425-7.
- [23] A. G. Evans, M. D. Drory, and M. S. Hu. The cracking and decohesion of thin films. *Journal of Materials Research*, 3(5):1043–1049, 1988. ISSN 0884-2914. doi: 10.1557/JMR.1988.1043.
- [24] Alan T. Zehnder. Griffith theory of fracture. In Q. Jane Wang and Yip-Wah Chung, editors, *Encyclopedia of Tribology*, pages 1570–1573. Springer US, Boston, MA, 2013. ISBN 978-0-387-92896-8. doi: 10.1007/978-0-387-92897-5{\textunderscore}259.
- [25] R.G Picknett and R. Bexon. The evaporation of sessile or pendant drops in still air. *Journal of Colloid and Interface Science*, 61(2):336–350, 1977. ISSN 0021-9797. doi: 10.1016/0021-9797(77)90396-4.
- [26] N. M. Kovalchuk, A. Trybala, and V. M. Starov. Evaporation of sessile droplets. *Current Opinion in Colloid & Interface Science*, 19(4):336–342, 2014. ISSN 1359-0294. doi: 10.1016/j.cocis.2014.07.005.

- [27] Hua Hu and Ronald G. Larson. Evaporation of a sessile droplet on a substrate. *The Journal of Physical Chemistry B*, 106(6):1334–1344, 2002. ISSN 1520-6106. doi: 10.1021/jp0118322.
- [28] Robert D. Deegan, Olgica Bakajin, Todd F. Dupont, Greb Huber, Sidney R. Nagel, and Thomas A. Witten. Capillary flow as the cause of ring stains from dried liquid drops. *Nature*, 389(6653):827–829, 1997. ISSN 0028-0836. doi: 10.1038/39827.
- [29] Martin Still. *Temperaturmessungen und Analyse von Wärme- und Stofftransportvorgängen bei verdunstenden Tropfen*. PhD thesis, Technische Universität Darmstadt, 2017.
- [30] Jan Mewis and Norman J. Wagner. *Colloidal Suspension Rheology*. Cambridge University Press, Cambridge, 2011. ISBN 9780511977978. doi: 10.1017/CBO9780511977978.
- [31] Gerhard Fritz, Volker Schädler, Norbert Willenbacher, and Norman J. Wagner. Electrosteric stabilization of colloidal dispersions. *Langmuir*, 18(16):6381–6390, 2002. ISSN 0743-7463. doi: 10.1021/la015734j.
- [32] S. Sadri Moghaddam, M. R. Alavi Moghaddam, and M. Arami. Coagulation/flocculation process for dye removal using sludge from water treatment plant: optimization through response surface methodology. *Journal of hazardous materials*, 175(1-3):651–657, 2010. doi: 10.1016/j.jhazmat.2009.10.058.
- [33] Paul C. Millett and Yu U. Wang. Diffuse-interface field approach to modeling arbitrarily-shaped particles at fluid-fluid interfaces. *Journal of Colloid and Interface Science*, 353(1):46–51, 2011. ISSN 0021-9797. doi: 10.1016/j.jcis.2010.09.021.
- [34] Erin Koos. Capillary suspensions: Particle networks formed through the capillary force. *Current Opinion in Colloid & Interface Science*, 19(6):575–584, 2014. ISSN 1359-0294. doi: 10.1016/j.cocis.2014.10.004.
- [35] Frank Bossler and Erin Koos. Structure of particle networks in capillary suspensions with wetting and nonwetting fluids. *Langmuir*, 32(6):1489–1501, 2016. ISSN 0743-7463. doi: 10.1021/acs.langmuir.5b04246.
- [36] Frank Bossler, Lydia Weyrauch, Robert Schmidt, and Erin Koos. Influence of mixing conditions on the rheological properties and structure of capillary suspensions. *Nanoscience and Nanotechnology*, 518:85–97, 2017. ISSN 0927-7757. doi: 10.1016/j.colurfa.2017.01.026.
- [37] Frank Bossler, Johannes Maurath, Katrin Dyhr, Norbert Willenbacher, and Erin Koos. Fractal approaches to characterize the structure of capillary suspensions using

- rheology and confocal microscopy. *Journal of Rheology*, 62(1):183–196, 2018. ISSN 0148-6055. doi: 10.1122/1.4997889.
- [38] Katharina Hauf, Kamran Riazi, Norbert Willenbacher, and Erin Koos. Radical polymerization of capillary bridges between micron-sized particles in liquid bulk phase as a low temperature route to produce porous solid materials. *Colloid and Polymer Science*, 295(10):1773–1785, 2017. ISSN 0303-402X. doi: 10.1007/s00396-017-4149-y.
- [39] Irene Natalia, Nicole Zeiler, Moritz Weiß, and Erin Koos. Negative normal stress differences n_1 - n_2 in a low concentration capillary suspension. *Soft Matter*, 14(17):3254–3264, 2018. ISSN 1744-683X. doi: 10.1039/c8sm00305j.
- [40] Irene Natalia, Randy H. Ewoldt, and Erin Koos. Questioning a fundamental assumption of rheology: Observation of noninteger power expansions. *Journal of Rheology*, 64(3):625–635, 2020. ISSN 0148-6055. doi: 10.1122/1.5130707.
- [41] Erin Koos, Wolfgang Kannowade, and Norbert Willenbacher. Restructuring and aging in a capillary suspension. *Rheologica Acta*, 53(12):947–957, 2014. ISSN 1435-1528. doi: 10.1007/s00397-014-0805-z.
- [42] Hans-Jürgen Butt and Michael Kappl. Normal capillary forces. *Advances in Colloid and Interface Science*, 146(1–2):48–60, 2009. ISSN 0001-8686. doi: 10.1016/j.cis.2008.10.002.
- [43] W. Pietsch and H. Rumpf. Haftkraft, Kapillardruck, Flüssigkeitsvolumen und Grenzwinkel einer Flüssigkeitsbrücke zwischen zwei Kugeln. *Chemie Ingenieur Technik*, 39(15):885–893, 1967. ISSN 0009286X. doi: 10.1002/cite.330391502.
- [44] Stefanie Strauch and Stephan Herminghaus. Wet granular matter: a truly complex fluid. *Soft Matter*, 8(32):8271, 2012. ISSN 1744-683X. doi: 10.1039/C2SM25883H.
- [45] Jens Dittmann, Erin Koos, and Norbert Willenbacher. Ceramic capillary suspensions: Novel processing route for macroporous ceramic materials. *Journal of the American Ceramic Society*, 96(2):391–397, 2013. ISSN 0002-7820. doi: 10.1111/jace.12126.
- [46] Jens Dittmann, Norbert Willenbacher, and G. Franks. Micro structural investigations and mechanical properties of macro porous ceramic materials from capillary suspensions. *Journal of the American Ceramic Society*, 97(12):3787–3792, 2014. ISSN 1551-2916. doi: 10.1111/jace.13184.

- [47] Susanne Hoffmann, Erin Koos, and Norbert Willenbacher. Using capillary bridges to tune stability and flow behavior of food suspensions. *Food Hydrocolloids*, 40:44–52, 2014. ISSN 0268-005X. doi: 10.1016/j.foodhyd.2014.01.027.
- [48] Susanne Wollgarten, Ceren Yuce, Erin Koos, and Norbert Willenbacher. Tailoring flow behavior and texture of water based cocoa suspensions. *Food Hydrocolloids*, 52: 167–174, 2015. ISSN 0268-005X. doi: 10.1016/j.foodhyd.2015.06.010.
- [49] Johannes Maurath, Jens Dittmann, Niko Schultz, and Norbert Willenbacher. Fabrication of highly porous glass filters using capillary suspension processing. *Separation and Purification Technology*, 149:470–478, 2015. ISSN 13835866. doi: 10.1016/j.seppur.2015.06.022.
- [50] Monica Schneider, Erin Koos, and Norbert Willenbacher. Highly conductive, printable pastes from capillary suspensions. *Scientific Reports*, 6:31367, 2016. doi: 10.1038/srep 31367.
- [51] Moritz Weiß, Johannes Maurath, Norbert Willenbacher, and Erin Koos. Shrinkage and dimensional accuracy of porous ceramics derived from capillary suspensions. *Journal of the European Ceramic Society*, 39(5):1887–1892, 2019. ISSN 09552219. doi: 10.1016/j.jeurceramsoc.2019.01.011.
- [52] Katharina Hartung, Carolyn Benner, Norbert Willenbacher, and Erin Koos. Lightweight porous glass composite materials based on capillary suspensions. *Materials*, 12(4), 2019. ISSN 1996-1944. doi: 10.3390/ma12040619.
- [53] Sebastian Bindgen, Frank Bossler, Jens Allard, and Erin Koos. Connecting particle clustering and rheology in attractive particle networks. *Soft Matter*, 2020. ISSN 1744-683X. doi: 10.1039/d0sm00861c.
- [54] Raymond C. Chiu and Michael J. Cima. Drying of granular ceramic films: Ii, drying stress and saturation uniformity. *Journal of the American Ceramic Society*, 76(11): 2769–2777, 1993. ISSN 1551-2916. doi: 10.1111/j.1151-2916.1993.tb04014.x.
- [55] J. Jiyou Guo and Jennifer A. Lewis. Aggregation effects on the compressive flow properties and drying behavior of colloidal silica suspensions. *Journal of the American Ceramic Society*, 82(9):2345–2358, 1999. ISSN 1551-2916. doi: 10.1111/j.1151-2916.1999.tb02090.x.
- [56] Glenn M. Channell and Charles F. Zukoski. Shear and compressive rheology of aggregated alumina suspensions. *AIChE Journal*, 43(7):1700–1708, 1997. ISSN 00011541. doi: 10.1002/aic.690430707.

- [57] Zhongwu Zhou, Peter J. Scales, and David V. Boger. Chemical and physical control of the rheology of concentrated metal oxide suspensions. *Chemical Engineering Science*, 56(9):2901–2920, 2001. ISSN 0009-2509. doi: 10.1016/S0009-2509(00)00473-5.
- [58] H. Lei, L. F. Francis, W. W. Gerberich, and L. E. Scriven. Stress development in drying coatings after solidification. *American Institute of Chemical Engineers. AIChE Journal*, 48(3):437–451, 2002. ISSN 0001-1541.
- [59] L. F. Francis, A. V. McCormick, D. M. Vaessen, and J. A. Payne. Development and measurement of stress in polymer coatings. *Journal of Materials Science*, 37(22):4717–4731, 2002. ISSN 00222461. doi: 10.1023/A:1020886802632.
- [60] Kerstin von der Ehe and Diethelm Johannsmann. Maps of the stress distributions in drying latex films. *Review of Scientific Instruments*, 78(11):113904, 2007. doi: 10.1063/1.2805515.
- [61] Alexander F. Routh. Drying of thin colloidal films. *Reports on progress in physics. Physical Society (Great Britain)*, 76(4):046603, 2013. doi: 10.1088/0034-4885/76/4/046603. URL <http://iopscience.iop.org/article/10.1088/0034-4885/76/4/046603/pdf>.
- [62] Jutta Böhnlein-Mauß, Wolfgang Sigmund, Gerhard Wegner, Wolfgang H. Meyer, Friedrich Heßel, Katharina Seitz, and Andreas Roosen. The function of polymers in the tape casting of alumina. *Advanced Materials*, 4(2):73–81, 1992. ISSN 0935-9648. doi: 10.1002/adma.19920040203.
- [63] D. Hotza and P. Greil. Review: Aqueous tape casting of ceramic powders. *Materials Science and Engineering: A*, 202(1-2):206–217, 1995. ISSN 09215093. doi: 10.1016/0921-5093(95)09785-6.
- [64] Christiane Bauer, Michael Cima, Armin Dellert, and Andreas Roosen. Stress development during drying of aqueous zirconia based tape casting slurries measured by transparent substrate deflection method. *Journal of the American Ceramic Society*, 92(6):1178–1185, 2009. ISSN 1551-2916. doi: 10.1111/j.1551-2916.2009.03000.x.
- [65] Dah-Shyang Tsai. Pressure buildup and internal stresses during binder burnout: Numerical analysis. *AIChE Journal*, 37(4):547–554, 1991. ISSN 00011541. doi: 10.1002/aic.690370408.
- [66] Zongwen Fu and Andreas Roosen. Shrinkage of tape cast products during binder burnout. *Journal of the American Ceramic Society*, 98(1):20–29, 2015. ISSN 1551-2916.

- [67] Pär Wedin, Carlos J. Martinez, Jennifer A. Lewis, John Daicic, and Lennart Bergström. Stress development during drying of calcium carbonate suspensions containing carboxymethylcellulose and latex particles. *Journal of Colloid and Interface Science*, 272(1):1–9, 2004. ISSN 0021-9797. doi: 10.1016/j.jcis.2003.12.030.
- [68] Steffen B. Fischer and Erin Koos. Apparatus for simultaneous stress and weight measurement during film drying in an environmentally controlled chamber. *Review of Scientific Instruments*, 91(12):123904, 2020. doi: 10.1063/5.0030739.
- [69] Matthijs Groenewolt. Highly scratch resistant coatings for automotive applications. *Progress in Organic Coatings*, 61(2-4):106–109, 2008. ISSN 03009440. doi: 10.1016/j.porgcoat.2007.07.036.
- [70] C. Allain and Limat L. Regular patterns of cracks formed by directional drying of a colloidal suspension. *Physical Review Letters*, 74(15):2981–2984, 1995. doi: 10.1103/PhysRevLett.74.2981.
- [71] R. C. Chiu, T. J. Garino, and M. J. Cima. Drying of granular ceramic films: I, effect of processing variables on cracking behavior. *Journal of the American Ceramic Society*, 76(9):2257–2264, 1993. ISSN 1551-2916. doi: 10.1111/j.1151-2916.1993.tb07762.x.
- [72] Derek M. Holmes, R. Vasant Kumar, and William J. Clegg. Cracking during lateral drying of alumina suspensions. *Journal of the American Ceramic Society*, 89(6):1908–1913, 2006. ISSN 0002-7820. doi: 10.1111/j.1551-2916.2006.01053.x.
- [73] G. Gerald Stoney. The tension of metallic films deposited by electrolysis. *Proc. R. Soc. London, Ser. A (Proceedings of the Royal Society of London. Series A, Containing Papers of a Mathematical and Physical Character)*, 82(553):172–175, 1909. doi: 10.1098/rspa.1909.0021.
- [74] G. B. Raju, D. J. Green, and O. Guillon. Evaluation of drying stresses in coatings using an optical method. *Measurement Science and Technology*, 23(8):085609, 2012. ISSN 0957-0233. doi: 10.1088/0957-0233/23/8/085609.
- [75] Alexander M. König and Diethelm Johannsmann. Stress fluctuations in drying polymer dispersions. *Langmuir*, 26(12):9437–9441, 2010. ISSN 0743-7463. doi: 10.1021/la100454z.
- [76] Carlos J. Martinez and Jennifer A. Lewis. Shape evolution and stress development during latex–silica film formation. *Langmuir*, 18(12):4689–4698, 2002. ISSN 0743-7463. doi: 10.1021/la0114833.

- [77] Kyle K. Price, Alon V. McCormick, and Lorraine F. Francis. Cryosem investigation of latex coatings dried in walled substrates. *Langmuir*, 28(28):10329–10333, 2012. ISSN 0743-7463. doi: 10.1021/la302317r.
- [78] Kyle K. Price, Yan Wu, Alon V. McCormick, Lorraine F. Francis, and G. Scherer. Stress development in hard particle coatings in the absence of lateral drying. *Journal of the American Ceramic Society*, 98(7):2214–2222, 2015. ISSN 1551-2916. doi: 10.1111/jace.13580.
- [79] Jason A. Payne, Alon V. McCormick, and Lorraine F. Francis. In situ stress measurement apparatus for liquid applied coatings. *Review of Scientific Instruments*, 68(12):4564–4568, 1997. doi: 10.1063/1.1148432. URL <http://scitation.aip.org/content/aip/journal/rsi/68/12/10.1063/1.1148432>.
- [80] H. Lei, J. A. Payne, A. V. McCormick, L. F. Francis, W. W. Gerberich, and L. E. Scriven. Stress development in drying coatings. *Journal of Applied Polymer Science*, 81(4):1000–1013, 2001. ISSN 1097-4628. doi: 10.1002/app.1522. URL <http://online.library.wiley.com/doi/10.1002/app.1522/full>.
- [81] Sunhyung Kim, Jun Hee Sung, Kyung Hyun Ahn, and Seung Jong Lee. Drying of the silica/pva suspension: effect of suspension microstructure. *Langmuir*, 25(11):6155–6161, 2009. ISSN 0743-7463. doi: 10.1021/la804112b.
- [82] Huai Nyin Yow, Itxaso Beristain, Monika Goikoetxea, Maria J. Barandiaran, and Alexander F. Routh. Evolving stresses in latex films as a function of temperature. *Langmuir*, 26(9):6335–6342, 2010. ISSN 0743-7463. doi: 10.1021/la1007439.
- [83] Zongwen Fu, Udo Eckstein, Armin Dellert, and Andreas Roosen. In situ study of mass loss, shrinkage and stress development during drying of cast colloidal films. *Journal of the European Ceramic Society*, 35(10):2883–2893, 2015. ISSN 09552219. doi: 10.1016/j.jeurceramsoc.2015.03.029.
- [84] J. Kiennemann, T. Chartier, C. Pagnoux, J. F. Baumard, M. Huger, and J. M. Laméran. Drying mechanisms and stress development in aqueous alumina tape casting. *Journal of the European Ceramic Society*, 25(9):1551–1564, 2005. ISSN 09552219. doi: 10.1016/j.jeurceramsoc.2004.05.028.
- [85] Steffen B. Fischer and Erin Koos. Influence of drying conditions on the stress and weight development of capillary suspensions. *Journal of the American Ceramic Society*, 104(3):1255–1270, 2021. ISSN 1551-2916. doi: 10.1111/jace.17553.

- [86] G.C.A.M. Janssen, M. M. Abdalla, F. van Keulen, B. R. Pujada, and B. van Venrooy. Celebrating the 100th anniversary of the stoney equation for film stress: Developments from polycrystalline steel strips to single crystal silicon wafers. *Thin Solid Films*, 517(6):1858–1867, 2009. ISSN 0040-6090. doi: 10.1016/j.tsf.2008.07.014.
- [87] E. M. Corcoran. Determining stresses in organic coatings using plate beam deflection. *Journal of Paint Technology*, 41(538):635–&, 1969. ISSN 0022-3352.
- [88] A. B. Kounga Njiwa, E. Aulbach, J. Rodel, and A. Neubrand. Mechanical properties of dry-pressed powder compacts: Case study on alumina nanoparticles. *Journal of the American Ceramic Society*, 89(8):2641–2644, 2006. ISSN 1551-2916. doi: 10.1111/j.1551-2916.2006.01088.x.
- [89] W. Pechhold, U. Mayer, G. B. Raju, and O. Guillon. Piezo rotary and axial vibrator (prav) characterization of a fresh coating during its drying. *Rheologica Acta*, 50(3): 221–229, 2011. ISSN 1435-1528. doi: 10.1007/s00397-010-0526-x.
- [90] Steffen B. Fischer and Erin Koos. Using an added liquid to suppress drying defects in hard particle coatings. *Journal of Colloid and Interface Science*, 582(Part B): 1231–1242, 2021. ISSN 0021-9797. doi: 10.1016/j.jcis.2020.08.055.
- [91] L. Goehring, R. Conroy, A. Akhter, W. J. Clegg, and A. F. Routh. Evolution of mud-crack patterns during repeated drying cycles. *Soft Matter*, 6(15):3562–3567, 2010. ISSN 1744-683X. doi: 10.1039/b922206e.
- [92] Marcel Schmitt, Philip Scharfer, and Wilhelm Schabel. Slot die coating of lithium-ion battery electrodes: investigations on edge effect issues for stripe and pattern coatings. *Journal of Coatings Technology and Research*, 11(1):57–63, 2014. ISSN 1547-0091. doi: 10.1007/s11998-013-9498-y.
- [93] Boris Bitsch, Jens Dittmann, Marcel Schmitt, Philip Scharfer, Wilhelm Schabel, and Norbert Willenbacher. A novel slurry concept for the fabrication of lithium-ion battery electrodes with beneficial properties. *Journal of Power Sources*, 265:81–90, 2014. ISSN 03787753. doi: 10.1016/j.jpowsour.2014.04.115.
- [94] D. M. Holmes, F. Tegeler, and W. J. Clegg. Stresses and strains in colloidal films during lateral drying. *Journal of the European Ceramic Society*, 28(7):1381–1387, 2008. ISSN 09552219. doi: 10.1016/j.jeurceramsoc.2007.12.017.
- [95] Yue Ma, H. T. Davis, and L. E. Scriven. Microstructure development in drying latex coatings. *Progress in Organic Coatings*, 52(1):46–62, 2005. ISSN 03009440. doi: 10.1016/j.porgcoat.2004.07.023.

- [96] Alexander F. Routh and William B. Russel. Horizontal drying fronts during solvent evaporation from latex films. *AIChE Journal*, 44(9):2088–2098, 1998. ISSN 00011541. doi: 10.1002/aic.690440916.
- [97] Qiu Jin, Peng Tan, Andrew B. Schofield, and Lei Xu. Eliminating cracking during drying. *The European Physical Journal. E, Soft matter*, 36(3):28, 2013. doi: 10.1140/epje/i2013-13028-9.
- [98] Caroline A. Schneider, Wayne S. Rasband, and Kevin W. Eliceiri. Nih image to imagej: 25 years of image analysis. *Nature methods*, 9(7):671–675, 2012. ISSN 1548-7105.
- [99] M. Baunach, S. Jaiser, S. Schmelzle, H. Nirschl, P. Scharfer, and W. Schabel. Delamination behavior of lithium-ion battery anodes: Influence of drying temperature during electrode processing. *Drying Technology*, 34(4):462–473, 2016. ISSN 0737-3937. doi: 10.1080/07373937.2015.1060497.
- [100] Lanqing Jiao, Bo Su, Junhu Meng, Jiesheng Han, and Honggang Wang. Effect of surrounding polydimethylsiloxane frame and substrate on drying behavior of aqueous alumina suspensions. *International Journal of Applied Ceramic Technology*, 15(6): 1502–1509, 2018. ISSN 1546542X. doi: 10.1111/ijac.13013.
- [101] L. A. Brown, C. F. Zukoski, and L. R. White. Consolidation during drying of aggregated suspensions. *AIChE Journal*, 48(3):492–502, 2002. ISSN 00011541. doi: 10.1002/aic.690480308.
- [102] Abdolreza Kharaghani, Christoph Kirsch, Thomas Metzger, and Evangelos Tsotsas. Micro-scale fluid model for drying of highly porous particle aggregates. *Computers & Chemical Engineering*, 52:46–54, 2013. ISSN 0098-1354. doi: 10.1016/j.compchemeng.2012.12.003. URL <http://www.sciencedirect.com/science/article/pii/S0098135412003948>.
- [103] Joao Borges Laurindo and Marc Prat. Numerical and experimental network study of evaporation in capillary porous media. drying rates. *Chemical Engineering Science*, 53(12):2257–2269, 1998. ISSN 0009-2509. doi: 10.1016/S0009-2509(97)00348-5. URL <http://www.sciencedirect.com/science/article/pii/S0009250997003485>.
- [104] M. Prat. On the influence of pore shape, contact angle and film flows on drying of capillary porous media. *International Journal of Heat and Mass Transfer*, 50(7): 1455–1468, 2007. ISSN 0017-9310. doi: 10.1016/j.ijheatmasstransfer.2006.09.001. URL <http://www.sciencedirect.com/science/article/pii/S0017931006005163>.

- [105] M. Prat. Pore network models of drying, contact angle, and film flows. *Chemical Engineering & Technology*, 34(7):1029–1038, 2011. ISSN 09307516. doi: 10.1002/ceat.201100056.
- [106] A. G. Yiotis, D. Salin, E. S. Tاجر, and Y. C. Yortsos. Drying in porous media with gravity-stabilized fronts: experimental results. *Physical Review E*, 86(2 Pt 2):026310, 2012. doi: 10.1103/PhysRevE.86.026310.
- [107] Rui Wu, Abdolreza Kharaghani, and Evangelos Tsotsas. Two-phase flow with capillary valve effect in porous media. *Chemical Engineering Science*, 139:241–248, 2016. ISSN 0009-2509. doi: 10.1016/j.ces.2015.09.028. URL <http://www.sciencedirect.com/science/article/pii/S0009250915006508>.
- [108] O. Chapuis and M. Prat. Influence of wettability conditions on slow evaporation in two-dimensional porous media. *Physical Review E*, 75(4):046311, 2007. doi: 10.1103/PhysRevE.75.046311. URL <http://link.aps.org/pdf/10.1103/PhysRevE.75.046311>.
- [109] van Dijke, M. I. J., S. R. McDougall, and K. S. Sorbie. Three-phase capillary pressure and relative permeability relationships in mixed-wet systems. *Transport in Porous Media*, 44(1):1–32, 2001. ISSN 1573-1634. doi: 10.1023/A:1010773606657. URL <https://doi.org/10.1023/A:1010773606657>.
- [110] Martin J. Blunt. Flow in porous media — pore-network models and multiphase flow. *Current Opinion in Colloid & Interface Science*, 6(3):197–207, 2001. ISSN 1359-0294. doi: 10.1016/S1359-0294(01)00084-X. URL <http://www.sciencedirect.com/science/article/pii/S135902940100084X>.
- [111] Alessio Scanziani, Kamaljit Singh, Tom Bultreys, Branko Bijeljic, and Martin J. Blunt. In situ characterization of immiscible three-phase flow at the pore scale for a water-wet carbonate rock. *Advances in Water Resources*, 121:446–455, 2018. ISSN 03091708. doi: 10.1016/j.advwatres.2018.09.010. URL <http://www.sciencedirect.com/science/article/pii/S0309170818304925>.
- [112] Richard A. Cairncross, Lorraine F. Francis, and L. E. Scriven. Predicting drying in coatings that react and gel: Drying regime maps. *AIChE Journal*, 42(1):55–67, 1996. ISSN 00011541. doi: 10.1002/aic.690420107.
- [113] Jens Dittmann, Johannes Maurath, Boris Bitsch, and Norbert Willenbacher. Highly porous materials with unique mechanical properties from smart capillary suspensions. *Advanced Materials*, 28(8):1689–1696, 2016. ISSN 0935-9648. doi: 10.1002/adma.201504910.

- [114] B. Westphal, H. Bockholt, T. Gunther, W. Haselrieder, and A. Kwade. Influence of convective drying parameters on electrode performance and physical electrode properties. *ECS Transactions*, 64(22):57–68, 2015. ISSN 1938-6737. doi: 10.1149/06422.0057ecst.
- [115] Moritz Weiß, Patrick Sälzler, Norbert Willenbacher, and Erin Koos. 3d-printed lightweight ceramics using capillary suspensions with incorporated nanoparticles. *Journal of the European Ceramic Society*, 40(8):3140–3147, 2020. ISSN 09552219. doi: 10.1016/j.jeurceramsoc.2020.02.055. URL <http://www.sciencedirect.com/science/article/pii/S0955221920301631>.
- [116] Karnail B. Singh and Mahesh S. Tirumkudulu. Cracking in drying colloidal films. *Physical Review Letters*, 98(21):218302, 2007.
- [117] Johannes Maurath and Norbert Willenbacher. 3d printing of open-porous cellular ceramics with high specific strength. *Journal of the European Ceramic Society*, 2017. ISSN 09552219. doi: 10.1016/j.jeurceramsoc.2017.06.001.
- [118] Lucas Goehring, William J. Clegg, and Alexander F. Routh. Plasticity and fracture in drying colloidal films. *Physical Review Letters*, 110(2):024301, 2013. doi: 10.1103/PhysRevLett.110.024301.
- [119] O. Coussy, P. Dangla, T. Lassabatère, and V. Baroghel-Bouny. The equivalent pore pressure and the swelling and shrinkage of cement-based materials. *Materials and Structures*, 37(1):15–20, 2004. ISSN 1359-5997. doi: 10.1007/BF02481623.
- [120] Alejandro Estrada-Baltazar, Micael Gerardo Bravo-Sanchez, Gustavo Arturo Iglesias-Silva, Juan Francisco Javier Alvarado, Edgar Omar Castrejon-Gonzalez, and Mariana Ramos-Estrada. Densities and viscosities of binary mixtures of n-decane+1-pentanol, +1-hexanol, +1-heptanol at temperatures from 293.15 to 363.15k and atmospheric pressure. *Chinese Journal of Chemical Engineering*, 23(3):559–571, 2015. ISSN 10049541. doi: 10.1016/j.cjche.2013.10.001.
- [121] Karnail B. Singh, Laxman R. Bhosale, and Mahesh S. Tirumkudulu. Cracking in drying colloidal films of flocculated dispersions. *Langmuir*, 25(8):4284–4287, 2009. ISSN 0743-7463. doi: 10.1021/la804331c.
- [122] Luis A. Segura and Pedro G. Toledo. Pore-level modeling of isothermal drying of pore networks. *Chemical Engineering Journal*, 111(2-3):237–252, 2005. ISSN 13858947. doi: 10.1016/j.cej.2005.02.004.

- [123] Joekar-Niasar and S. M. Hassanizadeh. Analysis of fundamentals of two-phase flow in porous media using dynamic pore-network models: A review. *Critical Reviews in Environmental Science and Technology*, 42(18):1895–1976, 2012. ISSN 1064-3389. doi: 10.1080/10643389.2011.574101.
- [124] Ryan T. Armstrong, Mark L. Porter, and Dorte Wildenschild. Linking pore-scale interfacial curvature to column-scale capillary pressure. *Advances in Water Resources*, 46:55–62, 2012. ISSN 03091708. doi: 10.1016/j.advwatres.2012.05.009.
- [125] Eva L. Davis. Effect of temperature and pore size on the hydraulic properties and flow of a hydrocarbon oil in the subsurface. *Journal of Contaminant Hydrology*, 16(1): 55–86, 1994. ISSN 01697722. doi: 10.1016/0169-7722(94)90072-8.
- [126] Hugh Y. She and Brent E. Sleep. The effect of temperature on capillary pressure-saturation relationships for air-water and perchloroethylene-water systems. *Water Resources Research*, 34(10):2587–2597, 1998. ISSN 1944-7973. doi: 10.1029/98WR01199.
- [127] Samantha J. Heidlebaugh, Trystan Domenech, Steven V. Iasella, and Sachin S. Velankar. Aggregation and separation in ternary particle/oil/water systems with fully wettable particles. *Langmuir*, 30(1):63–74, 2014. ISSN 0743-7463. doi: 10.1021/la4039396.
- [128] Chao Zhang and Paolo Carloni. Salt effects on water/hydrophobic liquid interfaces: a molecular dynamics study. *Journal of Physics. Condensed matter*, 24(12):124109, 2012. doi: 10.1088/0953-8984/24/12/124109.
- [129] Steffen B. Fischer and Erin Koos. Capillary bridge formation at room temperature in binary liquids with small miscibility. *Colloid and Interface Science Communications*, 41:100373, 2021. doi: 10.1016/j.colcom.2021.100373.
- [130] H. Rumpf. Grundlagen und Methoden des Granulierens. *Chemie Ingenieur Technik*, 30(3):144–158, 1958. ISSN 0009286X. doi: 10.1002/cite.330300307.
- [131] Stephan Herminghaus. Dynamics of wet granular matter. *Advances in Physics*, 54(3):221–261, 2005. ISSN 0001-8732. doi: 10.1080/00018730500167855.
- [132] Hans-Jürgen Butt. Capillary forces: influence of roughness and heterogeneity. *Langmuir*, 24(9):4715–4721, 2008. ISSN 0743-7463. doi: 10.1021/la703640f.
- [133] J.P.K. Seville, C. D. Willett, and P. C. Knight. Interparticle forces in fluidisation: a review. *Powder Technology*, 113(3):261–268, 2000. ISSN 00325910. doi: 10.1016/S0032-5910(00)00309-0.

-
- [134] St. Palzer. Agglomeration of pharmaceutical, detergent, chemical and food powders — similarities and differences of materials and processes. *Powder Technology*, 206(1-2): 2–17, 2011. ISSN 00325910. doi: 10.1016/j.powtec.2010.05.006.
- [135] C. R. Bloomquist and R. S. Shutt. Fine particle suspensions in organic liquids. *Industrial & Engineering Chemistry*, 32(6):827–831, 1940. ISSN 0019-7866. doi: 10.1021/ie50366a019.
- [136] Trystan Domenech, Junyi Yang, Samantha Heidlebaugh, and Sachin S. Velankar. Three distinct open-pore morphologies from a single particle-filled polymer blend. *Physical chemistry chemical physics : PCCP*, 18(6):4310–4315, 2016. doi: 10.1039/c5cp07576a.
- [137] Junyi Yang, David Roell, Martin Echavarria, and Sachin S. Velankar. A microstructure-composition map of a ternary liquid/liquid/particle system with partially-wetting particles. *Soft Matter*, 13(45):8579–8589, 2017. ISSN 1744-683X. doi: 10.1039/C7SM01571B.
- [138] Trystan Domenech and Sachin S. Velankar. On the rheology of pendular gels and morphological developments in paste-like ternary systems based on capillary attraction. *Soft Matter*, 11(8):1500–1516, 2015. ISSN 1744-683X. doi: 10.1039/c4sm02053g.
- [139] Trystan Domenech and Sachin S. Velankar. Microstructure, phase inversion and yielding in immiscible polymer blends with selectively wetting silica particles. *Journal of Rheology*, 61(2):363–377, 2017. ISSN 0148-6055. doi: 10.1122/1.4975931.
- [140] Krassimir D. Danov, Mihail T. Georgiev, Peter A. Kralchevsky, Gergana M. Radulova, Theodor D. Gurkov, Simeon D. Stoyanov, and Eddie G. Pelan. Hardening of particle/oil/water suspensions due to capillary bridges: Experimental yield stress and theoretical interpretation. *Advances in colloid and interface science*, 251:80–96, 2018. ISSN 1873-3727. doi: 10.1016/j.cis.2017.11.004.
- [141] Waleed Mustafa, Gianpiero Pataro, Giovanna Ferrari, and Francesco Donsì. Novel approaches to oil structuring via the addition of high-pressure homogenized agri-food residues and water forming capillary bridges. *Journal of Food Engineering*, 236:9–18, 2018. ISSN 02608774. doi: 10.1016/j.jfoodeng.2018.05.003.
- [142] Bhuvnesh Bharti, Anne-Laure Fameau, Michael Rubinstein, and Orlin D. Velev. Nanocapillarity-mediated magnetic assembly of nanoparticles into ultraflexible filaments and reconfigurable networks. *Nature Materials*, 14(11):1104–1109, 2015. ISSN 1476-1122. doi: 10.1038/nmat4364.

- [143] Anupam A. K. Das, Timothy S. Dunstan, Simeon D. Stoyanov, Pierre Starck, and Vesselin N. Paunov. Thermally responsive capillary suspensions. *ACS Applied Materials & Interfaces*, 9(50):44152–44160, 2017. ISSN 1944-8244. doi: 10.1021/acsami.7b11358.
- [144] Andrzej Maczynski, David G. Shaw, Marian Goral, and Barbara Wisniewska-Gocłowska. Iupac-nist solubility data series. 82. alcohols with water—revised and updated: Part 3. c₆ alcohols with water. *Journal of Physical and Chemical Reference Data*, 36(2):399, 2007. ISSN 00472689. doi: 10.1063/1.2383067.
- [145] Andrzej Maczynski, David G. Shaw, Marian Goral, and Barbara Wisniewska-Gocłowska. Iupac-nist solubility data series. 82. alcohols with water—revised and updated: Part 4. c₇ alcohols with water. *Journal of Physical and Chemical Reference Data*, 36(2):445–484, 2007. doi: 10.1063/1.2389037. URL <http://scitation.aip.org/content/aip/journal/jpcrd/36/2/10.1063/1.2389037>.
- [146] Andrzej Maczynski, David G. Shaw, Marian Goral, and Barbara Wisniewska-Gocłowska. Iupac-nist solubility data series. 82. alcohols with water—revised and updated: Part 5. c₈–c₁₇ alcohols with water. *Journal of Physical and Chemical Reference Data*, 36(3):685–731, 2007. doi: 10.1063/1.2391321. URL <http://scitation.aip.org/content/aip/journal/jpcrd/36/3/10.1063/1.2391321>.
- [147] Hans-Jürgen Butt and Michael Kappl. *Surface and interfacial forces*. Wiley-VCH, Weinheim, 2010. ISBN 9783527408498.
- [148] Volker Franz and Hans-Jürgen Butt. Confined liquids: Solvation forces in liquid alcohols between solid surfaces. *The Journal of Physical Chemistry B*, 106(7):1703–1708, 2002. ISSN 1520-6106. doi: 10.1021/jp012541w.
- [149] Yiling Tian, Liqian Cao, Lijuan Qiu, and Rongjiao Zhu. Comparison study on temperature dependence of the interfacial tension of n -alkane–water and n -alcohol–water two binary systems. *Journal of Chemical & Engineering Data*, 59(11):3495–3501, 2014. ISSN 0021-9568. doi: 10.1021/je500450w.
- [150] C. L. Flemmer. On the regime boundaries of moisture in granular materials. *Powder Technology*, 66(2):191–194, 1991. ISSN 00325910. doi: 10.1016/0032-5910(91)80100-W.
- [151] Hitoshi Takase. Influence of interparticle forces on selective wet agglomeration. *Advanced Powder Technology*, 20(4):327–334, 2009. ISSN 09218831. doi: 10.1016/j.apt.2009.01.005.

- [152] Tian-Le Cheng and Yu U. Wang. Spontaneous formation of stable capillary bridges for firming compact colloidal microstructures in phase separating liquids: a computational study. *Langmuir*, 28(5):2696–2703, 2012. ISSN 0743-7463. doi: 10.1021/la2044152.
- [153] Dong NguyenHuynh. Correlation and prediction of liquid–liquid equilibria for alcohol/hydrocarbon mixtures using pc-saft equation of state at high pressure up to 150 mpa. *Fluid Phase Equilibria*, 425:206–214, 2016. ISSN 03783812. doi: 10.1016/j.fluid.2016.06.002.
- [154] Roland Nagl, Patrick Zimmermann, and Tim Zeiner. Interfacial mass transfer in water–toluene systems. *Journal of Chemical & Engineering Data*, 65(2):328–336, 2020. ISSN 0021-9568. doi: 10.1021/acs.jced.9b00672.

Curriculum Vitae

Steffen Benno Fischer



Work experience:

10/2019 – to date	Evonik Operations GmbH , Hanau (Germany) Process Engineer
02/2017 – 08/2019	KU Leuven , Leuven (Belgium) Visiting researcher
11/2014 – 11/2017	Karlsruhe Institute of Technology , Karlsruhe (Germany) Research Associate
04/2015 – 07/2015	Seoul National University , Seoul (South Korea) Visiting researcher
03/2013 – 08/2013	Merck KGaA , Darmstadt (Germany) Internship, member of the STEP excellence program
09/2010 – 07/2011	University of Massachusetts , Amherst (USA) Research Assistant

Education:

11/2014 – to date	Karlsruhe Institute of Technology , Karlsruhe (Germany) PhD student
10/2007 to 10/2014	Karlsruhe Institute of Technology , Karlsruhe (Germany) Dipl.-Ing. in Process Engineering Final grade: 1.5 (sehr gut)
09/2013-06/2014	University of Canterbury , Christchurch (New Zealand) Diploma- thesis (grade: 1.0):
09/2010 - 07/2011	University of Massachusetts , Amherst (USA) Exchange student in the Chemical Engineering Department
1997 – 2006	Helfenstein-Gymnasium , Geislingen/ Steige (Germany) Degree: Allgemeine Hochschulreife